2008-06-11

# 3D A-Mode Ultrasound Calibration and Registration of the Tibia and Femur for Computer-Assisted Robotic Surgery

Alon Mozes
*University of Miami*, alon.mozes@alum.mit.edu

UNIVERSITY OF MIAMI

# 3D A-MODE ULTRASOUND CALIBRATION AND REGISTRATION OF THE TIBIA AND FEMUR FOR COMPUTER-ASSISTED ROBOTIC SURGERY

By

Alon Mozes

A DISSERTATION

Submitted to the Faculty
of the University of Miami
in partial fulfillment of the requirements for
the degree of Doctor of Philosophy

Coral Gables, Florida

June 2008

UNIVERSITY OF MIAMI

A thesis submitted in partial fulfillment of
the requirements for the degree of
Doctor of Philosophy

# 3D A-MODE ULTRASOUND CALIBRATION AND REGISTRATION OF THE TIBIA AND FEMUR FOR COMPUTER-ASSISTED ROBOTIC SURGERY

Alon Mozes

Approved:

| | |
|---|---|
| _____<br>Dr. Weizhao Zhao<br>Associate Professor of<br>Biomedical Engineering | _____<br>Dr. Terri A. Scandura<br>Dean of the Graduate School |
| _____<br>Dr. Ozcan Ozdamar<br>Professor and Chair of Biomedical<br>Engineering | _____<br>Dr. Fabrice Manns<br>Associate Professor of Biomedical<br>Engineering |
| _____<br>Dr. Sohyung Cho<br>Assistant Professor of Industrial<br>Engineering | _____<br>Dr. Jorge E. Bohorquez<br>Research Assistant Professor of<br>Biomedical Engineering |

_____
Dr. Lou Arata
Chief Software Architect
MAKO Surgical Corp.

MOZES, ALON (Ph.D., Biomedical Engineering)
3D A-Mode Ultrasound Calibration and Registration of the Tibia and Femur for Computer-Assisted Robotic Surgery (June 2008)

Abstract of a dissertation at the University of Miami.

Dissertation supervised by Professor Weizhao Zhao.
No. of pages in text. (154)

Registration is a key component for computer-navigated robot-assisted surgery. Invasive approaches such as fiducial-based and surface matching with mechanical probes are common but ultrasound may provide a non-invasive alternative. If an A-mode ultrasound transducer can be used to percutaneously select data points on the bones, a registration can be determined without needing any incision. This study investigates selecting an A-mode ultrasound transducer, calibrating it, analyzing the ultrasound signal, and using it to register a phantom sawbone tibia and femur as well as cadaveric specimens. This study is performed in conjunction with MAKO Surgical Corp.'s Tactile Guidance System™ (TGS™) at their headquarters and at The South Florida Spine Clinic for cadaveric experiments. The results for phantom and cadaveric ultrasound registrations compared to a mechanical probe approach demonstrate that A-mode ultrasound registration is a viable option for registration of the bones of the knee.

Acknowledgment

I would like to thank my committee for taking the time to help me through this endeavor. My advisor, Dr. Zhao, has been a great teacher and source of support throughout my time in the program. His guidance has made this a positive and memorable experience.

This research has been a collaboration between MAKO Surgical Corp. and the University of Miami. MAKO Surgical Corp. has given me a tremendous amount of support. Rony Abovitz, Menashe Frank, and Fritz Laporte from MAKO Surgical Corp. along with Dr. Ozdamar and Dr. Zhao from the University of Miami were instrumental in making the collaboration happen.

I would also like to thank my coworkers at MAKO Surgical Corp. who have assisted me with many of my experiments that would have been impossible without their helping hands. Alexandra Bellettre, Hyosig Kang, Nuri Acikgoz, Tim Perez, and Steven McKnight among others have given significant support.

I would like to thank my friends and family who have encouraged me through an often arduous process and kept me motivated to finish. My parents were consistently supportive no matter what my decisions were. Lanitia Ness and Mandana Dashtaki have helped me to stay positive over the years with kind words, and Whitney Bloom has shared the late nights and pain of reviewing and re-reviewing the same document.

Finally, I would like to thank Dr. Lou Arata who has served as my supervisor, committee advisor, mentor, and friend since I began working at MAKO Surgical Corp. He has helped me to improve in ways that will last beyond the classroom and workplace.

**TABLE OF CONTENTS**

LIST OF EQUATIONS:

LIST OF FIGURES:

LIST OF TABLES:

## Chapter 1: Introduction

### 1.1 Osteoarthritis of the Knee

Osteoarthritis is a non-inflammatory degenerative joint disease characterized by the breakdown of the joint's cartilage (Fig. 1.1). This disease can affect the knee and create a debilitating condition. The knee joint has several areas that require smooth contact in order to move properly between the bones of the knee, specifically between the femur and tibia and between the patella and the femur. Cartilage in the joint serves as a cushion at these interfaces. The degeneration of the cartilage as a result of osteoarthritis can lead to severe pain.

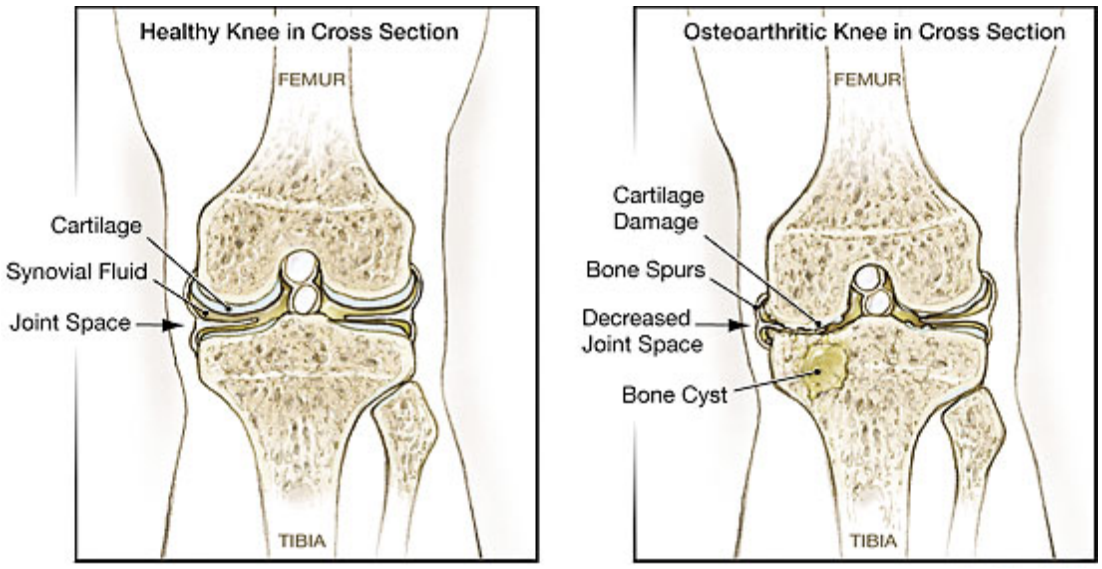


**Figure 1.1: A healthy knee on the left shows significant joint space cushioned by cartilage and synovial fluid [55]. A diseased knee on the right shows a collapsed medial compartment due to poor cartilage. A patient with the knee on the right will suffer from debilitating pain due to the bones rubbing together.**

Several causes can bring about this condition, including nutrition and lack of physical exercise [47]. Non-surgical treatments exist; pain-relievers and regular exercise are often prescribed [55]. Cortisone shots may help to reduce the inflammation in the

joint that is often a symptom of osteoarthritis. In patients with severely damaged joints, surgery is a possibility.

Surgical knee replacement removes bone from the two main bones of the joint, the femur and tibia. The tibia plateau is replaced with a polyethelene component and the femoral condyle is replaced with a metal component. The components are contoured to match the anatomy being removed. For knees with greater progression of disease, a total knee replacement is often needed. However, unicondylar knee replacement (UKR) is an option that removes less bone through a smaller incision while still relieving the osteoarthritic condition (Fig. 1.2).

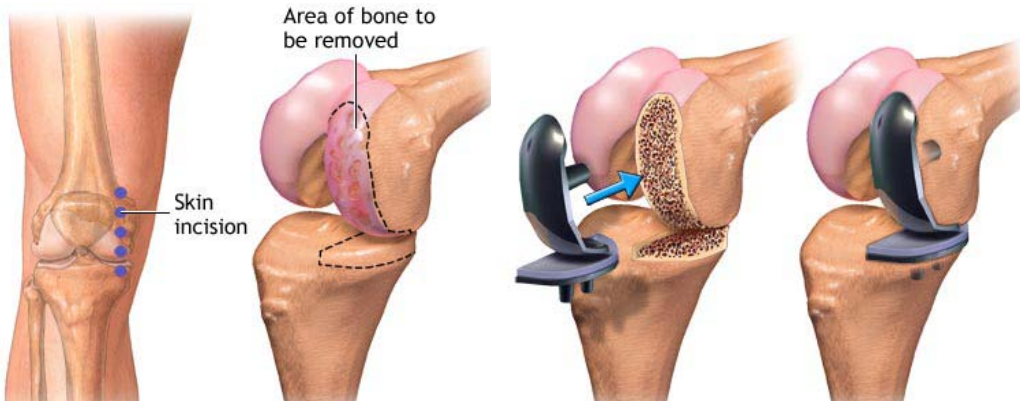


**Figure 1.2: The progression of a unicondylar knee replacement procedure [26]. The incision is shown on the medial side and is relatively small. The diseased portion of the anatomy is limited to the medial side and is subsequently removed. The implants designed to match the femur and tibia contours are placed in the bone.**

## 1.2 Arthroscopy

Arthroscopy, a type of endoscopy that is inserted into the joint through a small incision, is a traditional surgical procedure orthopedic surgeons use to visualize, diagnose

and treat problems inside a joint. It has opened a new chapter by using advanced medical imaging techniques. Although arthroscopy was first successfully performed on the human knee in the early 1920s, the procedure was not widely applied until the 1970s. During the 1980s, advances in biomedical engineering improved the technology enough for the technique to be used for joint surgery. This spurred the development of many new instruments and techniques, including suction punches, graspers, cutting tools, and power tools such as the shaver and burr. The camera attached to the arthroscope displays the "inside" image of the joint on a television screen with a minimal cut, allowing the surgeon to look throughout the knee at cartilage, ligaments, and under the patella. The surgeon can determine the amount or type of injury and then repair or correct the problem if necessary. New endoscopes have digital capabilities for manipulating and enhancing images. In some new procedures, cartilage can be harvested and grown for re-implantation later. In the 1990s, image-guided surgery systems (IGSs) started attracting people's attention [10, 23]. Most medical imaging facilities have been involved in different kinds of surgical procedures [23, 25, 32, 53]. Associated with pixel-level accuracy, "digital surgery" became feasible, particularly on knee operations. Digital surgery relies on two aspects of important background knowledge: medical imaging principles (image reconstruction and image processing techniques) and three-dimensional registration. The first aspect provides information about "what it is" (e.g., bone or soft tissue, which is represented by different signals under different imaging modalities). The second aspect provides information about "where it is" (e.g., localization between/among different imaging modalities and image planes).

**1.3 Significance of the Study**

The leading cause of disability in the United States is arthritis, according to Centers For Disease Control and Prevention and the U.S. Department of Health and Human Services. Osteoarthritic conditions in the knee represent a significant portion of the U.S. population disabled by arthritis. Arthritis accounts for at least 750,000 hospitalizations, and 36 million outpatient visits [71, 72]. Nearly 60% of U.S. citizens with arthritis are younger than 65 years old [71, 72], and they have a low rate of labor force participation. Approximately 400,000 knee surgery procedures are performed yearly in the U.S., which is expected to grow to 500,000 per year by 2007 [19]. Total Knee Replacement (TKR) has become a proven surgical intervention to treat this condition, relieve the pain, and restore the patient to reasonable function. Current TKR surgery results in long hospital stays, coupled with a costly and painful rehabilitation periods [27].

Repairing surgeries on the knee due to other injuries are also performed with arthroscopic procedures. Arthroscopic surgery has virtually replaced arthrotomy, a crude and invasive method of evaluating a joint with exploratory surgery. Before the advent of arthroscopy, surgery on the meniscus involved a many-centimeter-long incision along the side of the knee, with a recovery period that could last months. In normal arthroscopic operations, the incisions are so small, usually no more than a quarter of an inch, that they typically require only one stitch, if any. This helps patients recover from minimally invasive arthroscopic surgery much quicker than open orthopedic surgery. For professional athletes, this means a much faster return to the playing field. For weekend

warriors and people who sustain other joint injuries, arthroscopic surgery means getting back on your feet much sooner.

Computer-assisted robot arthritis surgery has been a new approach for about 10 years. A robot arm originally designed for assembling line with positioning accuracy of 0.5 mm in three dimensions has been integrated into arthritis surgery [11, 17, 45, 59]. Research in developing systems to enable minimally-invasive TKR surgery or knee repairing has a significant impact for future orthopedic surgery procedures. A system with advanced medical imaging guidance and high-accuracy robot positioning has the potential to enable same-day surgical procedures and a shorter period of rehabilitation. It also has the potential to become a clinical technique that can be easily replicated by both major academic centers and small community hospitals.

### 1.4 Aims of the Study

A computer-assisted robotic surgery system has the potential to relieve many patients of symptoms of knee osteoarthritis, but it requires that its components are conducive to a practical and minimally invasive approach. Current standards of computer guidance often necessitate large incisions and time-consuming protocols. Combining A-mode ultrasound, a simple imaging modality, with a computer-assisted robotic surgery system yields a minimally invasive and expedient application of digital surgery.

This study intended to develop such a system. The system should be calibrated and tested on plastic phantoms of bones in the knee. The study would investigate the efficacy of this system on cadaver specimens and compare the performance of various

techniques and design choices. Filtering algorithms, hardware equipment, and protocol techniques are all to be evaluated. Calibration results are to be measured using an objective function based on the distance of the collected points from the calibration phantom. Registration results are to be interpreted using transformation error metrics relative to standard techniques and graphic reconstructions that use 3D models of the bones being registered.

Specifically, the aims of the study are:

1) To design and implement a 3D ultrasound system that uses A-mode transducers, optical tracking, and a current industry navigation system.
2) To create signal processing algorithms for analyzing various ultrasound signals on phantoms and cadaver specimens and test their use in registration of phantom femur and tibia models
3) To design and test a calibration protocol for calibrating the tracked A-mode system.
4) To develop an ultrasound approach to knee registration that takes advantage of A-mode ultrasound benefits
5) To test the system and signal processing for use with human cadaver specimens
6) Perform data analysis on signal processing, calibration, and registration results

## Chapter 2: Computer-Assisted Orthopedic Surgery (CAOS)

Computer-assisted orthopedic surgery (CAOS) is the use of computers to assist orthopedic surgeons in executing procedures such as hip or knee replacement or spinal pedicle screw insertion. They often involve some tracking mechanism, such as cameras or mechanical trackers, and they process the tracking information to provide the surgeon with details about the procedure. This information could be the orientation of a pedicle screw relative to the spine, the depth of a tibial implant placement, or verifying kinematics of the knee once the surgery is complete. CAOS also provides the opportunity to visualize and plan the surgery before it even begins. It allows for precision and reliability in surgery that is unattainable by human hands alone.

In the case of knee replacement, failed surgeries are often due to poor alignment of the implants and poor manual instrumentation [20]. Orienting implant components significantly beyond nominal angles can adversely affect implant survival rates. Manual instrumentation is not sufficient for accurately aligning the various cuts involved with knee reconstruction [20]. CAOS allows for consistent and accurate implant placement which avoids the problems with conventional knee replacement surgery.

Langlotz and Nolte breakdown CAOS systems into a few critical components: a therapeutic object, a virtual object, and a navigation component that uses registration to link the two [41]. The therapeutic object is simply the portion of the patient's anatomy that is the object of the operation. The virtual object is a computer model of the anatomy based on an imaging modality like CT or MRI, or as with an imageless approach, the virtual model can be a generic model, which will morph using intraoperative imaging

results. For the navigation system to provide assistance, it must have an understanding of the relationship between the virtual object and therapeutic object. Surgeons must perform a registration to teach the system about that relationship. With this registration, the system can provide intraoperative feedback about how the surgery is being conducted on the actual patient relative to a virtual plan or model (Fig. 2.1).

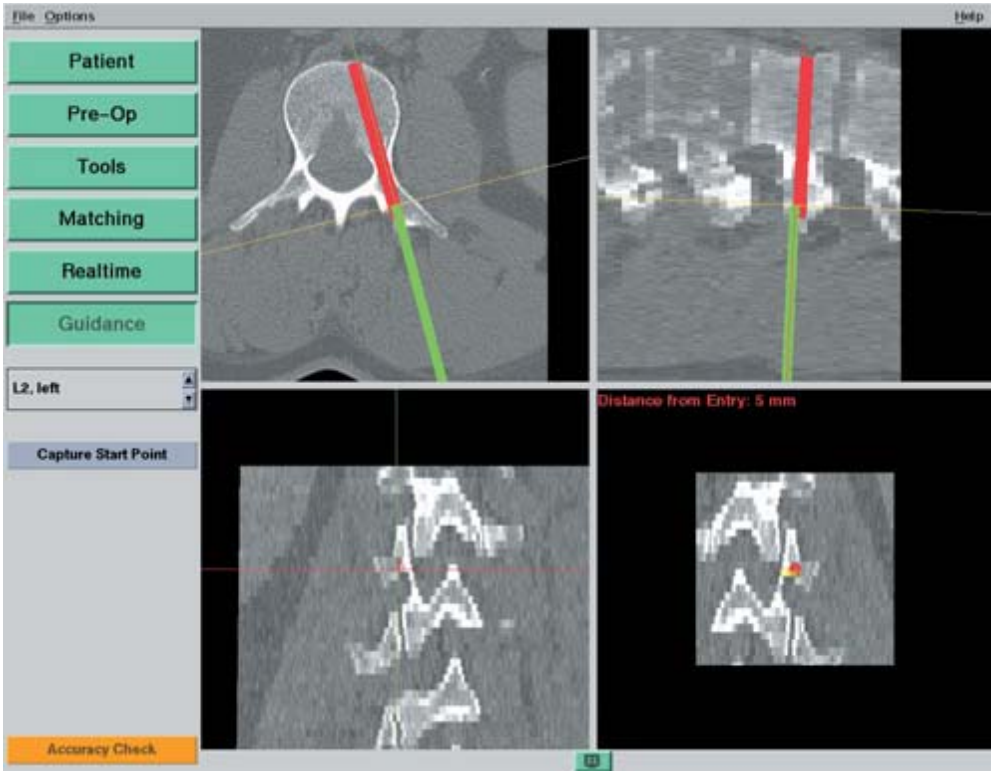


**Figure 2.1: Example of navigational feedback [41]. In this case of CT-based navigation during pedicle screw placement, the optimal location for the screw in L2 has been planned preoperatively (red line). The current position and orientation of the instrument used to prepare the screw canal is overlaid as a green line, facilitating precise alignment of the instrument with the plan.**

However, establishing this registration can be a time consuming process. Sikorski explains that costs are inherent in the use of CAOS [64]. Operations take longer due to additional steps required by the system, and depending on the system, additional imaging may be required. This leads to added financial cost and possibly radiation exposure.

Sikorski also explains that the benefits of CAOS are "conjectural" until long term results prove its efficacy.

In the meantime, CAOS systems continue to evolve from their beginnings around 1994. They are no longer strictly passive navigation assistants. With robotic augmentation, systems can now bridge the gap between providing on-screen help and physically aiding the surgeon in performing the procedure. Some surgical robotic systems are active, meaning that they perform cutting autonomously using navigation information. Others are passive and may simply hold a cutting jig in its proper place while the surgeon executes all the cutting. There are also semi-active robots that hold the cutting instrument, which restricts the motion of the surgeon to prevent any cuts that are not according to plan, but do not actively make any cuts [41].

## 2.1 Registration Principles

Registration is the mapping of one coordinate system to another. It can be the mapping of one two-dimensional space to another two-dimensional space, as with the fusion of CT to MRI images. It can also be the mapping of a two-dimensional space to a three-dimensional space, as with the inclusion of a 2D slice in a 3D model. In the case of CAOS, there are two coordinate spaces of primary concern. There is an image space, which contains a computer model of the patient anatomy based on MRI, CT, ultrasound, or a statistical average of typical patient anatomy (imageless). There is also a physical space, which is the coordinate space of the actual patient anatomy. In CAOS, the physical space is usually "seen" by the system with an infrared camera that tracks a reflective array embedded into the bone. The registration involves determining a series

of 4×4 six degree-of-freedom matrix transformations that will convert a point from image space to physical space and vice versa.

### 2.1.1 Image Space Model Using Segmentation

An essential part of registration is the creation of the image space model to which the physical model is matched. Sometimes an imageless approach is taken, meaning that a generic bone shape is used for the image space model. The model is then morphed using an affine transformation based on the intraoperative data that is collected. For this method to be accurate, significant coverage of the physical anatomy must be captured intraoperatively to constrain the shape as the image space model is morphed. This could require a more invasive surgical technique.

Other approaches use preoperative imaging to generate an accurate image space model. Modalities for this include MRI, CT, and ultrasound. All modalities result in a three-dimensional image from which the bone must be segmented. Numerous techniques exist to segment the bone. The process involves drawing contours around the bone in numerous two-dimensional slices. The contours are then stacked up to form a three-dimensional model of the bone.

By taking advantage of different image intensity values for bone, algorithms can use edge detection techniques to separate the bone from tissue. Manual techniques can be tedious and time-consuming. Even though segmentation is a preoperative step and does not drain surgical time, automated techniques are preferable as the chance for mistakes can be reduced and system usability is improved. Some automated techniques take advantage of commonalities between bones by using a typical bone model as a

starting point. The bone model is then used as a reference to segment the particular bone of the current patient. Since slight variation from the average bone can create errors in the segmentation, a more manual approach may be necessary.

Live-Wire is an algorithm that provides a compromise between accuracy and ease of use by finding the edge between user-determined points on the edge of the bone [76]. This semi-automated approach allows the user to control most of the segmentation process but allows the computer to assist and remove much of the tedious aspects of drawing each contour. In MAKO Surgical Corp.'s approach, Live-Wire is implemented by a user manually dropping anchor points around the edge of the bone with the mouse. As the user creates these points, the software will automatically connect the points using the Live-Wire edge detection algorithm (Fig. 2.2). The result is that each slice has a contour that can be segmented quickly and accurately.

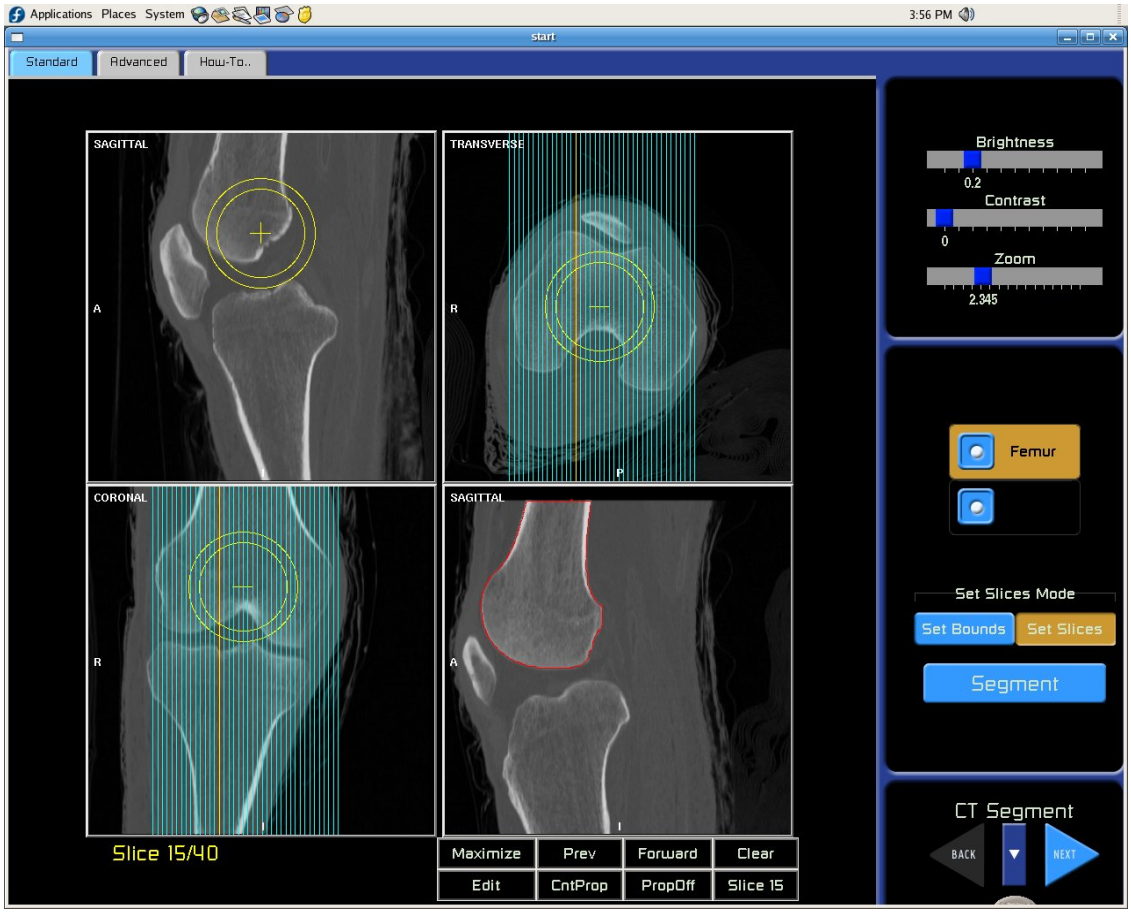


**Figure 2.2: The segmentation screen from the MAKO Surgical Corp.'s navigation system. The upper left window shows a sagittal view of a knee, the upper right window shows a transverse view of a knee, and the lower left window shows a coronal view of the knee. The lower right window shows a sagittal view of a femur that is contoured. The red line around the femur in the lower right window indicates the contour that was drawn using the Live-Wire algorithm.**

Region growing is a more automated approach that requires minimal interaction from the user. The user must place a seed in a given slice and the algorithm then determines the region contiguous to the initial seed that matches it in intensity [57]. This can progress within a slice as well as through successive slices thereby yielding a three-dimensional model. Region-growing may require a manual verification step to ensure accuracy since some intensity values may not clearly fall inside or outside the model boundary.

A similar automated technique known as thresholding requires very little user interaction. The algorithm simply analyzes each voxel's intensity to determine whether it is part of the model or not. While this is a simple approach, the accuracy is less consistent. The difficulty with this approach is that noise and speckle can have a significantly negative effect on the resulting model. Manual adjustments are necessary to make it a clinically viable approach for procedures that require accuracy.

### 2.1.2 Matrix Transformations

The previously mentioned data points are located in the image space. Considering the bone is "non-deformable", we need a rigid transformation to connect the image space to the physical space, which is typically presented by the 4×4 matrix. Rigid transformations focus on translation and rotation (Fig. 2.3, 2.4). The scale components will be fixed which will prevent scaling and shearing since those are used mostly with morphing techniques for imageless registration approaches. The transformation matrix can be decomposed into its component parts [34], which make it easy to compare various transformations. This is useful for understanding how the registration from one technique may differ from another. Equations 2.1 and 2.2 show two-dimensional and three-dimensional examples of translation and rotation transformation matrices respectively. In order to determine the value of each element in the transformation matrix, i.e., registration transformation, point-matching by a robust tracking system is required.

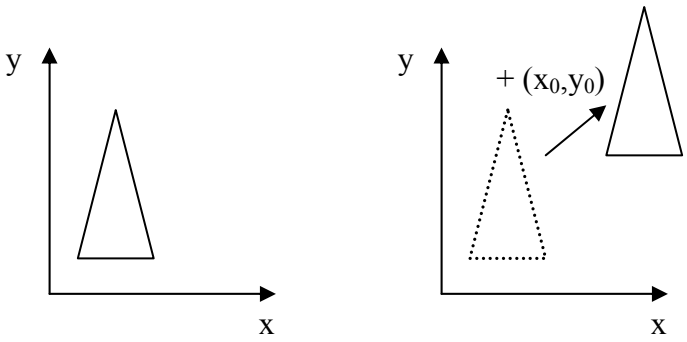


**Figure 2.3: Two-dimensional translation of a triangle. The triangle is translated by $x_0$ along the x-axis and $y_0$ along the y-axis. This translation is achieved by applying a translational transformation matrix as in Equation 2.1.**

$$\begin{bmatrix} x' \\ y' \\ 1 \end{bmatrix} = \begin{bmatrix} 1 & 0 & x_0 \\ 0 & 1 & y_0 \\ 0 & 0 & 1 \end{bmatrix} \cdot \begin{bmatrix} x \\ y \\ 1 \end{bmatrix} \qquad \textbf{(Eq. 2.1)}$$

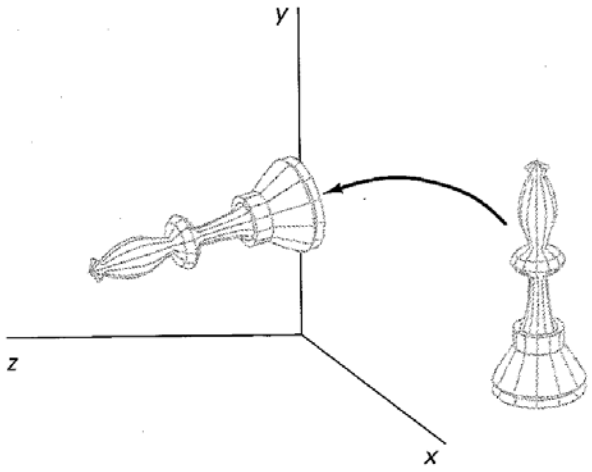


**Figure 2.4: A three-dimensional object is rotated about the x-axis. The data points that comprise the object are each transformed using a rotational transformation matrix similar to the one in Equation 2.2. Figure is taken from Hearn and Baker [34].**

$$\begin{bmatrix} x' \\ y' \\ z' \\ 1 \end{bmatrix} = \begin{bmatrix} 1 & 0 & 0 & 0 \\ 0 & \cos\theta & -\sin\theta & 0 \\ 0 & \sin\theta & \cos\theta & 0 \\ 0 & 0 & 0 & 1 \end{bmatrix} \cdot \begin{bmatrix} x \\ y \\ z \\ 1 \end{bmatrix} \quad \textbf{(Eq. 2.2)}$$

2.1.3 Fiducial-Based Point Pair Matching

There are numerous ways to register a patient. Fiducial based registration is accepted as yielding clinically accurate results as evidenced by its use as the gold standard for registration analyses [3, 8, 46]. The patient has fiducial markers implanted in the bone prior to being scanned by an MRI or CT machine (Fig. 2.5). The coordinates of those fiducials are chosen in image space. Then the surgeon points to those fiducials with a tracked probe relative to a tracked array embedded in the bone in order to capture those coordinates in physical tracker space. The two sets of coordinates are matched using a point-pair algorithm. The number of fiducials in the matching varies depending on the anatomy and the size of the area to be registered. The resulting registration is accurate to less than 1mm [14], but was achieved through invasive means as those fiducials required being implanted directly into bone for an extended period.

**Figure 2.5: An Acustar fiducial cap is used for a fiducial-based registration [52]. The user is holding an optically tracked instrument that is precisely indicating the position of the fiducial marker. Several fiducial markers can be used to create an accurate registration between an image space model with radiopaque markers and a physical model with the embedded markers accessible to a pointer.**

### 2.1.4 Surface Matching with ICP

A less invasive registration method exists that does not require any fiducials to be implanted prior to surgery. This method, called surface matching, involves using a probe that is tracked by the camera to identify points on the anatomy relative to the array that is attached to the patient's bone. An optimization routine uses these points in an iterative closest point (ICP) algorithm to line up the physical space points with the image space model [9]. The optimization routine uses an initial transform and iterates, perturbing the transform a certain amount each time. A new set of corresponding points is established each iteration. An objective function measures the error of the new corresponding points and determines if the perturbation was in the right direction. The routine continues until the maximum number of iterations has been executed or the remaining error as determined by the objective function is below a predetermined threshold. The transform

that results in the best fit is the registration. The outline of each iteration in ICP has been described by Rusinkiewicz et al [61] as follows:

1. Selection of some set of points in one data set.
2. Matching these points to samples in the other set.
3. Weighting the corresponding pairs appropriately.
4. Rejecting certain pairs based on looking at each pair individually or considering the entire set of pairs.
5. Assigning an error metric based on the point pairs.
6. Minimizing the error metric.

The optimization routine also requires an initial guess for the desired transformation. This guess, called a rough registration or pre-registration, can have a dramatic effect on the convergence of the algorithm [40]. If the initial guess is poor, the algorithm may converge on a local minimum rather than the desired global minimum. To alleviate this problem, researchers have developed versions of the optimization that perturb the initial guess in translation and rotation parameters and then attempt to re-register with the new guess [40].

Often, a small group of coarse landmarks are used for the initial guess for the optimization routine. The landmarks are typically a set of anatomical positions that are easy for the surgeon to locate on the patient. Gong et al describe a variation of ICP that incorporates the coarse landmarks into the iterative portion of the optimization routine [29]. The coarse landmarks not only provide the starting position, but also limit the changes of the transform throughout the optimization. Each time that the transform is changed in a way that causes the point pairing of the coarse landmarks to have an error above a certain threshold, an additional penalty is added to the objective function's calculation.

The objective function measures the distance of the physical points to the image space model after the points are transformed using the registration. The measure is often the distance from the transformed physical points to the nearest corresponding triangle in the image space model. However, some variants of ICP use an image space model comprised of points and calculate point-to-point distances. Greenspan et al take advantage of such a scheme by using a nearest-neighbor algorithm [31]. By using their proposed Triangle Constraint, they create an ICP variant that has a significantly better run-time performance. In practice, run-time performance is another important factor, but it cannot come at the expense of accuracy.

Another objective function used by Maurer et al converts the generic ICP algorithm into one that takes advantage of geometrical features [48]. In addition, each distance measurement is given a weight. The weights place emphasis on larger shapes in the surface model. They are also used to cull outliers as the optimization converges. In real specimens, outliers in the data set are common and can drastically affect the results of a registration. Ma and Ellis also create a robust variation of the ICP algorithm to better handle outliers [46].

In order for the algorithm to successfully find the proper transform, the points that are collected in physical space must be accurately picked on the bone with the tracked probe. This means that the probe must touch the bone directly when it collects the points. Phantom models often include only a plastic model of the bone, whereas cadaver specimens and live patients have tissue that may interfere with point collection. If points are captured on cartilage, the mapping from an image space model of the bone to a

physical bone will not be accurate. Touching the bone directly requires access to the bone and a pain-staking procedure that extends surgical time.

If the registration is not accurate, the robot may place the implant in the wrong position or orientation. It is critical to the life of the implant that this registration be clinically accurate. However, it is also important to maintain a minimally invasive and speedy approach. Surface matching, while accurate and less invasive than fiducial-based registration, may not be the least invasive option.

### 2.1.5 Registration Tracking Options

A critical component of any navigation system is its approach to tracking the physical object. Accuracy, ease-of-use, and invasiveness are criteria for selecting the tracking system. Most tracking options require a sensor component attached to the physical object and a nearby transceiver with which it will communicate. This communication provides a location of the tracked object. Each current approach has disadvantages. Electromagnetic trackers suffer from distortion by nearby metal instruments [80]. This renders it useless in a clinical environment in which metal instrumentation is ubiquitous. The most common approaches in clinical use are mechanical and optical tracking.

#### 2.1.5.1 Mechanical Tracking

Mechanical tracking involves the use of a mechanical arm with several joints that allow for enough degrees of freedom to easily locate fiducials on the patient (Fig. 2.6). Each joint is tracked by an encoder that can translate an angle into a voltage and, through

kinematic calculations, report back the resultant point of the tip relative to the base. The fiducial markers on the patient are selected in image space based on the preoperative image, and the arm selects the same points in physical space on the patient. The registration is created by matching the two data sets. The markers cannot move relative to the robot nor relative to the patient. Traditionally, this technique requires fixating the patient, as with a Mayfield clamp [33]. While this approach has a high degree of accuracy, the disadvantage is that surgery may be cumbersome due to the lack of patient mobility [33].

**Figure 2.6: A mechanical Viewing Wand navigation system (ISG Technologies Inc., Mississauga, Ontario, Canada) collects fiducial points that are attached to the patient's skin [33]. These points were in place during the preoperative scan. The positions of the markers in image space are matched with the positions of the mechanical arm after the captures are completed.**

2.1.5.2 Optical Tracking

Another commonly used tracking technique involves infrared stereoscopic cameras. In the case of passive optical tracking, several reflective markers are attached to

each of the patient's bones in a known configuration (Fig. 2.7). The camera sends out an infrared beam that is reflected by these markers, and this reflection is detected by the camera. Each of the two detectors on the camera recognizes the marker pattern using image processing software. The system triangulates the marker position and determines a location in three dimensions (Fig. 2.8). In the case of active trackers, a similar scheme is used except that the markers are actively emitting light rather than passively reflecting it. The system then reports a 4×4 transformation matrix that provides the tracker location in the reference frame of the camera (Table 2.1).

**Figure 2.7: Trackers and stereoscopic cameras work together to determine physical three-dimensional information [77, 81]. On the left, passive and active trackers are used in a study to determine the accuracy of optical tracking. These trackers are attached to the bone using stereotactic frames or bone pins and clamps. The left tracker is passive and has reflective spheres attached to the frame. The right tracker is active and has LED's embedded in the frame to generate a signal rather than reflect one. On the right, a stereoscopic camera (Northern Digital Imaging Inc., Waterloo, Canada) has two sensors that detect trackers and triangulate their position in three dimensions. Infrared beam emitters are located on the face of the camera for use with passive reflecting trackers.**

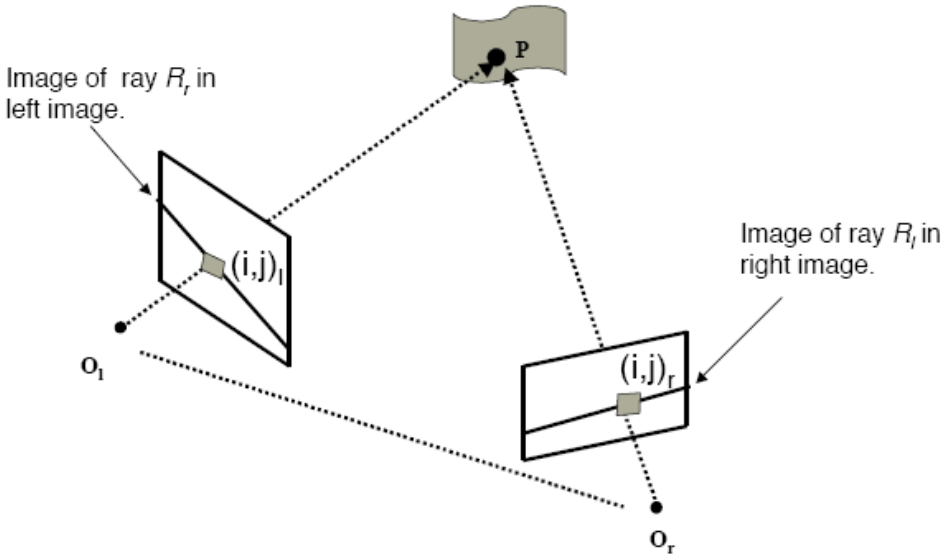


**Figure 2.8: Diagram of a stereoscopic camera capturing a tracker's position P in three dimensions [38]. The position is detected in two dimensions for each eye of the camera, indicated by $O_l$ and $O_r$. With $O_l$ and $O_r$ calibrated to each other, the camera triangulates the position in the two views to yield a three-dimensional coordinate.**

```
% $t track once
% $t fulltrans
0.38332969 -0.32828486 0.86330026 0.00000000 0.89938074 0.34537092 -0.26801717 0
.00000000 -0.21017283 0.87917459 0.42764401 0.00000000 114.58260345 -149.3006744
4 -1808.57470703 1.00000000
% exit
```

$$\begin{bmatrix} 0.383 & 0.899 & -0.210 & 114.583 \\ -0.328 & 0.345 & 0.879 & -149.301 \\ 0.863 & -0.268 & 0.428 & -1808.575 \\ 0 & 0 & 0 & 1 \end{bmatrix}$$

*Translation* = {114.583, −149.301, −1808.575}
*Scale* = {1.000, 1.000, 1.000}
*Rotation* = {−0.760, −1.042, −0.708}

**Table 2.1: Tracking matrix and its decomposition. In row one, commands using scripting language Tcl to retrieve a tracker position from a Polaris camera (Northern Digital Imaging, Inc., Waterloo, Canada). Tracker $t is a probe with three markers attached similar to the marker in Figure 2.7. The "fulltrans" command returns the full transformation of a tracker with respect to any references that were established. In this case, the camera itself is the reference. The resulting transform is a 16**

**element list representing the 4×4 matrix transform in column-major form. The transform assumes units of millimeters and radians. The final four elements show the translation vector with 114.58 representing the X-axis offset of the tracker from the camera, -149.30 representing the Y-axis offset of the tracker from the camera, and -1808.57 representing the Z-axis offset of the tracker from the camera. This implies the tracker was approximately straight ahead of the camera at a distance of about 1.8 meters. In row two, the same 16-element list converted to a 4×4 matrix transform format. In row 3, transform is decomposed into translation, rotation, and scale parameters using a "DecomposeTransform" command in the math library. The parameters listed include x, y, and z elements in that order. The translation is listed in units of millimeters and the rotation is listed in units of radians. The scale is not a factor since this is a rigid transform and that is shown in the scale values that would have no effect.**

The disadvantage to optical tracking is that it requires a direct line-of-sight from the camera to the trackers throughout the procedure. This can be a difficult limitation for cases that require surgical assistants to surround the patient during the procedure. Clinical settings are also difficult due to fluids and tissue that may dirty the markers. An obscured marker can induce inaccuracies or prevent tracking altogether. The camera is also limited by a frame rate of 30 Hz which means that any patient movement at a significant velocity could result in navigation errors.

## 2.2 Clinical Registration

Clinically, determining an accurate registration is a key step for many orthopedic procedures. Computer navigation is commonly used for hip, knee, spine, and cranium surgeries [3, 5, 14, 8, 41, 46, 63]. While some research has shown that a navigation system can be generically used for multiple anatomical areas [79], most systems are dedicated to a particular procedure or anatomical location. An overview of current navigation applications is shown in Table 2.2.

**Table 2.2: An overview of applications that provide surgical navigation and require registration.**

| Navigation System | Tracking Method | Registration Approach | Anatomical Object |
|---|---|---|---|
| BrainLAB VectorVision, [39] | Optical (passive trackers) | Fiducials attached by headband | Hip |
| Acrobot [6] | Mechanical | Region-based surface match | Hip |
| StealthStation TRIA Plus from Medtronic Surgical Navigation Technologies [1] | Optical (passive trackers) | Fiducial based (cutting tip registration) with fluoroscopy | Hip |
| MAKO Surgical Corp. | Optical (passive trackers) | CT-based Surface Match | Knee |
| BarinLAB VectorVision [68] | Optical (passive trackers) | Anatomic Landmarks | Knee |
| OrthoPilot [66] | Optical (active trackers including separate ankle tracker) | Anatomic Landmarks and Cutting Block landmarks | Knee |
| BrainLAB VectorVision [42] | Optical (passive trackers) | CT-based Anatomic Landmark Point Pair matching | Spine |
| CyberKnife Stereotactic Radiosurgery System [62] | X-ray cameras | Intraoperative X-ray matched to preoperative CT, augmented with a single implanted fiducial | Spine |
| Mazor Technologies Smart-Assist [63] | Mechanical | Intraoperative fluoroscopy matched to preoperative CT | Spine |
| Neurobot [16] | Ultrasound, MRI tracking | Preoperative planning MRI, Intraoperative MRI with fiducial stereotactic frame attached, and intraoperative ultrasound to detect brain shifts | Cranium and Brain |

### 2.2.1 Registration for Hip Surgery

Hip surgery provides a unique challenge for computer navigation due to the position of the bone deep within the tissue. Contrary to other orthopedic procedures, the

hip is not as easily accessible. If a mechanical pointer is used for registration, for example, it must puncture through thick layers of skin and fat to touch the bone [21]. Many of the registration techniques, however, remain the same for hip procedures.

Also similar to other procedures, registration for hip surgery can require invasive reference trackers. One study attempted to use trackers that were not rigidly attached to the femur with pins [39]. Researchers used a headband to hold the reference markers in place relative to the bone (Fig. 2.9). The headband was not able to maintain rigid position of the fiducials throughout the procedure. It concluded that the references suffered from significant independent motion when attached by the headband. While a less invasive approach remains a goal, accuracy must be maintained and rigid tracker fixation cannot yet be avoided.

**Figure 2.9: Headband with passive reflective markers for optical tracking [39]. The headband proved to be too mobile during the surgery to maintain a clinically accurate registration.**

Other researchers have used robots to reduce invasiveness. The Acrobot Navigation System enables a minimally invasive approach for hip resurfacing [7]. (Fig. 2.10) The procedure involves registering the femur with a tracked probe. Rather than have the patient immobilized, the Acrobot system uses a tracking mechanism so the system can continuously understand the patient location in a relative reference frame. While some systems like that of MAKO Surgical Corp. use optical tracking, the Acrobot system uses mechanical tracking. The patient is physically attached to the robot through the use of mechanical trackers that originate from the robot. The registration accuracy is approximately 1.5 mm of translation and 3 degrees of rotation.


**Figure 2.10: Acrobot navigation system incorporating a mechanical tracking arm and touchscreen display [6]. This system is used for hip replacement surgery. It employs a region-based surface-match registration.**

Some hip procedures involve revising failed implants. With revision total hip arthroplasty, cement must be removed from the femoral head. Researchers use navigation to precisely burr away the cement without causing any damage or fractures to

the bone [1]. They employ a StealthStation TRIA Plus from Medtronic Surgical Navigation Technologies which visualizes the bone using fluoroscopy. They show that a poor registration can greatly affect the results of cement removal with the navigation system (Fig. 2.11).

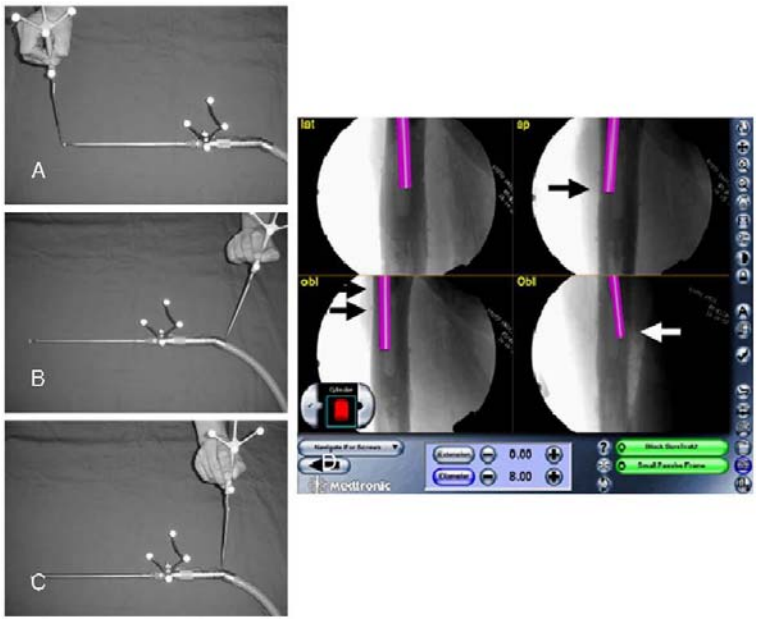


**Figure 2.11: A technical problem of registration of the high-speed burr [1]. Pointing at a tip of the high-speed burr with a probe (A). Registration of the long axis of the high-speed burr with a probe correctly (B). Pointing at a wrong place on the high-speed burr with a probe for registration (C). Incorrect registration produces trajectory angle difference between the virtual images and the real fluoroscopic images of the high-speed burr (D). The arrows indicate the trajectory of the high-speed burr in the femoral cortex.**

Incorrect registration can lead to dependence on a faulty navigation system. Another study confirmed this with a Stryker navigation system used in the registration of the acetabular component in a hip procedure [65]. In particular, the anterior pelvic plane can exhibit significant error if registration points are poorly collected. These studies underscore the importance of having an accurate registration and a registration procedure that is easy and robust.

### 2.2.2 Registration for Knee Surgery

MAKO Surgical Corp. uses a surface matching technique to register tibias and femurs during Unicondylar Knee Reconstruction (UKR) surgery in a procedure called MAKOplasty. The preoperative image space model is constructed by segmenting a CT of the patient. The registration is achieved with a surface match using specially designed pointers to handle cartilage and bony surfaces. The pointers collect points at particular prescribed positions on the surface of the anatomy. The registration is then used to guide a five degree-of-freedom robot to mechanically guide the surgeon in carving out the proper shape in the bone for an implant.

Similar robots exist that perform knee reconstruction. Sugita et al describe a seven degree-of-freedom robot that performs unicondylar knee arthroplasty [68] (Fig. 2.12). This system uses a BrainLAB VectorVision navigation system to register the optically tracked femur and tibia. The system requires the user to locate anatomical landmarks using a tracked pointer. The final resulting cutting accuracy shows rotational errors of less than two degrees and a “flatness” measure of less than 0.1mm error.

**Figure 2.12: Seven degree-of-freedom robot using a preoperative plan and registration to perform Unicondylar Knee Arthroplasty (UKA) [68]. The robot is shown poised over a patient's knee. The registration and navigation components are provided by a BrainLAB VectorVision system. The robot uses an optical tracking system to locate the pointer for registration.**

The registration accuracy is tied to the accuracy of the points collected. Yau et al researched the accuracy of anatomic landmarks collected relative to a fiducial-based gold standard registration [82]. Again, the navigation system of choice is a BrainLAB VectorVision which uses optical tracking components and anatomic landmark registration points. In the case of the knee, the landmarks included: tibia and femur knee centers, medial and lateral femoral epicondyles, and medial and lateral malleoli. They found that the epicondyle points were significantly in error. For this reason, the anatomic landmarks alone cannot yield an accurate registration in knee reconstruction. However, they also found that the mechanical axes were reasonably aligned relative to the gold standard. This is especially important since landmarks often define the mechanical axes even in systems that capture more points during a more detailed surface match.

Another study used a different navigation system, OrthoPilot, for its computer-assisted total knee replacement experiments [66]. Similar to VectorVision, this system is optically tracked and requires a few anatomic landmarks to be captured. It includes a special device to capture the ankle center (Fig. 2.13). It also requires capturing hip center and a kinematic knee center by extending and flexing the leg. Other landmarks are captured which are specific to orienting cutting blocks to guide the knee resection. The landmark approach used by OrthoPilot resulted in registrations with high variability, often due to user inexperience and patient deformity. Despite this inconsistency, the study still concluded that the navigation system provided an added benefit over conventional surgery and radiograph based planning.

**Figure 2.13: Optically tracked device for capturing ankle center [66]. Instead of capturing the medial and lateral malleoli and calculating the ankle center from that, this device can more accurately determine the ankle center based on kinematic motion of the ankle joint. This leads to a more accurate rough registration which provides a better initial guess for the registration routine.**

### 2.2.3 Registration for Spine Surgery

Computer assistance in spine surgery presents problems due to multiple implants being placed and multiple patient positions being used. Lee et al used a point-pair

matching technique by selecting anatomical landmarks on the vertebrae and comparing them to a preoperative CT scan [42]. Changing patient position from prone to supine can disturb the registration, and they found that re-registering the patient for each new instrumented level of the procedure yields better results. The final registration was then used to guide the entry of the beginning of the spinal procedure (Fig. 2.14).

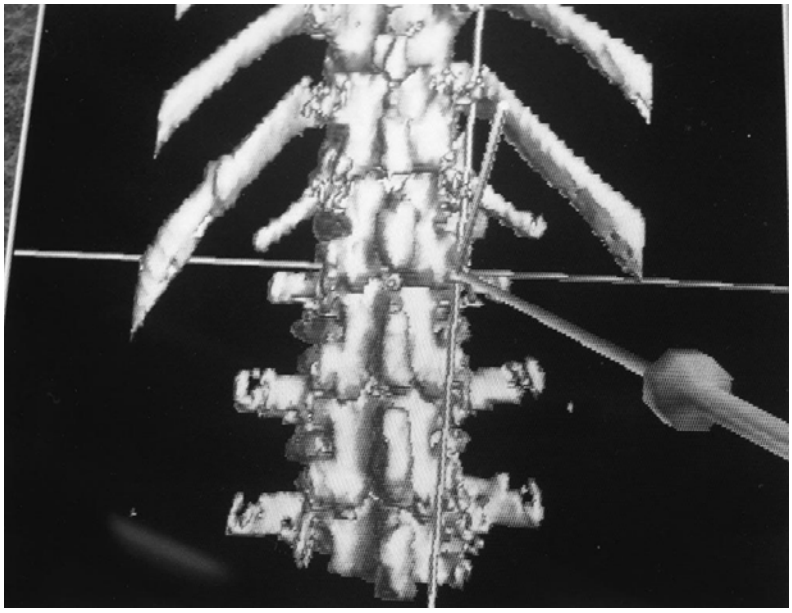

**Figure 2.14: Spinal navigation [42]. After successful patient registration, spinal navigation begins by using the registration pointer to touch the planned entry point. The monitor on the workstation depicts this step in real time.**

In order to improve accuracy and robustness, Russakoff et al experimented with a hybrid registration approach by implanting a single fiducial to augment an intensity-based 2D-3D registration (Fig. 2.15) [62]. Fiducial-only registration techniques are typically invasive as the markers must be implanted in the bone and spread across a considerable region to maintain accuracy. On the other hand, intensity-based solutions often suffer from finding sub-optimal solutions as they may get stuck on local optima. Russakoff et al found the hybrid results provide a greater convergence rate for the

registration algorithm, thereby avoiding local optima solutions, without greatly increasing invasiveness since only one fiducial was used.

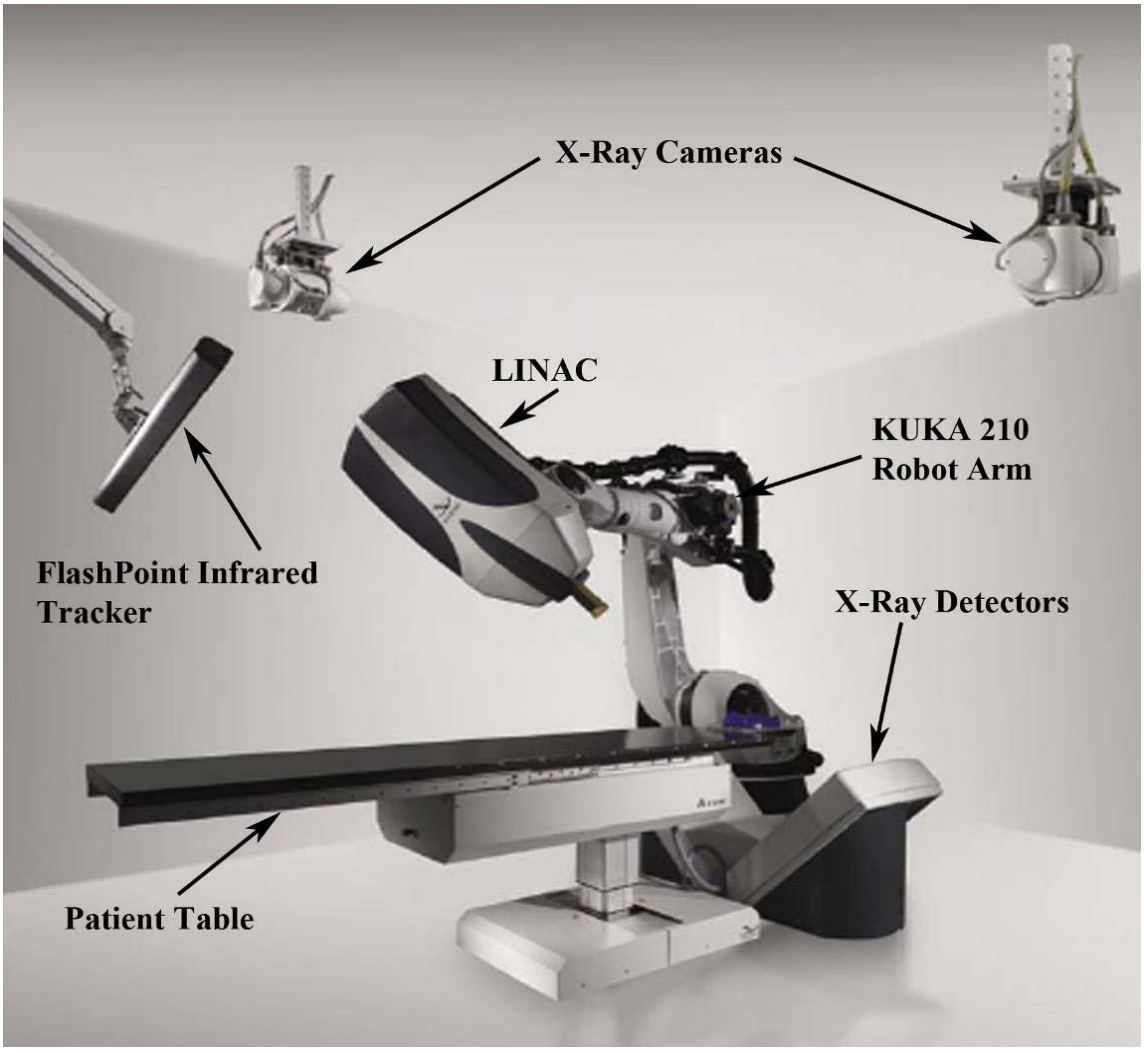


**Figure 2.15: CyberKnife system with 2D-D registration. Russakoff et al used a CyberKnife guided radiotherapy system to experiment with alternate registration techniques. They augmented a 2D-3D X-ray-based registration pattern with a single fiducial. This hybrid approach between surface matching and fiducial-based registration yielded a better registration convergence without drastically increasing the invasiveness of the procedure through the use of multiple fiducials. This image is taken from a thesis from the Catholic University of America [78].**

Another solution to the problem of multiple implants involved an ability to adjust the assisting robot intraoperatively [63]. Mazor Technologies developed the SmartAssist robot that attaches to a clamp that is rigidly mounted on the spine. The clamp is

registered to the bone using pre-operative CT and intra-operative fluoroscopy. The robot can be placed in three different locations on the clamp without requiring a re-registration, thereby allowing for multiple cuts without registering each time.

### 2.2.4 Registration for Cranial Surgery

Cranial surgery includes several procedures that benefit from surgical navigation, such as operations on the nasal cavity, ear, and skull base [75]. Various registration methods and mechanisms have been developed for fiducial approaches and laser scan based surface matching. Custom mouthpieces can be used since teeth are rigidly attached to other parts of the skull that may be operated on. Registration is especially important with cranial surgery since critical structures are close to the surgery site. Using the registration, several robotic systems assist surgeons with cranial surgery [75].

One such system is the Neurobot [16]. Neurobot is a robot with four active degrees-of-freedom. It uses active constraints to restrict the surgeon in making cranial cuts so the surgeon is ultimately still in control. The registration scheme involves one MRI for planning and a second MRI after a stereotactic frame with fiducials is mounted. The robot is registered to the frame using a fiducial-based registration. The two MRI data sets are co-registered so the planning information can be used intraoperatively. Ultrasound images are captured during surgery, and automatic feature extraction connects the ultrasound images to the second MRI. This allows the system to understand how the brain shifts during surgery.

### 2.3 MAKO Surgical Corp.'s System

MAKO Surgical Corp. employs a semi-active five degree-of-freedom robot paired with a computer navigation system that accurately guides a surgeon for placing knee implants during unicondylar knee arthroplasty (UKA). The system includes the robot with its controller, a computer that provides the user interface and algorithm implementation for registration and segmentation, and an infrared camera that stereoscopically detects trackers with reflective spheres. The surgeon attaches trackers to the tibia, femur, and robot so each component can be tracked throughout the procedure (Fig. 2.16). The surgeon will register each tracked component, which allows the robot to understand where it is relative to the patient. Using a preoperatively determined surgical plan for the position and orientation of the implants, the robot can assist the surgeon in executing the cuts precisely according to plan.

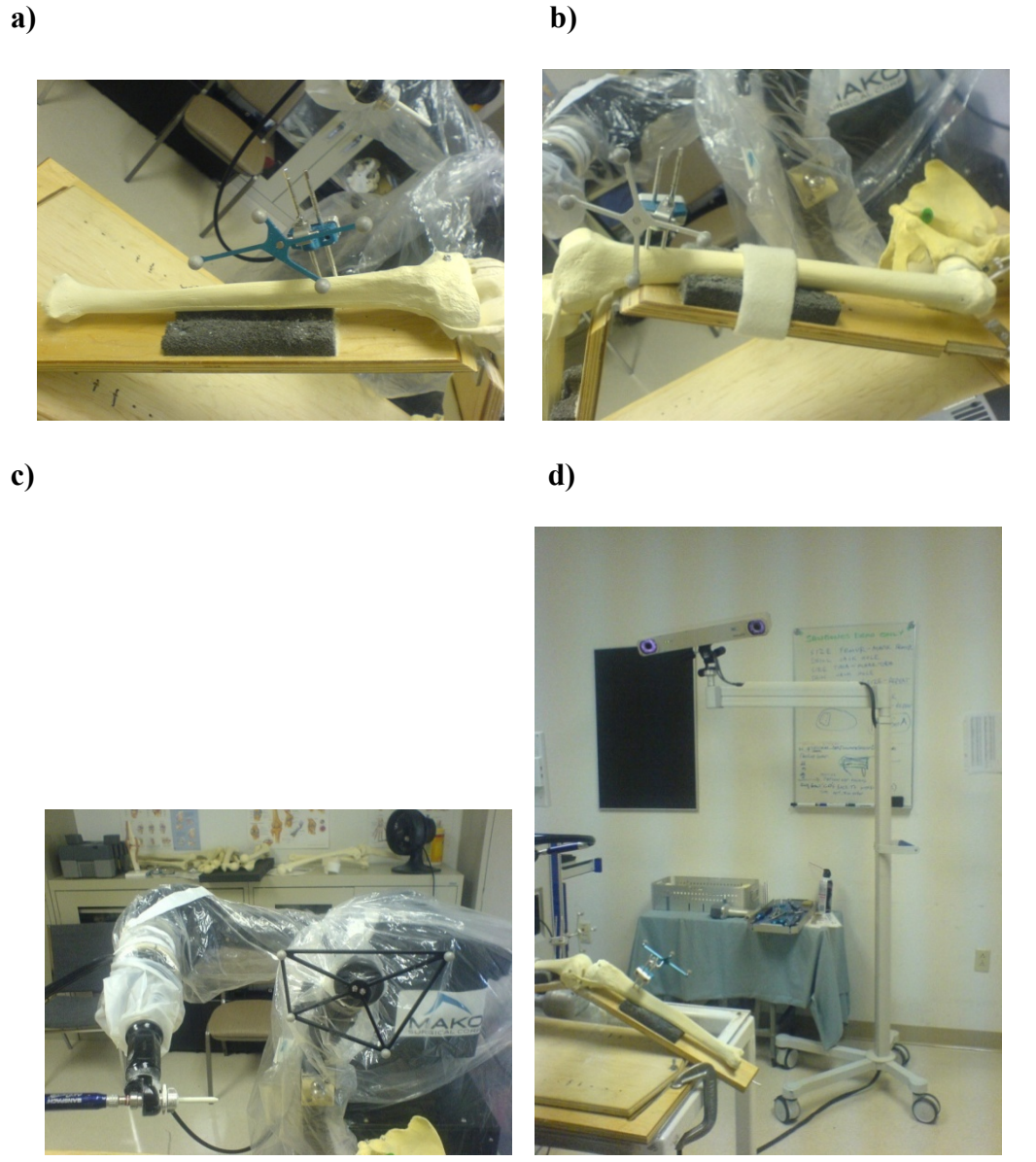


**Figure 2.16: MAKO Surgical Corp.'s approach with a camera tracking a tibia, femur, and robot. a) A phantom tibia with a 4-sphere tracker pinned to the bone. b) A phantom femur with a 4-sphere tracker pinned to the bone. c) The robot manipulator arm with cutting device attached and 4-sphere tracker fixed to the base. d) Infrared camera (Northern Digital Imaging Inc., Waterloo, Canada) that has a view of all three trackers. Infrared LED's can be seen emitting light from the camera "eyes".**

## Chapter 3: Ultrasound and Applications in CAOS

### 3.1 Ultrasound Principles

Ultrasound provides an alternative to the direct probing that is common to most registration procedures. Ultrasound imaging is the use of sound waves to detect differences in material density. It is based on the principle that sound travels at different speeds through materials of different densities. By knowing the speed of sound through a material, one can use ultrasound to measure or image that material. If the material is purely homogenous, the beam will pass through it cleanly at the known speed. If there are defects or other materials along the beam's path, a reflection will be created every time it encounters an inhomogeneity. A greater transition in acoustic impedance in the material yields a greater reflected signal. The amplitude of the reflection is described by Equation 3.1:

$$R = \left(\frac{Z_2 \cos\theta_i - Z_1 \cos\theta_t}{Z_2 \cos\theta_i + Z_1 \cos\theta_t}\right)^2 \qquad \text{(Eq. 3.1)}$$

where $Z_1$ and $Z_2$ are the acoustic impedances of the two mediums and $\theta_i$ and $\theta_t$ are the angle of incidence into the interface and angle of transmission out of the interface as seen in Figure 3.1 [67].

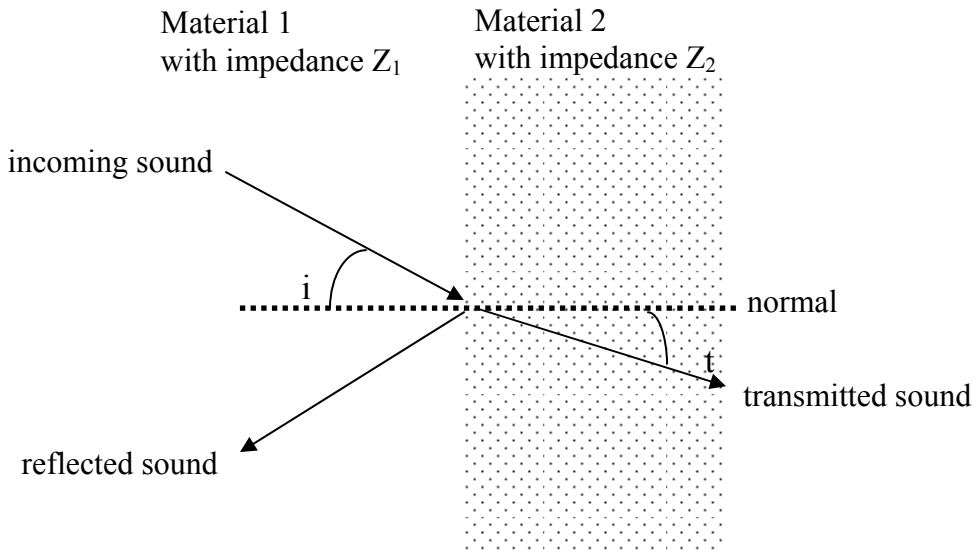


**Figure 3.1: Diagram of a beam of sound travelling from a material of one impedance into a material of a different impedance. The coefficient of reflection is determined by the two impedances, the angle of incidence ( $_i$), and the angle of transmission ( $_t$) as described by Equation 1.1.**

The amount of time it takes for the reflection to return to the point of origin of the beam determines the distance of the source of the reflection to the origin of the beam. The distance is calculated using the equation:

$$d = \frac{vt}{2} \qquad \text{(Eq. 3.2)}$$

where d is the distance to the target signal, v is equal to the velocity of sound in the material, and t is the amount of time it takes for the beam to get to the target and reflect back to the source. Sound travels faster in material that is denser. The speed of sound constant is shown for various tissues in Table 3.1.

| Tissue Type | Speed (mm/ s) | Density (g/cm$^3$) |
|---|---|---|
| Connective | 1.613 | 1.120 |
| Muscle | 1.547 | 1.050 |
| Fat | 1.478 | 0.950 |
| Adipose | 1.450 | 0.950 |
| Blood | 1.584 | 1.060 |
| Brain | 1.560 | 1.040 |
| Breast | 1.510 | 1.020 |
| Eye: lens | 1.645 | 1.070 |
| Eye: vitreous | 1.528 | 1.010 |
| Kidney | 1.560 | 1.050 |
| Liver | 1.595 | 1.060 |
| Muscle, cardiac | 1.576 | 1.060 |
| Muscle, skeletal | 1.580 | 1.050 |
| Skin | 1.615 | 1.090 |
| Fatty | 1.465 | 0.985 |
| Non-fatty | 1.575 | 1.055 |
| Blood cells | 1.627 | 1.093 |
| Blood plasma | 1.543 | 1.027 |
| Eye: cornea | 1.586 | 1.076 |
| Spinal Cord | 1.542 | 1.038 |
| Spleen | 1.567 | 1.054 |
| Testis | 1.595 | 1.044 |
| Mean | 1.561 | 1.043 |
| St. Dev. | 0.051 | 0.042 |

**Table 3.1: The speed of sound constants through various tissue types (Modified from Goss et al [30]). The speed of sound varies based on density. The mean speed from this particular study is 1.561 mm/ s although other studies have found a mean of 1.54 mm/ s.**

### 3.1.1 Ultrasound Hardware

Creating an ultrasound beam involves the use of a transducer to convert electrical energy to mechanical energy via a crystal, which vibrates at a known frequency when electricity is applied. That same crystal can receive the signal as the sound waves are bounced back from the target material and convert it back into electrical energy (Fig. 3.2). The received electrical signal can then be processed by a computer and interpreted as distances or image intensity, depending on the imaging mode.

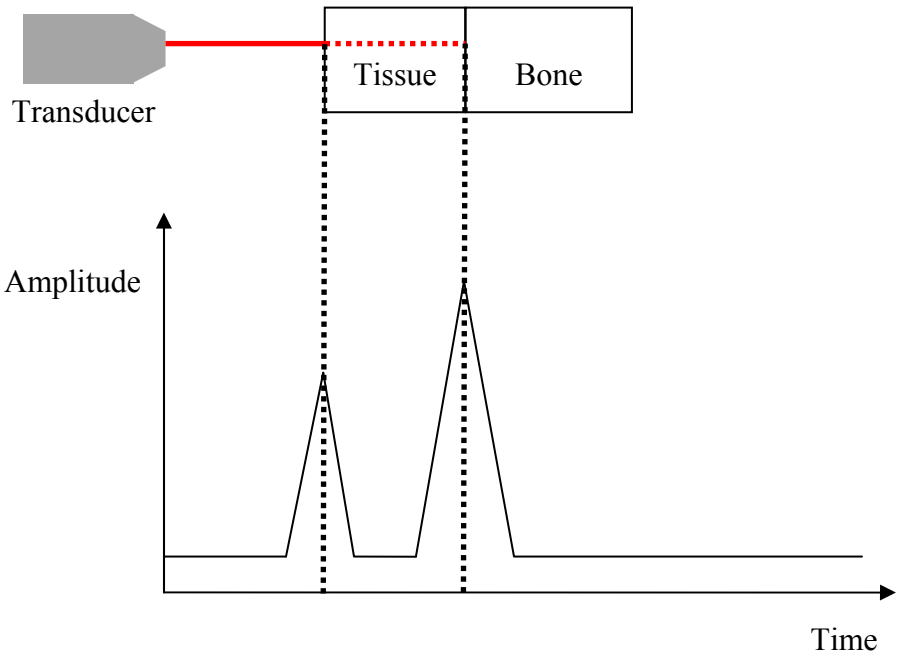


**Figure 3.2: An ultrasound transducer sends a beam into various materials and receives a signal that correlates the time of the sound beam travel with the distance that the beam travels. In this case, the first tissue interface reflects back a peak and the interface between the bone and the tissue also reflects back an even greater peak due to a greater difference in impedance. The distance between the peaks indicates tissue thickness and the distance from the source to the bone peak indicates bone depth.**

The transducer has several properties that determine how effective it is. Axial resolution is the resolution along the axis of the beam. Lateral resolution is the resolution perpendicular to the axis of the beam (Fig. 3.3). The frequency can determine what axial resolution the beam will have as well as how deep the beam will penetrate. A high frequency signal will only penetrate to a shallow depth, but have high resolution. Conversely, a low frequency signal will penetrate deeply but sacrifice resolution. Typical frequencies for ultrasound applications for medical imaging are within the 1 – 7 MHz range. Higher frequencies (between 10-30 MHz) may be used for shallow imaging applications that require a greater degree of accuracy.

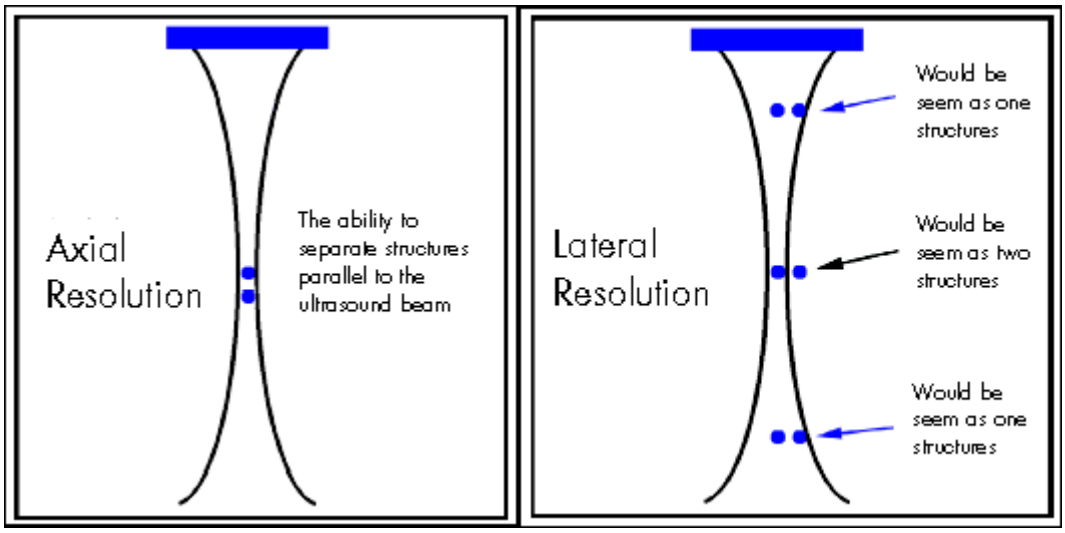


**Figure 3.3: Axial and lateral resolution of an ultrasound beam. Axial resolution determines the ability of an ultrasound system to distinguish between objects that lie along the axis of the beam. Axial resolution is affected by frequency. Lateral resolution determines the ability of an ultrasound system to distinguish between objects that are next to each other on a plane perpendicular to the axis of the beam. Lateral resolution is affected by transducer element size and focusing. Image is taken from Dumond [22].**

Focal length is another property of the transducer that will have an effect on accuracy, particularly lateral resolution. Various focusing methods can be chosen ranging from spherical to cylindrical or none at all. Spherical focusing will cause the beam to converge down to a point, and the beam will then diverge after that. Cylindrical focusing will cause the beam to converge to a line and diverge from there. Without any focusing, the beam will be nearly as wide as the crystal element diameter. The narrower the beam is, the better the lateral resolution will be and the closer it will come to the approximation of the beam being an infinitely thin line.

The beam must also be directed in such a way that the beam angle of incidence to the target is close to zero degrees [2]. This ensures a maximum reflection. An angle of incidence higher than 45 degrees can result in negligible reflections and a poor ultrasound image. Transducers may have an optional standoff which can cause the alignment of the

transducer to the target to be even more difficult. The standoff allows the face of the transducer to be set back from the target in case the target would be too close to the source of the beam. The near field and ring-down region of the transducer should be avoided for accurate measurements and so a standoff may be necessary. Standoffs include hardware that is built into the transducer to match the impedance of the desired target as well as gel or other objects that can be held in place between the transducer and the target.

### 3.1.2 Ultrasound Modes

The common forms of ultrasound used clinically are B-mode, which is a two-dimensional imaging modality, and M-mode, which is used for measuring temporal differences in density. B-mode is based on an array of crystals, each of which sends a single beam of ultrasound. It is commonly used for monitoring fetal development, measuring prostate volume, and a host of other non-invasive imaging procedures [51]. M-mode uses temporal differences to measure changes. A third mode, A-mode, is a one-dimensional beam. With A-mode, the signal can be interpreted as distances to the borders of various targets along the beam's path. It is less useful for imaging various anatomical structures, but it is ideal for probing percutaneously. The A-mode signal is simple and relatively easy to analyze.

Determining the velocity component in Equation 3.2 is key to accurately analyzing an A-mode signal in any given medium. The speed of sound in water is 1450-1550m/s, depending on temperature and pressure, and in human tissue has experimentally been found to be approximately 1540m/s [44]. Fat and muscle present different densities

and therefore different speed constants, in the range of 1500-1600m/s [30]. However, while human tissue is not perfectly homogeneous, the varying speed constants should not greatly affect the overall accuracy. Amstutz argues that for small distance measurements, as is the case for the distal femur and proximal tibia, the variation has a minimal effect [3].

This can have clinically relevant results, however, as researchers have found that groups of patients can have differing average ultrasound velocities [69]. While age is not a considerable factor, gender has a noticeable effect likely due to the higher fat content in muscles of women. Patients' conditions can also be a factor in the speed of sound in tissue as edemas proved to decrease the velocity. While most patients seem to fall safely in an acceptable range, an inaccurate speed of sound through tissue could be a source of error that will be hard to correct intraoperatively.

### 3.2 Ultrasound Registration

By using A-mode ultrasound, researchers have been able to collect points for computer-navigated surgery without requiring direct access to the bone [3, 28, 36]. An A-mode ultrasound solution includes an ultrasound transducer affixed with a tracked array that is visible to the camera in addition to the normal registration components such as the stereoscopic camera and image space model of the physical object (Fig. 3.4). The tracked ultrasound transducer is essentially a variable length pointer, where the distance to the tip would be measured by properly filtering the ultrasound signal. A calibration allows for the conversion of the point found by the signal into the space of the optically tracked reference markers.

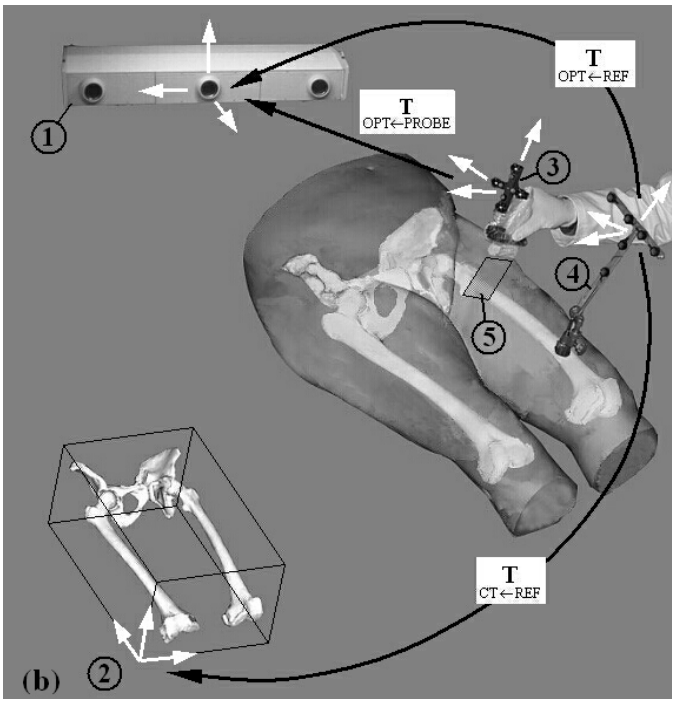


**Figure 3.4: Schematic of the setup used for ultrasound-based registration during orthopedic surgery: (1) Optical localizer; (2) Segmented CT scan (Image Space); (3) Tracked Ultrasound probe; (4) Bone-implanted dynamic reference object (Physical Space); (5) Ultrasound image. The rigid-body transformations between the 3D coordinate systems of the various components are indicated by the black arrows [4].**

Researchers have tried to develop ultrasound solutions to registration [3, 4, 12, 13, 18, 28, 35-37, 49, 50, 74]. Several steps are needed in order to add an ultrasound device to a navigation system. The ultrasound device must first be calibrated so the relationship between the tracker seen by the camera and the beam source and direction is known (Fig. 3.5). Then, a processing algorithm must be developed to interpret the signal so the position of the bone in the signal is known. For B-mode ultrasound, this involves segmentation of a two-dimensional image to determine a bone surface in the image. Automating B-mode segmentation is difficult but necessary for clinical acceptance [2]. For A-mode ultrasound, it requires interpreting a one-dimensional signal so a distance to the bone can be found. Once that information is known, it must be matched to the

preoperative image data using some sort of optimization routine. An accurate and robust matching is determined by accurate data samples as well as choosing geometrically unique features on the bones.

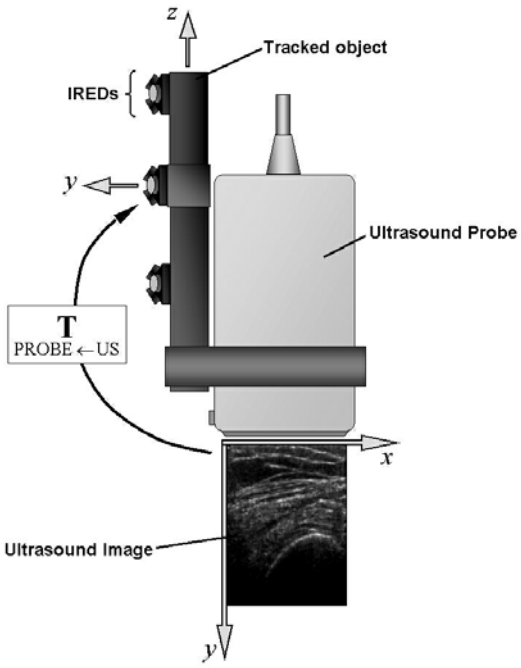


**Figure 3.5: A tracked B-mode US probe with attachment for freehand 3D US imaging [4]. A calibration is required to convert from the x-y space of the image to the x-y-z space of the tracked object. The calibration transform is shown here with a black arrow and the label $T_{UStoProbe}$.**

### 3.2.1 Ultrasound Calibration

Researchers have calibrated ultrasound devices with a few different methods. Some calibrate a full transformation, both rotation and position, while others focus only on translation and assume the axis of the beam is along the housing of the transducer, which can be easily measured. Bass calibrates an ultrasound probe by combining a normal pivot calibration for an optically tracked probe with a custom fixture that will measure the offset of the beam origin (Fig. 3.6) [8]. This assumes that the transducer will

precisely replace the probe tip in such a way that the face of the transducer will be centered at the original position of the probe tip. The procedure then determines an offset by measuring a sample signal, and this makes another assumption that the beam is aligned along the axis of the transducer housing. Rousseau discusses the use of a plane phantom to calibrate a B-mode scanner [60]. Each B-scan is filtered to determine the position of the phantom using intensity and gradient information. The data points are used by the Levenberg-Marquardt optimization algorithm to determine the calibration [43].

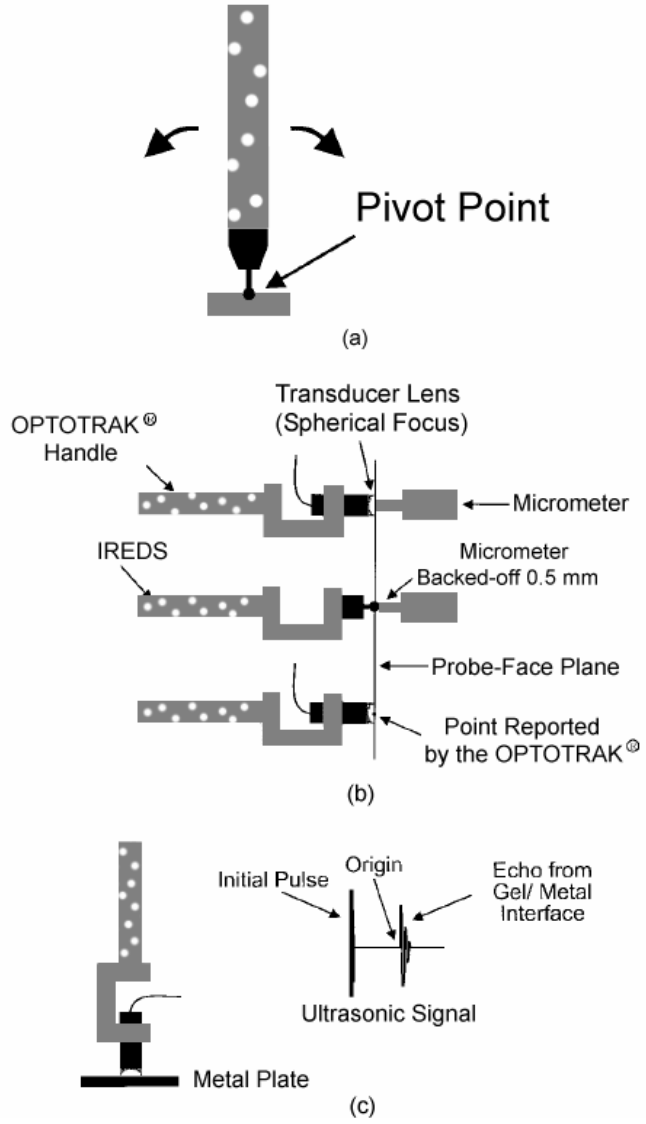


**Figure 3.6: Bass's description of an A-mode ultrasound calibration routine using OPTOTRAK optical tracking with active infrared emitting markers (IRED's): The procedures used to calibrate the pointer probe and the ultrasonic probe. (a) The normal OPTOTRAK calibration procedure in which a pointer probe is "pivoted" while the center of the spherical pointer tip does not move. This allows the OPTOTRAK to determine the pointer tip location relative to the IRED's. During normal operation, the center of the pointer tip is reported as the probe position. (b) The ultrasonic probe alignment procedure. While the probe is firmly held in a fixture, the micrometer is moved to be flush with the probe-face plane. The ultrasonic transducer is then replaced by a pointer probe. The center of the spherical pointer tip is aligned with the probe-face plane by backing-off the micrometer by the radius of the sphere. The probe can then be calibrated using a normal OPTOTRAK calibration as in (a). (c) The procedure for determining the ultrasonic signal origin relative to the probe-face plane. The large gel/metal echo occurs at the probe-face plane; the beginning of this echo serves as the origin of the ultrasonic signal for calculating the physical position of echoes relative to the position of the probe. Diagram is taken from dissertation from Vanderbilt University [8]**

### 3.2.2 Ultrasound Signal Processing

Once a calibration is determined, algorithms must be used to segment the ultrasound data and find the bone surface in the signal so that it can be registered. For A-mode signals, Bass uses a standard deviation window to process the signal (Fig. 3.7) [8]. The result is an envelope of the original signal that can be filtered by looking for peaks in contiguous regions. For B-mode imaging, Ionescu refers to low-level and high-level segmentation. He uses a watershed algorithm first and performs an additional optimization to further filter the data set (Fig. 3.8) [37]. Other researchers use active shape models (ASM) to find the bone shapes in the ultrasound scans. This consists of adapting a deformable template of the bone based on a training set to the intensity data in the B-mode images from a particular patient [35].

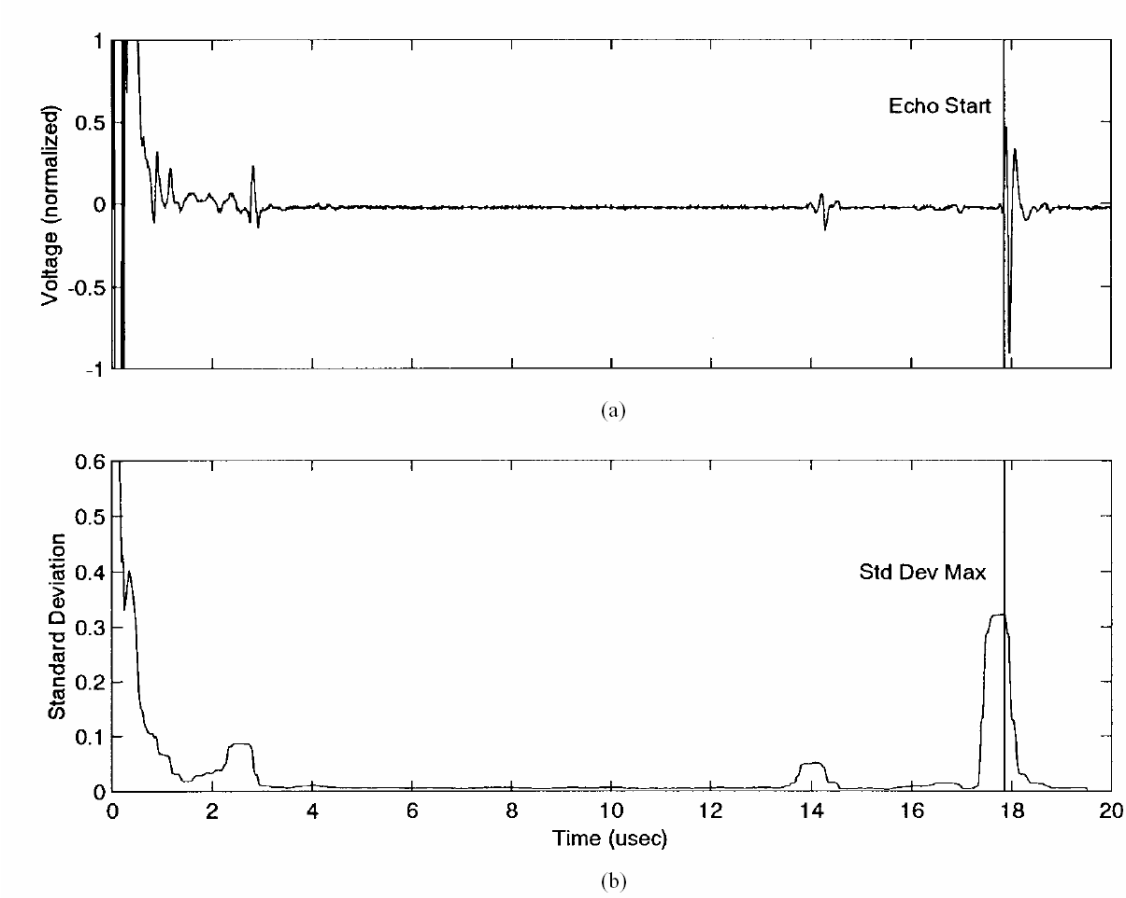


**Figure 3.7: On top, an original A-mode ultrasound signal shows a significant peak in the raw data [8]. On the bottom, the signal is processed by passing a 0.5-μs-wide standard-deviation window over the original signal to yield an envelope signal that is easier to process.**

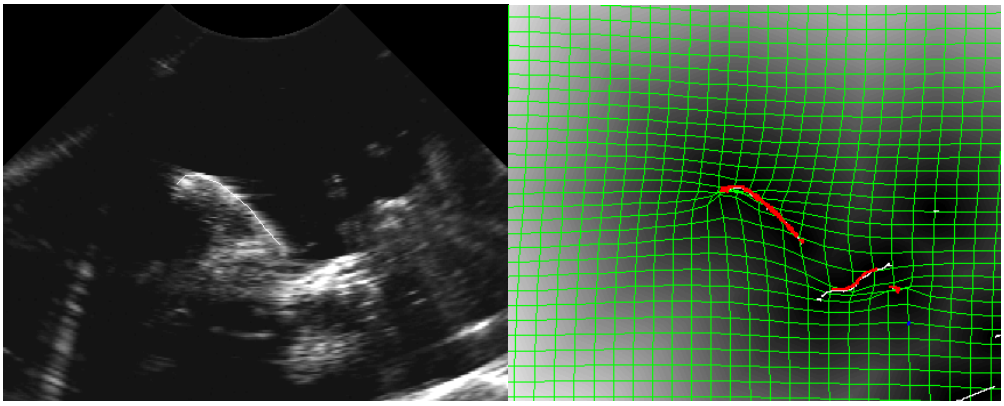

**Figure 3.8: Typical ultrasound images (left) and 2*D*/2*D* elastic registration (right) of a vertebra [47]. This two-dimensional segmentation can be significantly more complicated than the one-dimensional segmentation shown in Fig. 3.7.**

### 3.2.3 Ultrasound Registration Advantages

While registration is clearly a crucial step to receiving the benefits of computer assisted navigation, the invasiveness of common registration techniques can be prohibitive. Fiducial approaches require implanted markers that must be in place prior to the patient scan. Surface match approaches may need larger incisions to access geometrically unique anatomical features to constrain the registration [58], thereby negating the benefits of a potentially minimally invasive surgical technique. Ultrasound, however, offers a minimally invasive approach when combined with surface matching. It can image the bone percutaneously. It can access anatomy that is otherwise difficult to reach or even completely out of the scope of the procedure, as was the case for distal femur points during hip replacement [36].

Ease of use is another benefit of ultrasound registration. Ultrasound imaging is a simple scanning process. This can reduce the time it takes to collect all the data points [58]. This differs from surface matching which may require the surgeon to collect points on the surface of the bone in a precise pattern to guarantee a robust registration. Fiducials, while easy to touch intraoperatively, may be difficult to implant.

Being easier also leads to another practical advantage. The surgeon's time is critical and ultrasound scanning can be accomplished by a physician's assistant. This allows the patient to be registered before the surgeon walks into the operating room, saving critical minutes. On the other hand, implanting fiducials and collecting anatomical landmarks precisely will likely always be in the realm of the surgeon.

### 3.3 Ultrasound Registration Clinical Application

In cranial procedures, A-mode ultrasound was used to register the bone beneath the scalp [8]. The method used a tracked A-mode probe to capture data points on the skull without making an incision through the scalp (Fig. 3.9). The tracked A-mode ultrasound transducer scanned the surface of the scalp and captured signals over previously implanted fiducials. The fiducial location was determined by processing the ultrasound signals. This was shown to have clinically equivalent accuracy to a fiducial-based registration approach that used a mechanical probe to touch the fiducials (Fig. 3.10).

**Figure 3.9: Bone surface points are collected transcutaneously using the A-mode ultrasound probe [3]. For acoustic coupling, gel was applied. A dynamic reference base, consisting of 2 separate marker carriers, each with 4 infrared light–emitting diodes, is attached noninvasively to the upper teeth by a silicon mold.**

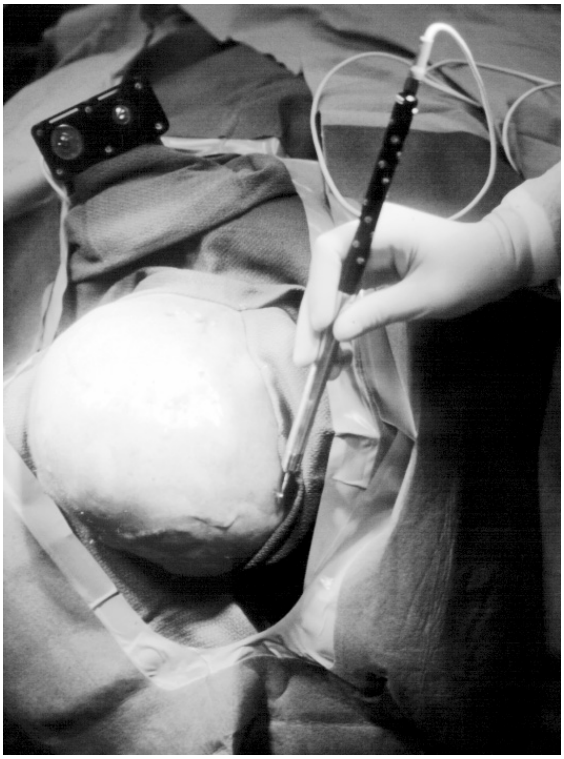

**Figure 3.10: A tracked probe touches fiducials implanted into the cranium [8]. This provides the ground truth registration method for A-mode ultrasound tests.**

In hip surgery, Heger et al used A-mode ultrasound to augment the registration of the proximal femur [36]. When a hip is being replaced, the surgeon has access to the proximal femur to collect points directly with a probe, but additional points on the distal femur would increase the accuracy of the registration by better defining the mechanical axis of the femur. Using A-mode ultrasound, researchers were successful in capturing additional points on the distal femur near the knee for the registration of the femur near the hip. This improved the overall registration.

Some research has been conducted to apply A-mode ultrasound for knee surgery, which includes registering the distal femur and proximal tibia [28]. However, little of this research addresses the challenge of real specimens. Real specimens present problems of accessibility. Few studies have validated an ultrasound approach to human

specimens [5]. Some researchers have explained the difficulty in using B-mode ultrasound with real specimens. The segmentation proves to be more difficult, as expected, since each signal is more complex. Diekomien et al found that they had to visually inspect the ultrasound scans and did not provide an automated solution for segmenting bone in the ultrasound [18]. The selectivity of the ultrasound in the work underscored the need to use only highly accurate ultrasound scans in order to yield an accurate registration.

Amin et al used standard B-mode ultrasound and an automated segmentation method to register the pelvis for hip surgery [2]. By comparing to a surface match solution, they determined the accuracy of their approach to be within 3mm translational error and 2 degrees of rotational error. They used the B-mode image to provide feedback to the surgeon regarding the quality of the image being captured. This improved the quality of the captured data by guaranteeing that the image had strong reflections.

Another way to improve the registration is to alter the image space model of the patient. Some researchers found improvement in registering the spine by adjusting the surface model of the vertebrae to only include areas that the ultrasound could reach [13]. Their model started with using a threshold filter on a CT data set (Fig. 3.11). By assuming the direction of the ultrasound beam, they could remove parts of the surface whose normals would clearly not be reachable by the beam. This reduced the chances that they could mistakenly match the ultrasound scan to surfaces in the CT.

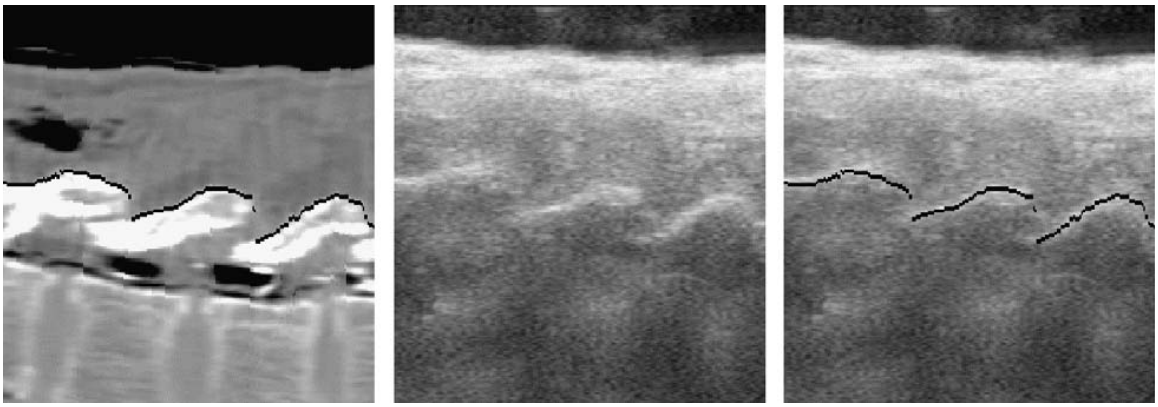

**Figure 3.11: Estimated surface and corresponding ultrasound data [13]. Left: sagittal CT slice of the laminar arc (human lumbar spine). The black line marks the estimated surface. Middle: corresponding ultrasound slice. Right: overlay of estimated surface and ultrasound slice.**

Other experiments have used custom ultrasound devices to acquire intraoperative images. One such device was the ULTRACUBE of the Ro-Med System (Fig. 3.12) [74]. This was a navigation system coupled with an autonomous robot for pedicle screw insertion. The intraoperative ultrasound provided real-time updates to the registration which gave the surgeon the ability to move the patient, in contrast with other autonomous robots which require fixed positions. The system achieved this by segmenting the intraoperative ultrasound data and registering it to a preoperative CT data set. Ultimately, the ultrasound registration showed promise but fell slightly short of what would be needed for clinical accuracy, due in part to a segmentation error of 1.5mm.

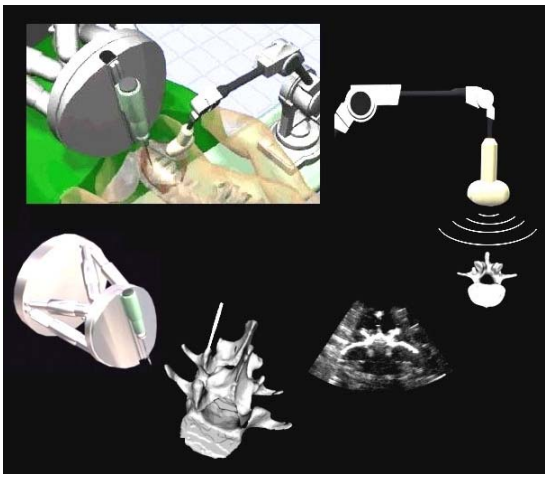

**Figure 3.12: The Ro-Med robot concept (clockwise through the image) - Overall system; Intraoperative record of the contour of the vertebral body; US-image of the contour; Identification of the contour in the preoperatively generated 3d-model based on Spiral-CTdata; d) control of the Robot [74].**

Another custom ultrasound device, the AcouStick, was used for cranial registration (Fig. 3.13) [50]. They performed experiments on phantom specimens augmented with gel to mimic tissue and on human specimens. They found a total registration error in the range of 1-2mm. This demonstrates that easily accessible bone provides a good opportunity for ultrasound registration.

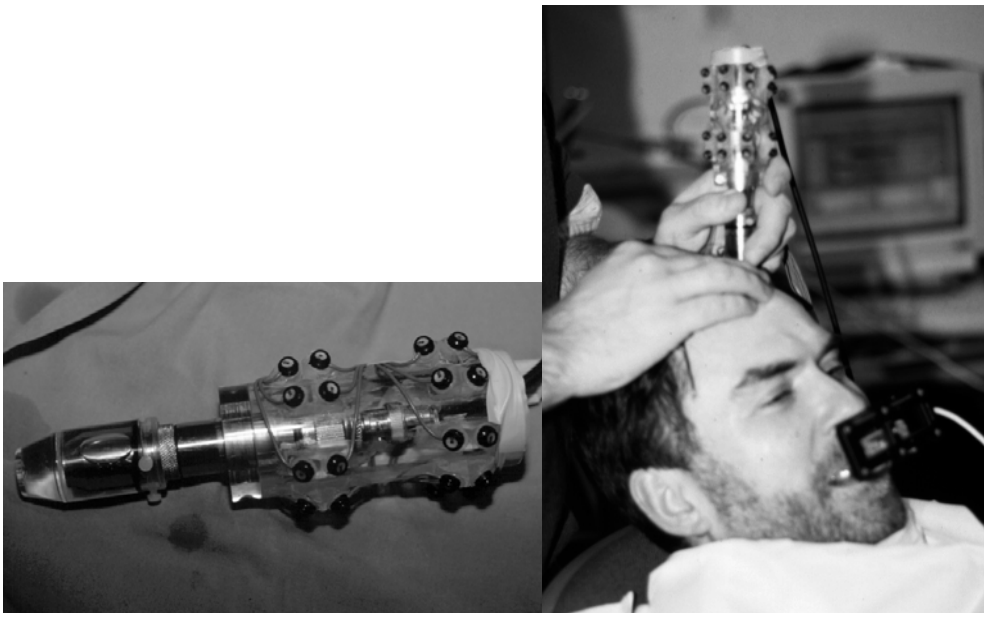

**Figure 3.13: AcouStick ultrasound transducer and it being used in vivo[50].**

A-mode ultrasound is also used for robot-aided surgery using the CRANIO system [58]. Using an anatomical landmark registration as an initial guess, researchers used A-mode ultrasound with a surface match algorithm to register the cranium. They were able to achieve an accuracy of better than 2.5mm. This surpassed attempts using only anatomical landmark and attempts using surface match with a pointer. The fiducial approach was still significantly more accurate than ultrasound, but they argue that it comes with an added cost of increased time and invasiveness.

## Chapter 4: Materials and Methods

An A-mode ultrasound registration system is developed in conjunction with a navigation system developed by MAKO Surgical Corp. Three critical components comprise the A-mode ultrasound registration system: the A-mode ultrasound hardware, the calibration of the ultrasound transducer to its tracker, and the registration signal processing as it applies to phantoms and specimens. The calibration enables captured data to be converted from the coordinate space of the transducer into the coordinate space of the camera. This system then captures data (Fig. 4.1) to be registered to a CT-based computer model for phantoms and specimens. An accurate registration of the two data sets is dependent on the quality of each set. The signal processing is designed and implemented to automate the data collection so the system has clinical utility as well as accuracy.

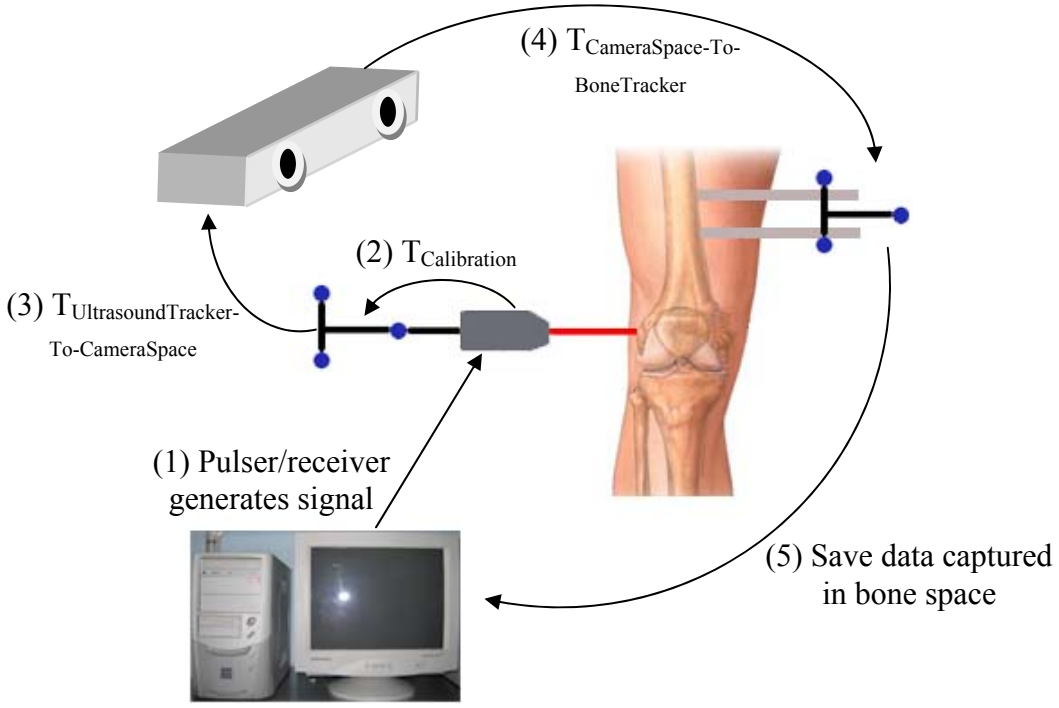


**Figure 4.1: Overview diagram of collecting A-mode ultrasound data on physical object. The physical data captured here is then registered to a CT-based virtual model. A computer and pulser/receiver generate a pulse to capture an ultrasound signal (1). The processed signal is converted from the coordinate space of the ultrasound transducer into the space of the ultrasound tracker using a pre-determined calibration (2). The resulting point in ultrasound tracker space is then transformed into camera space (3). That coordinate is then transformed (4) into the space of the bone tracker inserted into the physical bone. The data points in the coordinate space of the bone tracker are stored on the computer (5) and registered to a virtual surface model of the same bone.**

## 4.1 Hardware

An ultrasound system was implemented with the intention of being compatible with MAKO Surgical Corp.'s Voyager navigation system. An Olympus Panametrics-NDT ultrasound A-mode immersion transducer was purchased (model V312 0.25 inch element diameter). The transducer specification claimed 10MHz frequency (9 MHz in practice), and it is spherically focused with a focal length of 25mm. This is ideal for measuring bones that are relatively shallow in the tissue, like the tibia and distal femur.

For measuring bone that is beneath thicker tissue, a transducer with lower frequency and greater focal length would have been necessary. A tracker was affixed to the transducer so it could be seen and tracked by the camera (Fig. 4.2).

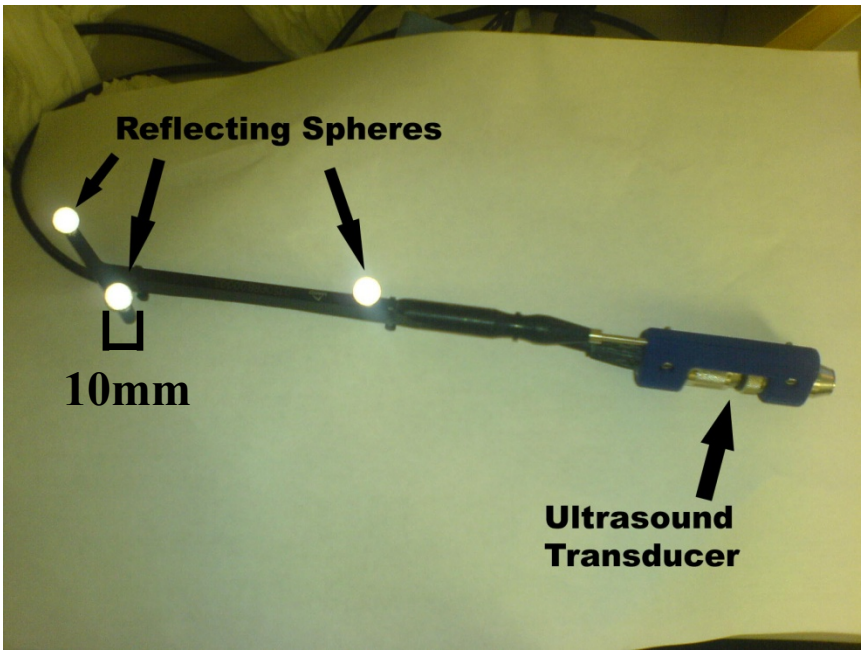


**Figure 4.2: Tracked ultrasound construct showing reflective spheres and ultrasound transducer fixed to the tracker. Each tracking sphere is 10 mm diameter.**

Various standoff solutions were employed. An Aquaflex gel pad, a water-filled glove finger, and a no-standoff option were all used. The Aquaflex pad is a medical grade bacteriostatic gel pad that is commonly used in clinical practice. The water-filled glove finger is created by simply cutting off a finger from a glove, filling it with water and tying it off. All approaches require the use of additional gel to allow for better signal propagation between each surface.

The transducer was controlled with an Olympus Panametrics-NDT pulser-receiver model 5072PR. It provided the electric pulse that the transducer would convert into sound energy, and it also received the resulting signal and passed it along to the PC. The

pulse repetition frequency was set to 100 Hz. The gain was set to 40dB. The resistance on the pulser-receiver was set to 50 Ohms. Both high-pass filtering and low-pass filtering were disabled as all signal processing was to be done in software. The mode was set such that the same transducer would both send and receive the signal.

The PC used was standard for the Voyager navigation system, but a capture card (AlazarTech ATS850) had to be installed. It was an 8-bit 50MHz card, which provides enough temporal and spatial resolution. The pulse repetition frequency was 100Hz so the 50MHz sampling rate of the card provided more than enough resolution. 8-bit resolution for reading a signal was enough to distinguish various peaks in the signal. The capture card also required an SDK (ATS-SDK ver. 4.6.1) to control it from software.

The particular hardware that is selected for this experiment affects the calculation in Equation 3.2. The AlazarTech capture card captures at a rate of 50 MHz. The results are captured as a record of data 4096 bytes long. Each byte represents an intensity value and its index is a chronological sample. The samples are converted to time and then Equation 3.2 is used to determine a distance. The equation to convert from sample index to distance using the specimen speed of sound constant of 1.54 mm/ s is shown in Equation 4.1:

$$d\,(mm) = sample\ index * \frac{1\,(sec)}{50 * 10^6 (samples)} * \frac{1.54(mm)}{1\,(\mu s)} * \frac{10^6\,\mu s}{1\,(sec)} * \frac{1}{2}$$

(Eq. 4.1)

## 4.2 Calibration

Calibration is necessary in order to determine the transformation from the ultrasound beam source to the tracker that is attached to the transducer. The ultrasound probe was precisely created so that the beam axis was aligned with the long axis of the tracker. This was accomplished with the assumption that the long axis of the housing of the transducer indicates the axis of the beam. This means that the only part of the transformation that needed to be determined was the three dimensional vector that indicates the translational offset from the tracker origin to the ultrasound beam origin (Fig 4.3).

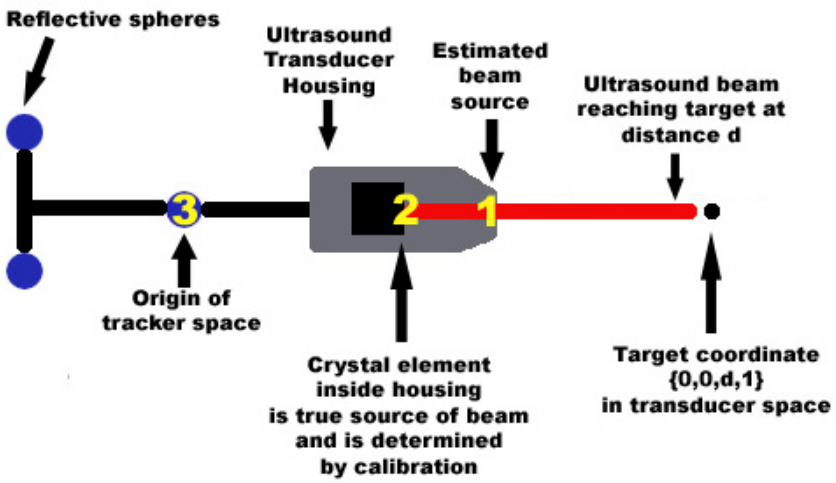


**Figure 4.3: Ultrasound transducer calibration diagram. Calibration finds the translational offset from the beam origin at 2 to the tracker origin at 3. The initial guess as measured by Coordinate Measurement Machine (CMM) is at 1, the front face of the transducer housing.**

### 4.2.1 Establishing Calibration Phantom

A metal sphere with radius r (25.4 mm) was used as a calibration phantom. The phantom did not have a tracker on it, so the phantom and camera had to remain stationary during the calibration. The calibration phantom was placed in a water bath so signal

propagation from the ultrasound transducer to the phantom would be clean. An acustar probe (Fig. 4.4) is used to gather points on the sphere surface and determine the center of the sphere in camera space. The center is calculated by fitting the acustar data points to a sphere and is represented in camera space as $(x_c,y_c,z_c,1)$.

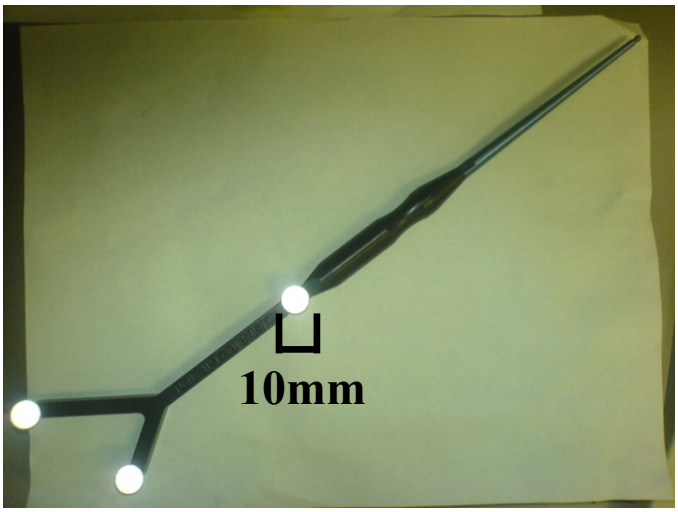


**Figure 4.4: Tracked acustar probe with spherical tip used to determine the calibration sphere center. The probe collects points around a spherical phantom and performs a sphere-fitting calculation on the data using the known radius of the phantom. The result determines a center coordinate $(x_c,y_c,z_c,1)$ that is used as a reference for the ultrasound calibration.**

### 4.2.2 Calibration Signal Processing

The signal processing that determines the distance along the beam is relatively simple (Fig. 4.5). A processing window is established that covers the expected distance to the surface of the sphere. Any noise that occurs outside that window is ignored. This eliminates artifacts from ring-down noise and echoes. This also requires that the user collect data by holding the transducer a proper distance away from the calibration phantom surface. Within that window, the signal is processed with a simple threshold filter. The maximum intensity within the processing window is labeled the peak of the signal as long as it is greater than a threshold. The detected peak is highlighted in the

display as the red-yellow interface (Fig. 4.6). The distance to the target is calculated using the time-of-flight from the source to the peak and Equation 3.2, where the speed of sound in water is 1450m/s.


**Figure 4.5: Processing scheme for calibration signals. The sinusoid shows a sample input that is passed through two filters. A processing window establishes a minimum and maximum distance in between which the peak is expected. If the peak occurs outside this window, it will not be detected. This implies that the transducer should be held an appropriate distance from the surface of the phantom. The signal is then passed through a peak detection filter that looks for intensities above a certain threshold.**

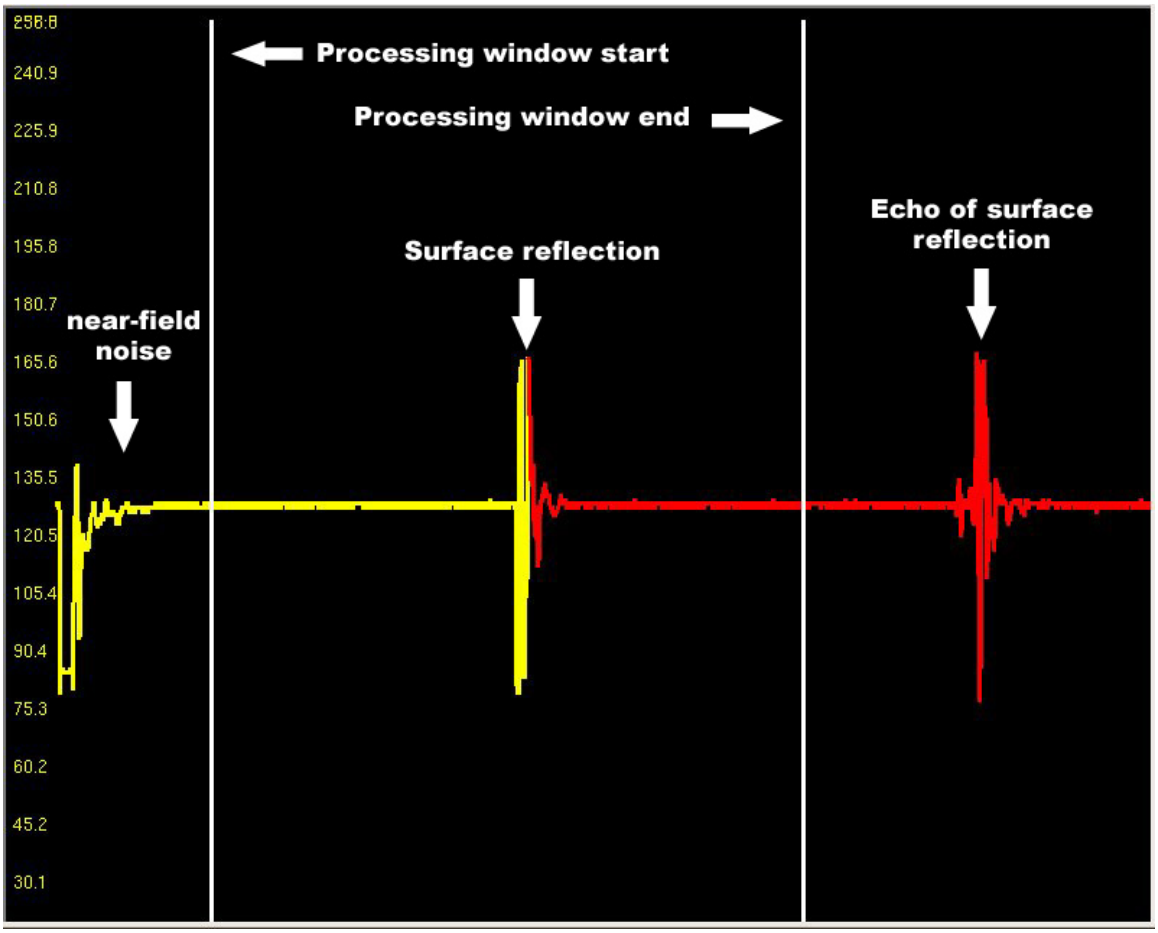


**Figure 4.6: Ultrasound calibration pulse filtered for a single reflection peak. The ring-down noise early in the signal is ignored by setting the start of the processing window to after the ring-down is complete. The surface reflection from the phantom surface provides a clear and strong signal that is indicated by the processing software as a change in color from red to yellow. An echo is created in the signal as the sound beam bounces off the face of the transducer, reflects off the phantom again, and returns to the transducer as a second peak. This second peak appears as a second surface farther away. By limiting the processing window to end before any expected echoes, the echo does not affect the determination of the phantom surface.**

### 4.2.3 Calculating Calibration

The tracked ultrasound transducer is used to collect data points on the surface of the sphere. Signal processing can determine the distance of the "touched" surface, d, from the beam source. The beam is defined to be along the z-axis, so the point in ultrasound beam space is (0,0,d,1). That point is converted to the space of the tracker with the calibration transform, $T_{UltrasoundBeamToTracker}$. When a data point is captured, the

camera also captures a transform representing the location of the tracked spheres in camera space, $T_{Tracker\text{-}to\text{-}Camera}$. The final coordinate P in camera space is given by the equation in Equation 4.2.

$$P_{CameraSpace} = T_{Tracker-To-Camera} * T_{UltrasoundBeam-To-Tracker} * (0,0,d,1)^T$$

(Eq. 4.2)

An optimization routine uses a set of points (0,0,d,1) paired with a set of transforms $T_{Tracker\text{-}to\text{-}Camera}$. The initial guess for the transform $T_{UltrasoundBeamToTracker}$ is provided by a CMM (Coordinate Measurement Machine) measurement of the center of the front face of the transducer. The algorithm, shown later in pseudocode, then calculates the objective function by transforming the point from ultrasound beam space to camera space using that series of transforms and determining the point's distance from the previously determined sphere center $(x_c,y_c,z_c,1)$. The error for the objective function is the difference between that distance and the known radius r (Equation 4.3) (Fig. 4.7).

```
Set initial transform guess to CMM value
For each point in calibration data set
        Initial Error += error based on objective function
        Current Error = Initial Error
While (error > MaxErrorThreshold && iteration < MaxIterations)
        For each of three parameters (one for each dimension of translation)
                Parameter += delta
                For each point in calibration data set
                        Intermediate Error += error based on objective function
                Parameter -= delta
        Adjust all parameters based on Intermediate Errors
        For each point in calibration data set
                Resulting Error += error based on objective function
        If (Resulting Error < Current Error)
                Save adjusted parameter values and iterate
        Else
                Reset parameter values and iterate
```

$$Error = | r - Distance\left((x_c, y_c, z_c, 1), P_{CameraSpace}\right)| \quad \text{(Eq. 4.3)}$$

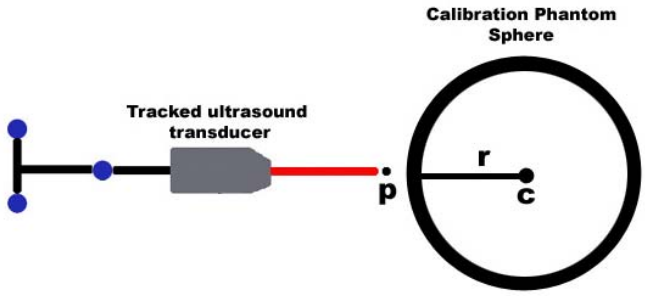


**Figure 4.7: Diagram showing calibration objective measurement. The calibration is used to transform the point p into the reference space of the camera (the same space as sphere center c). The error for each point captured is calculated as the difference between the distance from p to the center c and the known radius r. In the form of Equation 4.2, Error =abs( r – (distance(p,c)))**

The optimization is performed using an implementation of the Levenberg-Marquardt algorithm with a 3-parameter vector as the desired solution set indicating the

translational offset. The results of the calibration include a root-mean-square error (RMS) and a condition number, which indicates the quality of the data set. The ultrasound data points are then displayed on the sphere using the resulting calibration transform. The Levenberg-Marquardt implementation is verified using a computer generated data set that precisely matches the shape of the phantom.

## 4.3 Ultrasound Registration

The registration is calculated using MAKO Surgical Corp.'s surface matching algorithm, which is a variant of ICP [9]. The registration matches an image space model to a physical model. The image space model is generated by segmenting a CT scan. The registration routine requires that a point-pair matching first be attained by collecting anatomical landmarks in image space and on the physical model. This provides an initial guess for the registration solution. In the image space, the hip center is captured as the center of the femoral head. The medial and lateral epicondyles are captured on the femur. The medial and lateral malleoli are captured on the ankle. Then, in physical space, those same landmarks except for hip center are captured with the tracked mechanical probe. Capturing several poses while rotating the femur and calculating the center of rotation determines the hip center. Then, approximately 50 points for each of the tibia and femur are collected and fed into the ICP algorithm.

### 4.3.1 CT Scan Protocol

Each CT scan was taken as three image groups in the same series. The first group was taken centered at the hip (center of the femoral head) with a 10cm length and 5mm

slice intervals along the axial direction. The second group was centered about the knee and had a length of 10cm proximal and 10cm distal of the joint with 1mm slice intervals. The third group was centered about the ankle with a length of 10cm and 5mm slice intervals. All groups had a 25mm field-of-view with intraslice resolution of 0.48mm x 0.48mm. The scan was performed with a helical scan and bone reconstruction algorithm. To create a computer model from the CT scan DICOM images, a segmentation was created from 40 sagittal slices for each bone. A contour was drawn in each slice to outline the bone in the DICOM image. Once all slices had been contoured, the contours were automatically triangulated to form a three-dimensional model.

The length of the knee volume portion of the CT scan was varied with the cadaver specimens. Taking advantage of the benefits of ultrasound, a longer scan allows for more area to be "reached" by the tracked ultrasound probe. Unlike a standard mechanical probe that must physically reach the bone through the incision, the ultrasound probe has the ability to transcutaneously collect data even if the bone cannot be directly touched through the incision. Therefore, the first specimen deviates from the typical protocol by having an extra-long preoperative scan which is then segmented to generate the image space model. Due to problems discussed in the results section, the second and third specimens returned to more normal length CT scans. The effects of the different scan lengths on the registrations are compared.

### 4.3.2 Accessibility

Another consideration is which part of the bone should be accessible. While the sawbones are completely exposed, real specimens will be limited in which parts of the

bone can be reached by the ultrasound. Both the ultrasound probe and the mechanical probe will have limitations in accessibility (Fig. 4.8). The sawbone point collection was therefore limited to match realistic clinical situations.

While some studies analyze accessibility for total knee replacement (TKR) procedures [70], few analyze the difficulties inherent with a unicondylar knee replacement (UKR) procedure. MAKO Surgical Corp. has determined a mechanical probe registration pattern based on dozens of UKR procedures. For the mechanical probe approach, only the medial condyle of the femur and the medial tibia near the incision are accessible. For the ultrasound approach, the areas on the side and anterior of the bones are accessible, but in between the joint is unavailable because there is no incision and the patella is in the way. Additionally, the posterior of the leg contains significantly more tissue of varying density that will cause a noisy ultrasound signal.

**(a)**

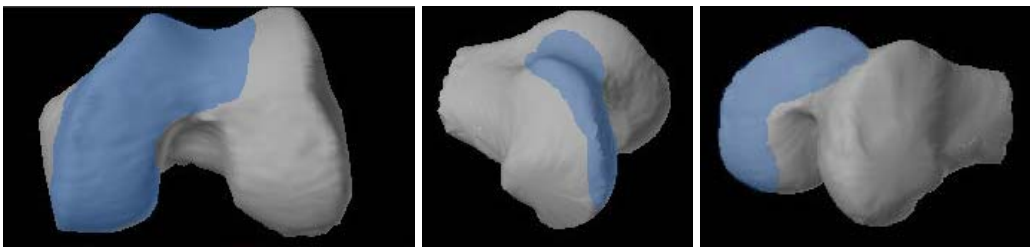

**(b)**

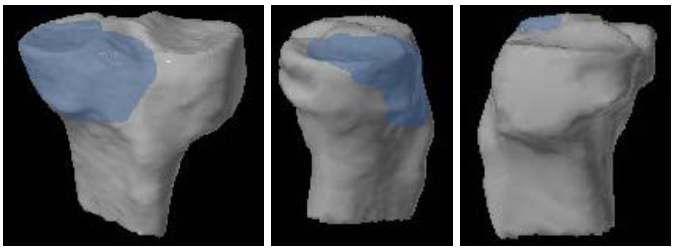

**(c)**

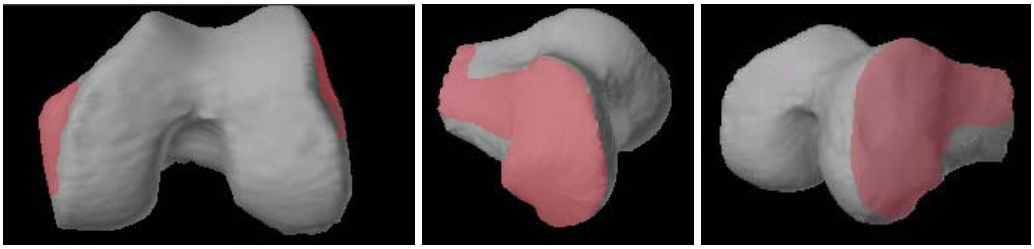

**(d)**

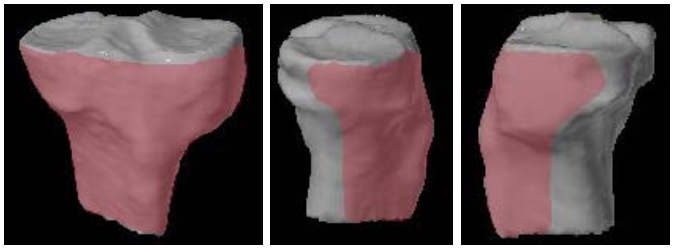

**Figure 4.8: (a) Accessible areas on femur for mechanical probe. (b) Accessible areas on tibia for mechanical probe. (c) Accessible areas on femur for ultrasound. (d) Accessible areas on tibia for ultrasound. The primary constraint for the mechanical probe approach is the incision. If an area can be reached through the incision, a sharp or blunt tipped probe can touch the bone even if cartilage exists. Ultrasound has different constraints since the beam can reach the bone transcutaneously. The incision is no longer relevant for an ultrasound approach. For femur data collection, the patella can obscure ultrasound access. For the tibia, reaching the plateau is difficult since that is where the femur and tibia meet.**

### 4.3.3 Phantom Registration

Once a calibration is established, the tracked transducer is used to collect data points on plastic models of a femur and tibia to register it to a segmented CT of the same models. Sawbone phantom femurs and tibias (Pacific Research Labs, Inc. part 1145-1, Vashon, Washington) are used for phantoms. For ultrasound point collection on a phantom, the phantom is placed in a water bath so the ultrasound signal can be easily conducted from the immersion transducer to the phantom. The ultrasound approach for the phantom is compared to a tracked mechanical probe approach where the points are collected with a tracked mechanical probe.

There are several considerations when capturing the data points with the tracked ultrasound transducer on the sawbone. First, the signal must be processed in software to better filter out noise and find the peaks, which indicate relevant distances. For the application to automatically and continuously collect data points, the software must determine which signals are valid. The signal from a sawbone is similar to the one in the calibration procedure. There is a single peak that determines the surface of the target. However, rather than use the processing scheme that was used in calibration, a more versatile processing algorithm was developed in order to prepare for a real specimen registration.

Several filters were developed to smooth the signal and apply a threshold to determine where the peaks are (Fig. 4.9). The first few hundred samples of each signal are zeroed-out by the filter because they are in the field of ring-down noise of the transducer. The demean filter finds the average value and removes it from each element

in the signal. Rectify signal takes the absolute value of the signal so the successive filters will only perform operations on non-negative values. The low-pass filter smoothes out the signal so contiguous peaks and valleys can be easily detected. The threshold filter analyzes the smoothed result and determines how many significant peaks exist.


**Figure 4.9: Bone intra-signal processing flowchart. A sinusoid is shown as a sample input signal to the series of filters that ultimately find a peak from a bone reflection. The demean filter finds the average value and removes it from each element in the signal. Rectify signal takes the absolute value of the signal so the successive filters will only perform operations on non-negative values. The low-pass filter smooths out the signal so contiguous peaks and valleys can be easily detected. The threshold filter analyzes the smoothed result and determines how many significant peaks exist.**

The experimental filter variations include differences in the cutoff frequency of the smoothing filter as well as the threshold value of the threshold filter. The best one is experimentally determined and used for all registrations. The smoothing filter eliminates problems caused by noise introduced by varying tissue densities and slightly off-axis signals. To get the most accurate results, the transducer should be normal to the target so that the reflected signal is maximized [5]. Any signals that deviate from the normal should be thrown out. The threshold filter achieves this by ignoring signals with peaks that are not significant. The threshold filter is simply adjusted for sawbones by looking for signals with exactly one peak (Fig. 4.10). Its use for real specimens will be discussed later.

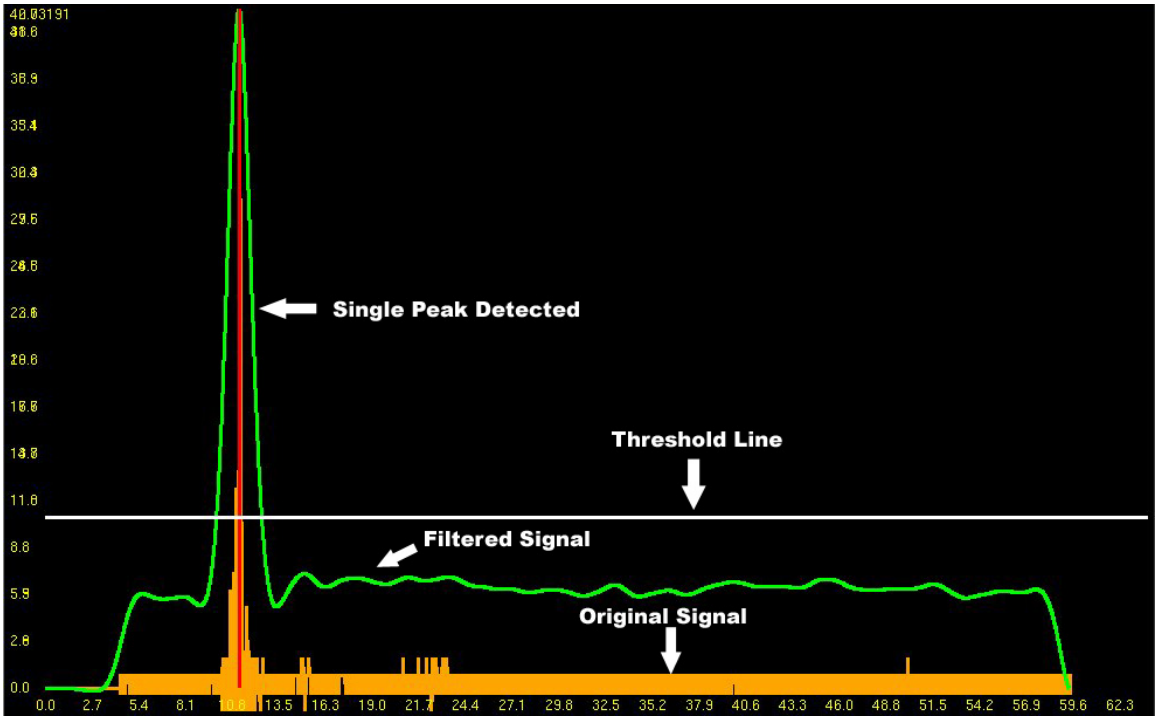


**Figure 4.10: A single peak easily detected on the surface of the sawbone phantom. The signal is filtered using the scheme in Figure 4.10. The orange line indicates the signal after the demean filter. The green line shows the signal after the demeaned signal has been rectified and low-pass filtered. The red vertical line indicates that the software found a peak, which is the highest point in a contiguous region above the white horizontal threshold line. Several of these signals are then filtered with a spatial and temporal inter-filter scheme to yield a valid surface detection.**

An additional indication of a noisy or inaccurate signal is inconsistency. A signal that is not consistently yielding a coordinate to within a certain threshold when the transducer is not moving is a sign of a poor data point. An additional inter-signal temporal filter is added to ensure that the signal is consistent. It requires that the transducer capture several data points successively in the same position to determine that the point is genuinely on the bone and is not generated by noise. After each signal is processed using the scheme in Figure 4.9, the resulting data point is passed through this temporal filter to determine consistency. The temporal filter has parameters for length of history and a threshold from previous points. The history length determines how many signals must successively yield the same result in order for the current signal to be

considered valid. The threshold determines how similar the current signal must be from its past signals in order to be considered the same point.

When collecting points with the transducer, a spread is necessary so not all points are clustered in the same exact position. In addition to outlining a pattern of regions that should be covered, the software uses an inter-signal spatial filter to cull out neighboring points that are too close together. The filter requires a minimum spread of 1mm between each data point. This filter ensures that the data collection is not limited to any one feature on the anatomy and improves the odds that a registration will be accurate. A poor spread of data could yield a misleadingly low RMS error value even though the registration is inaccurate.

### 4.3.4 Specimen Registration

The general registration scheme for the specimens is the same as for the phantoms. The specimen ultrasound registration is compared to a mechanical probe registration. In addition to having limitations to accessibility, the mechanical probe approach for the specimens must deal with bone that is covered with cartilage as well as bone that is directly exposed. This requires two separate probes, one sharp for penetrating cartilage and one blunt for touching bone surfaces that have no cartilage. The ultrasound transducer avoids this problem since the beam penetrates directly to the bone.

The standoff is a critical component for the specimen registration. While it does not play a role in the calibration or phantom registrations, it becomes necessary for capturing clean signals on a real specimen. Since there is no water bath for the real specimens, the transducer must be placed directly on the specimens. The signal will not

cleanly show the bone surface if the surface is too close to the source of the transducer beam. The standoff provides the necessary buffer so the target is placed farther away from the source, ideally without adding any air gaps that would prevent the ultrasound signal from propagating. However, a standoff may create problems since the transducer must have a perfect coupling to the target. Gel facilitates this coupling, but any extra components can increase the chance that there will be an air gap between the transducer and its target thereby blocking the ultrasound beam. The three standoff options were using none at all, using an AquaFlex gel pad, and using a glove finger filled with water.

Specimen registration is performed using a similar processing algorithm to the one used on sawbones. The only difference is that the algorithm searches for exactly two peaks instead of one (Fig. 4.11). The first peak indicates the interface between the standoff and the skin surface. The second peak is the boundary between the tissue and the bone. Since the bone is the target, the distance indicated by the second peak is calculated.

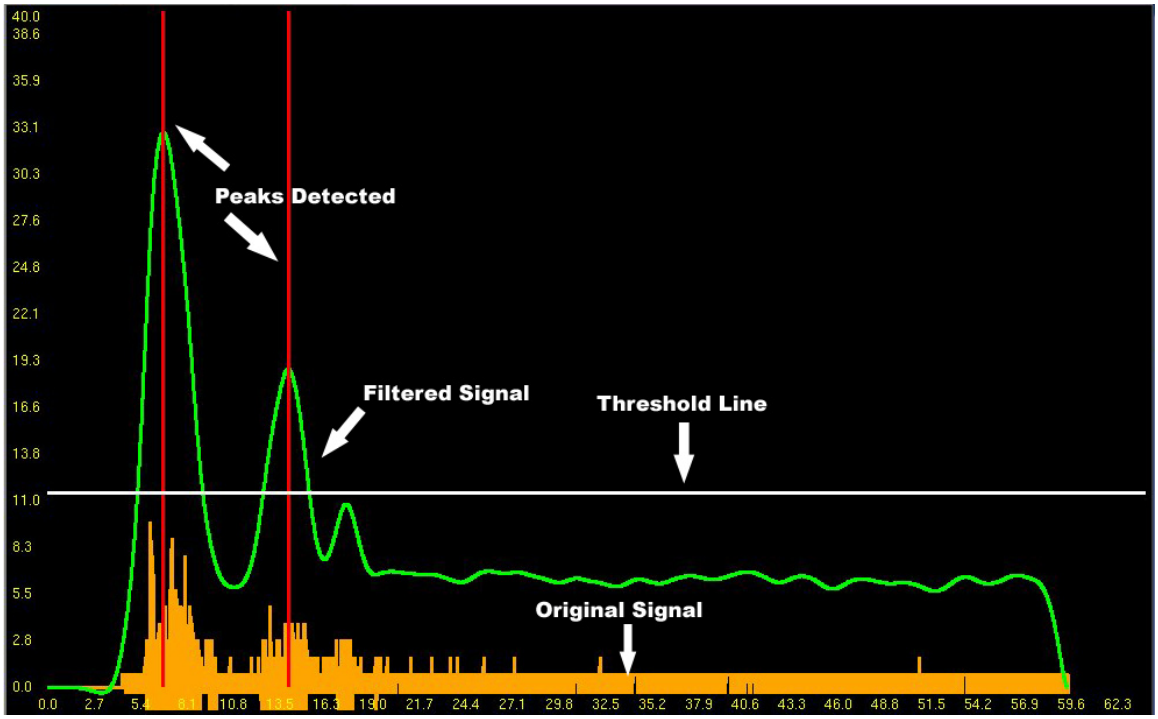


**Figure 4.11: The characteristic double peaks that indicate the standoff/skin boundary as well as the tissue/bone boundary. This differs from the single peaks that are typical of the calibration and phantom signals. The first peak in this example occurs at approximately 7 mm away and the second peak occurs at approximately 13 mm away. However, since tissue is thicker in some areas of the anatomy, a processing window cannot be established for this signal as it was with the calibration signals.**

### 4.3.5 Criteria for Results

An RMS error is determined for the data points by measuring the distance of each captured point from the computer model bone surface after the resulting registration transform was applied to each point. This is similar to the TRE (Target Registration Error) that Fitzpatrick et al describe [24] since many of the points captured are close to the area of concern. This provides a decent indication for success, but a low RMS error does not necessarily imply that the registration was successful. A poorly spread data set may yield a low RMS value as all the points can rest perfectly on the bone surface in image space, but the solution may be a local optimum and still be significantly different

than the globally optimal solution. The following equation shows how the RMS is calculated:

$$RMS^2 = \frac{1}{N} * \sum distance(x,y)^2 \qquad \text{(Eq. 4.4)}$$

where x is the data point as transformed into image space using the resulting registration, and y is the point on the image space surface model closest to point x.

For a more robust measure of the merit of a registration, a comparison to a ground truth registration is necessary. The mechanical probe approach used by MAKO Surgical Corp. has been verified as an accurate approach to registration. The ultrasound approach for the phantom is compared to a tracked mechanical probe approach. The only difference between the approaches is the device and method used for capturing points on the bone. The segmentation, initial registration, and registration algorithm are the same. The registration with a mechanical probe results in the same type of transform as that of the ultrasound registration, specifically a Bone-Tracker-To-CT-Space transform ($T_{BoneTracker\text{-}To\text{-}CTSpace}$). The process of inverting the transform from the mechanical probe result and applying it to the transform of the ultrasound result yields an error metric (Equation 4.5). The metric is an error matrix based in CT space with a clinically relevant coordinate system. The x axis is aligned with the medial-lateral axis, the y axis is aligned with the anterior-posterior axis, and the z axis is aligned with the superior-inferior axis (also known as the mechanical axis). If the transforms do not differ, implying that the ultrasound registration is ideal, then the error matrix would be the identity matrix. The resulting matrix is then decomposed into translation and rotation errors for each axis.

$$T_{Error\ Matrix} = \left(T_{BoneTracker-To-CTSpace-From\ Mechanical}\right)^{-1} * \left(T_{BoneTracker-To-CTSpace-From\ Ultrasound}\right)$$

(Eq. 4.5)

Thresholds for how much error is clinically acceptable are subjective and dependent on the surgeon and the procedure. Maurer et al stated that an upper limit of 3mm for a target registration error (TRE) in vivo could be achieved, determined by the distance between each target point transformed from its gold standard transform and the target point transformed from the transform being evaluated [50]. The criteria that MAKO Surgical Corp. uses for a clinically relevant threshold for registration is 2 mm translational error in any axis and 2 degree rotational error about any axis relative to a fiducial-based registration.

In addition to the quantitative measures, displaying the ultrasound data points using the ground truth registration transform can expose which data points are improperly collected. This shows which areas may be less accessible for clean propagation of the ultrasound signal. It can also expose any errors in the signal processing or calibration by indicating a shift in the captured data points relative to the bone image surface. This view can be achieved by applying the ground truth registration transform as captured by the mechanical probe to the ultrasound data points captured in tracker space as in Equation 4.6.

$$P_{Ultrasound\ Ground\ Truth} = T_{BoneTracker-To-CTSpace-From\ Mechanical} * T_{UltrasoundBeam-To-Tracker} * (0,0,d,1)^T$$

(Eq. 4.6)

## Chapter 5: Results

### 5.1 Calibration

Five calibrations were collected. The optimization determined the translational offset from the tracker source to the beam source. For each calibration, an RMS error and condition number were calculated. The RMS is the root mean square of the error for each data point as measured from the surface of the sphere using the final transformation. The condition number is the measure of the quality of the data set. A greater spread of data will lead to a lower condition number. Table 5.2 shows the resulting calibration transforms for each of the calibrations. Table 5.2 shows the error results of each calibration. The mean RMS error across all calibrations was 0.69 mm and the mean condition number was 9.67. Each calibration result is displayed virtually with the calibration points mapped to the surface of the phantom and colored according to the distance from the surface (Figs. 5.1-5.5).

**Table 5.1 Resulting calibration translational offsets. Each calibration attempt yields a translational offset from the origin of the beam to the origin of the ultrasound tracker. These are the resulting offsets in tracker space.**

| | X-axis Translational Offset | Y-axis Translational Offset | Z-axis Translational Offset |
|---|---|---|---|
| **Calibration 1** | 28.10 | 1.72 | 201.47 |
| **Calibration 2** | 26.00 | 0.92 | 201.22 |
| **Calibration 3** | 25.42 | 1.31 | 201.34 |
| **Calibration 4** | 28.50 | 0.60 | 201.44 |
| **Calibration 5** | 23.14 | 1.53 | 201.33 |

**Table 5.2 Calibration error results. Each calibration is measured by an RMS calculated from all of the sample points. The Levenberg-Marquardt optimization routine also provides a condition number to measure the quality of the spread of the data points. A better calibration is indicated by a lower RMS and a lower condition number.**

| | RMS (mm) | Condition Number |
|---|---|---|
| **Calibration 1** | 0.55 | 6.79 |
| **Calibration 2** | 0.91 | 6.19 |
| **Calibration 3** | 0.71 | 10.70 |
| **Calibration 4** | 0.66 | 10.45 |
| **Calibration 5** | 0.60 | 14.20 |
| **Overall Mean** | 0.69 | 9.67 |

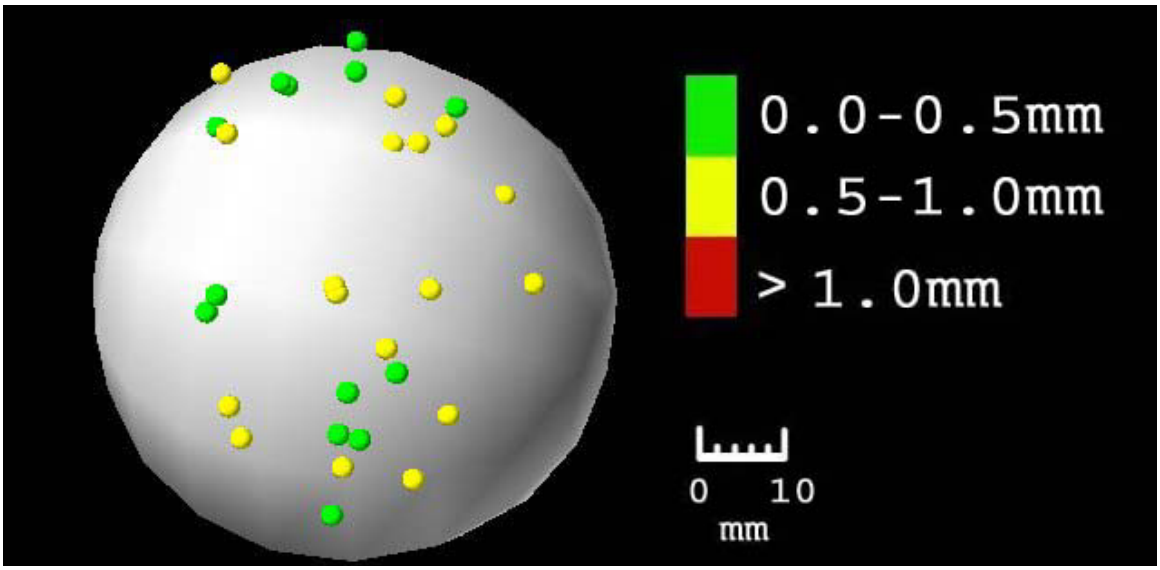


**Figure 5.1 The first calibration result has an RMS of 0.55 mm and a condition number of 6.79. It is displayed virtually with the spherical phantom. Each sample point is shown colored according to its distance from the surface of the sphere. Green points are less than 0.5 mm away, yellow points are between 0.5 and 1.0 mm away, and the red points are more than 1.0 mm away from the sphere surface. Each sample point is displayed with a 1.0 mm radius.**

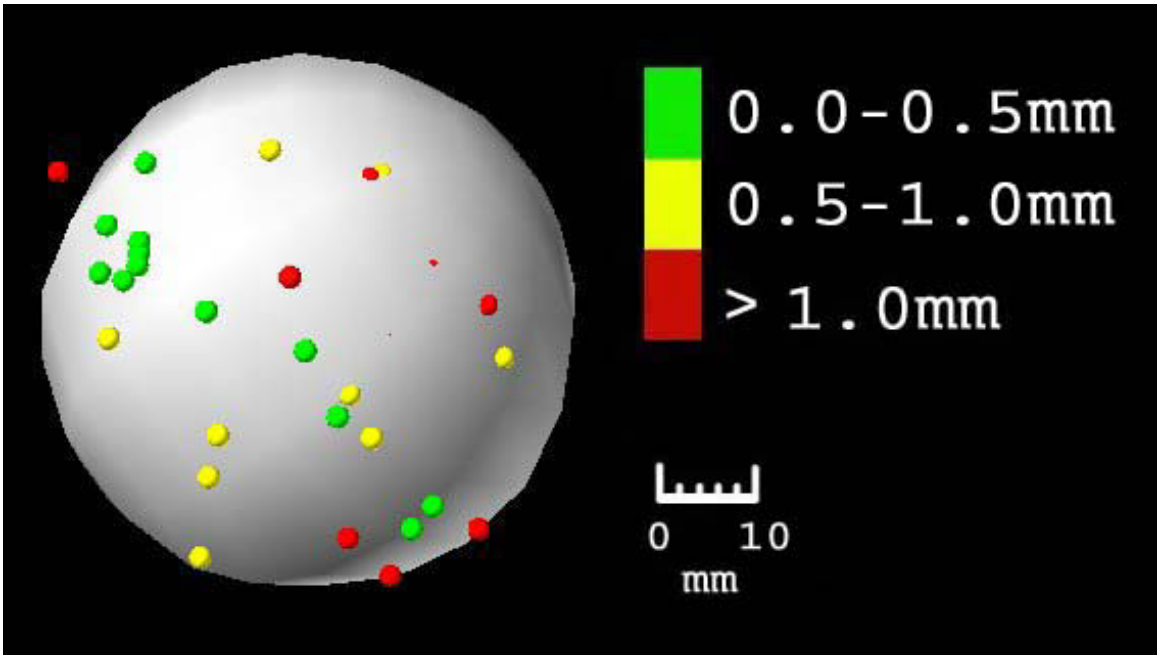


**Figure 5.2 The second calibration result has an RMS of 0.91 mm and a condition number of 6.19. It is displayed virtually with the spherical phantom. Each sample point is shown colored according to its distance from the surface of the sphere. Green points are less than 0.5 mm away, yellow points are between 0.5 and 1.0 mm away, and the red points are more than 1.0 mm away from the sphere surface. Each sample point is displayed with a 1.0 mm radius.**

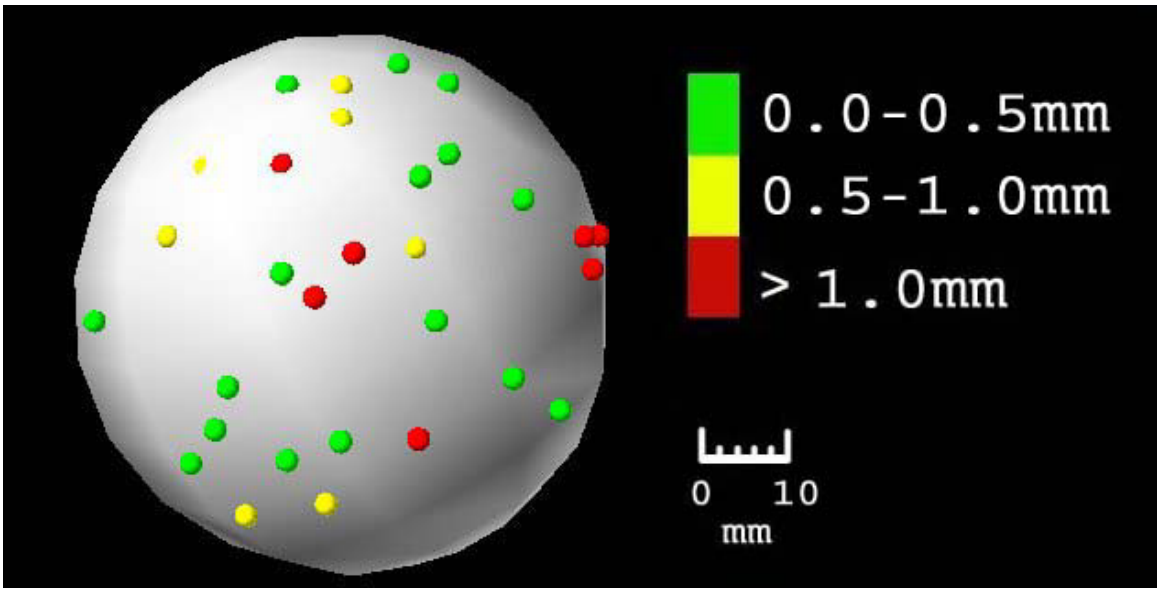


**Figure 5.3 The third calibration result has an RMS of 0.71 mm and a condition number of 10.70. It is displayed virtually with the spherical phantom. Each sample point is shown colored according to its distance from the surface of the sphere. Green points are less than 0.5 mm away, yellow points are between 0.5 and 1.0 mm away, and the red points are more than 1.0 mm away from the sphere surface. Each sample point is displayed with a 1.0 mm radius.**

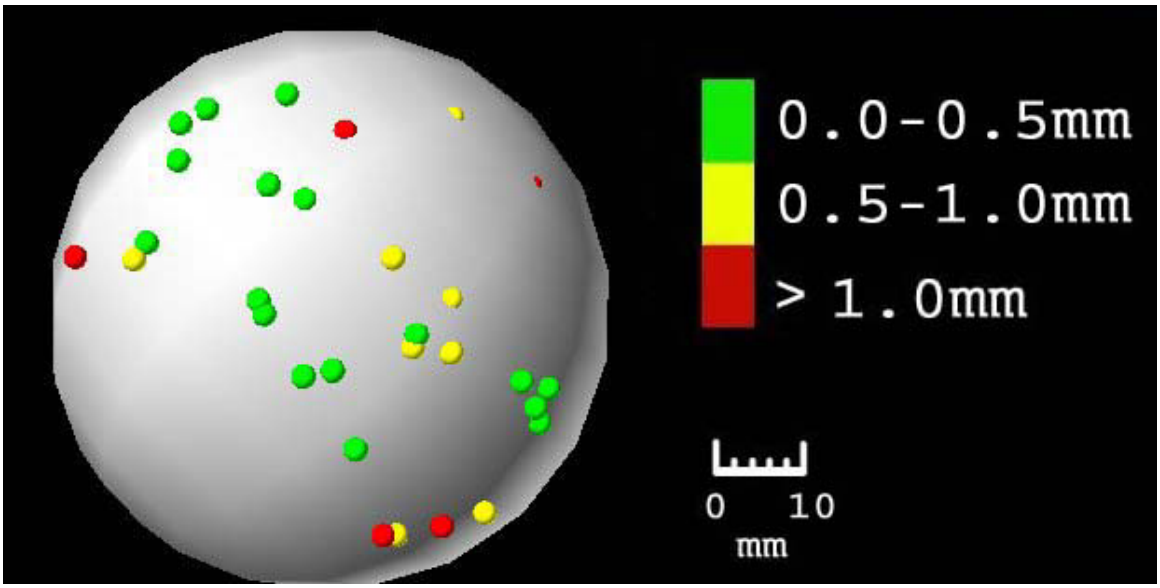


**Figure 5.4 The fourth calibration result has an RMS of 0.66 mm and a condition number of 10.45. It is displayed virtually with the spherical phantom. Each sample point is shown colored according to its distance from the surface of the sphere. Green points are less than 0.5 mm away, yellow points are between 0.5 and 1.0 mm away, and the red points are more than 1.0 mm away from the sphere surface. Each sample point is displayed with a 1.0 mm radius.**

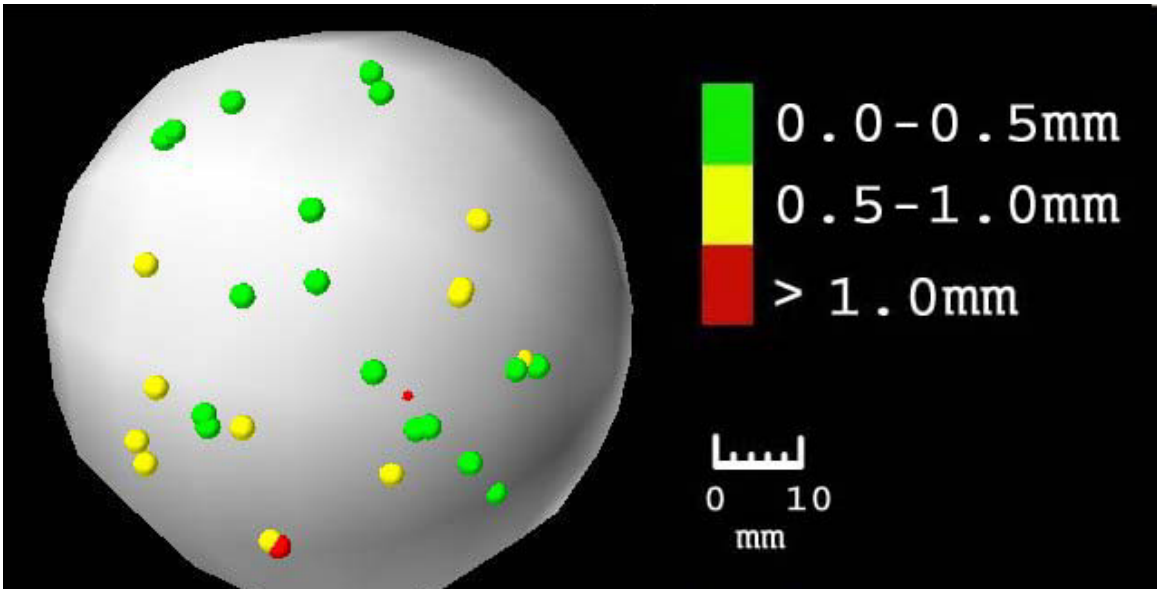


**Figure 5.5 The fifth calibration result has an RMS of 0.60 mm and a condition number of 14.20. It is displayed virtually with the spherical phantom. Each sample point is shown colored according to its distance from the surface of the sphere. Green points are less than 0.5 mm away, yellow points are between 0.5 and 1.0 mm away, and the red points are more than 1.0 mm away from the sphere surface. Each sample point is displayed with a 1.0 mm radius.**

## 5.2 Phantom Registration

### 5.2.1 First Phantom Registration

Five registrations for the tibia and femur were captured with the A-mode ultrasound scheme. An RMS error was determined for the data points by measuring the distance of each captured point from the computer model bone surface after the resulting registration transform was applied to each point. The average RMS error for the tibia registrations was 1.06mm. The average RMS error for the femur registrations was 1.19mm.

In addition, the ultrasound approach for the phantom is compared to a standard tracked mechanical probe approach. The only difference between the approaches is the device and method used for capturing points on the bone. The segmentation, initial registration, and registration algorithm are the same. The registration with a mechanical probe provides the same type of transform as that of the ultrasound registration, specifically a Bone-Tracker-To-CT-Space transformation ($T_{BoneTracker\text{-}To\text{-}CTSpace}$). Inverting the transform from the mechanical result and applying it to the transform of the ultrasound result yields an error metric. If the transforms do not differ, implying that the ultrasound registration is ideal, then the error would be the identity matrix. The resulting matrix is decomposed into translation and rotation errors for each axis. The errors for each registration as well as the mean errors are displayed in Table 5.3.

**Table 5.3: Registration results for phantom #1 compared to standard registration with mechanical probe. The error is derived from a decomposed matrix that applies the inverse of the standard registration result with the ultrasound registration results. The table is broken down into errors for a) translation for femur, b) rotation for femur, c) translation for tibia, and d) rotation for tibia for each axis.**

**a)**

| Femur Phantom #1 | X translation error (Medial-Lateral) (mm) | Y translation error (Anterior-Posterior) (mm) | Z translation error (Superior-Inferior) (mm) |
|---|---|---|---|
| Registration #1 | 1.71 | 3.23 | 3.61 |
| Registration #2 | 2.13 | 3.81 | 1.66 |
| Registration #3 | 2.81 | 4.72 | 2.03 |
| Registration #4 | 3.80 | 5.02 | 0.27 |
| Registration #5 | 2.24 | 3.61 | 3.43 |
| Mean | 2.54 | 4.08 | 2.19 |

**b)**

| Femur Phantom #1 | Rotation about X-axis (Medial-Lateral) (degrees) | Rotation about Y-axis (Anterior-Posterior) (degrees) | Rotation about Z-axis (Superior-Inferior) (degrees) |
|---|---|---|---|
| Registration #1 | 0.42 | 0.03 | 0.45 |
| Registration #2 | 0.53 | 0.15 | 0.55 |
| Registration #3 | 0.32 | 0.09 | 4.76 |
| Registration #4 | 0.31 | 0.30 | 2.55 |
| Registration #5 | 0.58 | 0.05 | 0.95 |
| Mean | 0.43 | 0.12 | 1.85 |

**c)**

| Tibia Phantom #1 | X translation error (Medial-Lateral) (mm) | Y translation error (Anterior-Posterior) (mm) | Z translation error (Superior-Inferior) (mm) |
|---|---|---|---|
| Registration #1 | 0.84 | 1.49 | 2.46 |
| Registration #2 | 0.53 | 2.23 | 1.86 |
| Registration #3 | 0.37 | 1.74 | 2.50 |
| Registration #4 | 0.29 | 0.66 | 3.31 |
| Registration #5 | 0.95 | 0.58 | 4.13 |
| Mean | 1.07 | 2.17 | 2.43 |

**d)**

| Tibia Phantom #1 | Rotation about X-axis (Medial-Lateral) (degrees) | Rotation about Y-axis (Anterior-Posterior) (degrees) | Rotation about Z-axis (Superior-Inferior) (degrees) |
|---|---|---|---|
| Registration #1 | 0.76 | 0.77 | 0.43 |
| Registration #2 | 0.77 | 0.69 | 0.20 |
| Registration #3 | 0.13 | 1.14 | 1.37 |
| Registration #4 | 0.95 | 0.58 | 4.13 |
| Registration #5 | 0.51 | 0.49 | 0.80 |
| Mean | 0.62 | 0.73 | 1.38 |

The ultrasound data points were also displayed using the registration from the mechanical probe. This creates a visualization that shows which data points were accurately captured. Figures 5.6 and 5.7 show that the data points for the phantom registration seem to be floating off of the surface of the image model. Because the points are uniformly in error, an error in the speed of sound could account for the poorly aligned data points. The speed of sound constant was 1450 m/s. This constant is based on distilled water at a precisely controlled temperature. Since the environmental conditions may not have matched the theoretical conditions on which the constant is based, the constant may be an inappropriate value. Although the results relative to the mechanical probe registration are within a reasonable range, a second phantom registration data set is captured with a more precise constant for the speed of sound.

a)

b)

c)

d)

e)

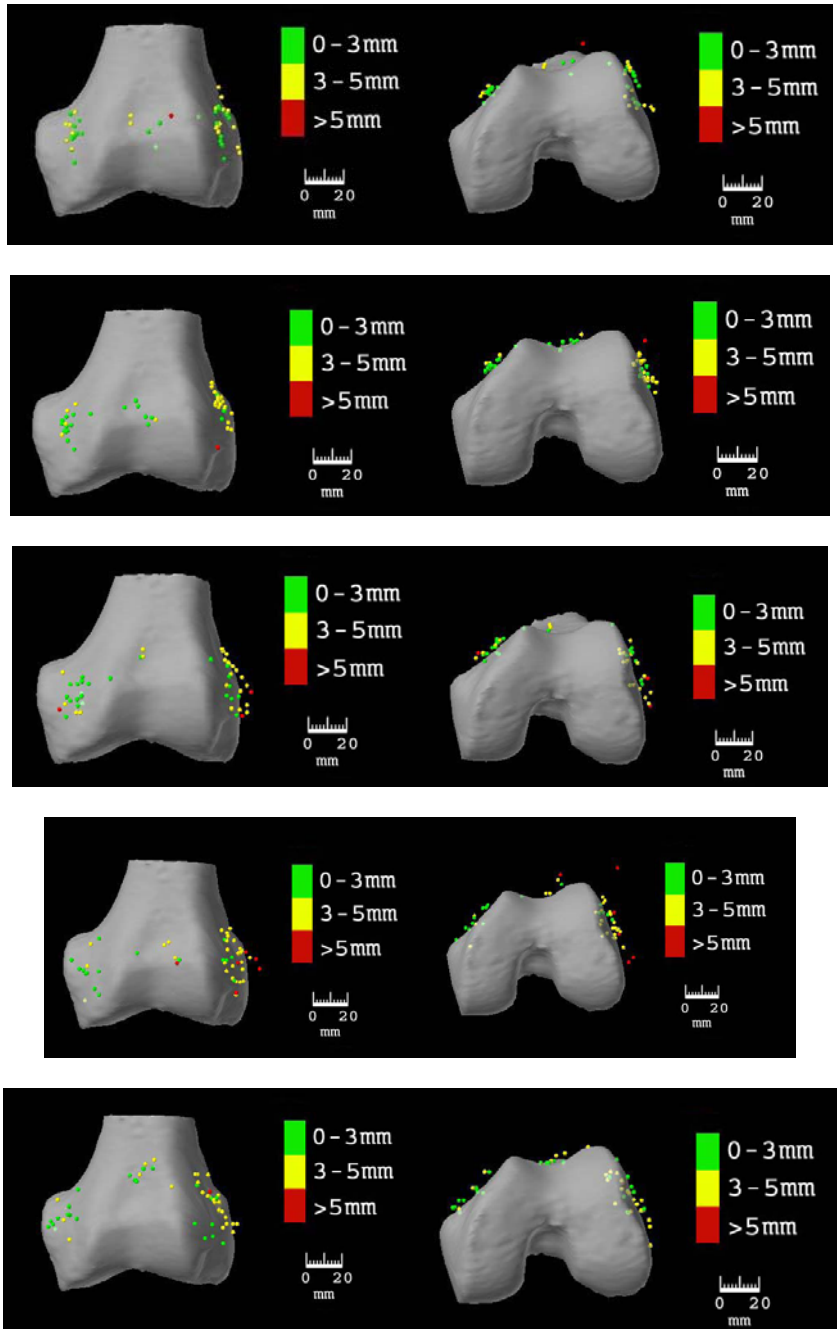


**Figure 5.6 Femur registrations for phantom #1. a) registration #1, b) registration #2, c) registration #3, d) registration #4, e) registration #5. The phantom femur segmented model is displayed with ultrasound data points from coronal and transverse perspectives. The points are transformed using the ground truth registration from the standard registration approach. The distance of the point from the model shows the quality of the ultrasound capture approach. Data points less than 3 mm away are shown in green, points that are between 3 and 5 mm away are shown in yellow, and points that are greater than 5 mm away are shown in red.**

a)

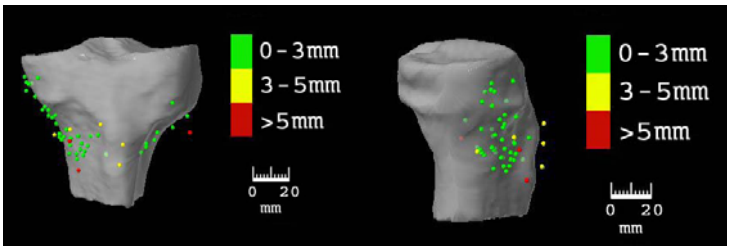


b)

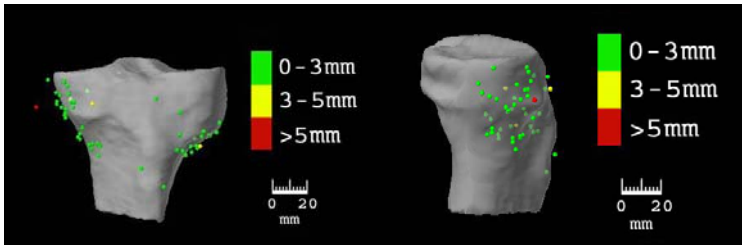


c)

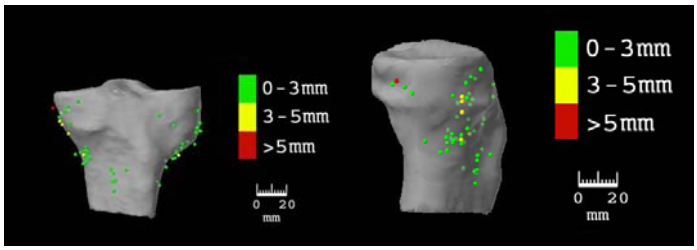


d)

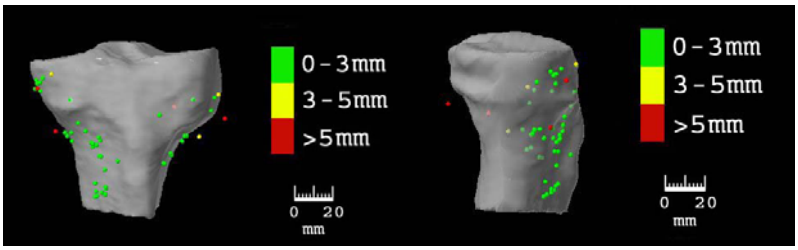


e)

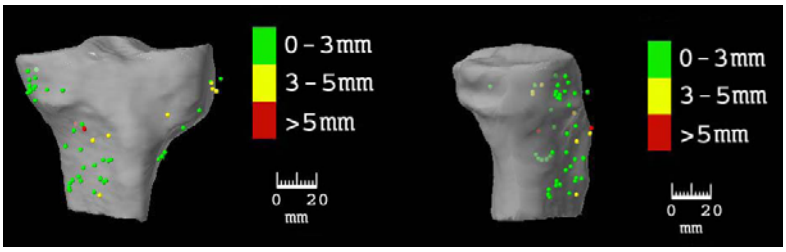


**Figure 5.7 Tibia registrations for phantom #1. a) registration #1, b) registration #2, c) registration #3, d) registration #4, e) registration #5. The phantom tibia segmented model is displayed with ultrasound data points from coronal and sagittal perspectives. The points are transformed using the ground truth registration from the standard registration approach. The distance of the point from the model shows the quality of the ultrasound capture approach. Data points less than 3 mm away are shown in green, points that are between 3 and 5 mm away are shown in yellow, and points that are greater than 5 mm away are shown in red.**

### 5.2.2 Second Phantom Registration

Experimental values for the speed of sound in water often use distilled water at a cooler temperature than was used for the first phantom experiment. As a result, the speed of sound was adjusted to 1540 m/s to match the current setup. Table 5.4 shows the results relative to the standard mechanical probe registration. Figures 5.8 and 5.9 shows the display of the ultrasound points transformed with the ground truth transform and shows a clear improvement over the first phantom registrations that used a speed of sound constant of 1450 m/s in water.

**Table 5.4: Registration results for phantom #2 compared to standard registration with mechanical probe. The error is derived from a decomposed matrix that applies the inverse of the standard registration result with the ultrasound registration results. The table is broken down into errors for a) translation for femur, b) rotation for femur, c) translation for tibia, and d) rotation for tibia for each axis.**

**a)**

| Femur Phantom #2 | X translation error (Medial-Lateral) (mm) | Y translation error (Anterior-Posterior) (mm) | Z translation error (Superior-Inferior) (mm) |
|---|---|---|---|
| Registration #1 | 1.94 | 3.42 | 3.14 |
| Registration #2 | 1.28 | 3.97 | 1.62 |
| Registration #3 | 0.88 | 1.78 | 0.90 |
| Registration #4 | 0.22 | 3.52 | 1.77 |
| Registration #5 | 0.52 | 3.70 | 0.96 |
| Mean | 0.97 | 3.28 | 1.68 |

**b)**

| Femur Phantom #2 | Rotation about X-axis (Medial-Lateral) (degrees) | Rotation about Y-axis (Anterior-Posterior) (degrees) | Rotation about Z-axis (Superior-Inferior) (degrees) |
|---|---|---|---|
| Registration #1 | 0.65 | 0.20 | 0.01 |
| Registration #2 | 1.09 | 0.54 | 0.67 |
| Registration #3 | 0.71 | 0.12 | 1.48 |
| Registration #4 | 1.22 | 0.04 | 3.77 |
| Registration #5 | 1.16 | 0.23 | 3.07 |
| Mean | 0.96 | 0.22 | 1.80 |

**c)**

| Tibia Phantom #2 | X translation error (Medial-Lateral) (mm) | Y translation error (Anterior-Posterior) (mm) | Z translation error (Superior-Inferior) (mm) |
|---|---|---|---|
| Registration #1 | 0.19 | 1.89 | 0.16 |
| Registration #2 | 1.28 | 1.74 | 2.50 |
| Registration #3 | 0.48 | 1.48 | 1.40 |
| Registration #4 | 0.65 | 1.55 | 1.69 |
| Registration #5 | 1.96 | 1.28 | 2.39 |
| Mean | 0.91 | 1.59 | 1.63 |

**d)**

| Tibia Phantom #2 | Rotation about X-axis (Medial-Lateral) (degrees) | Rotation about Y-axis (Anterior-Posterior) (degrees) | Rotation about Z-axis (Superior-Inferior) (degrees) |
|---|---|---|---|
| Registration #1 | 0.18 | 0.80 | 0.70 |
| Registration #2 | 0.17 | 0.16 | 1.04 |
| Registration #3 | 0.06 | 0.43 | 0.37 |
| Registration #4 | 0.34 | 0.55 | 0.39 |
| Registration #5 | 0.29 | 0.21 | 2.98 |
| Mean | 0.21 | 0.43 | 1.09 |

a)

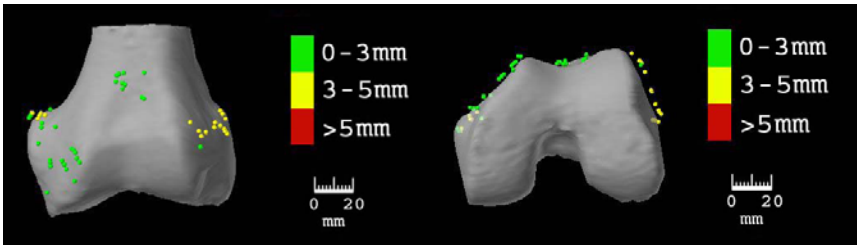


b)

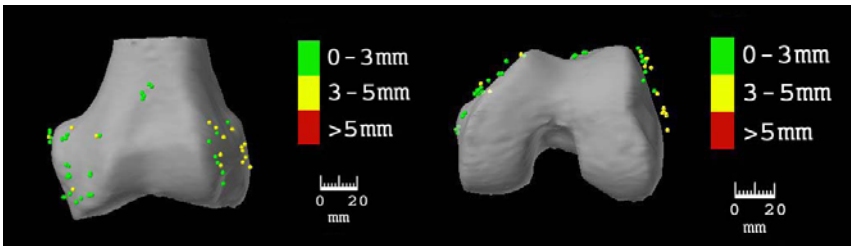


c)

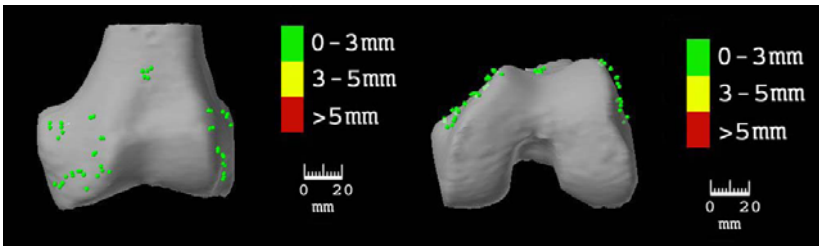


d)

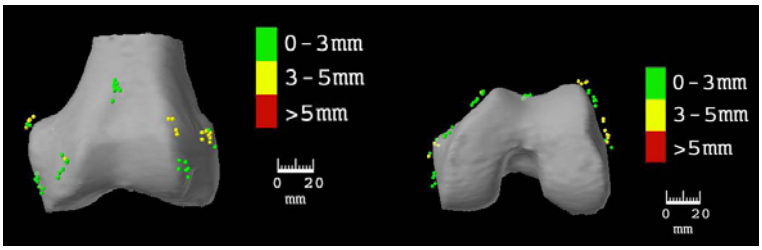


e)

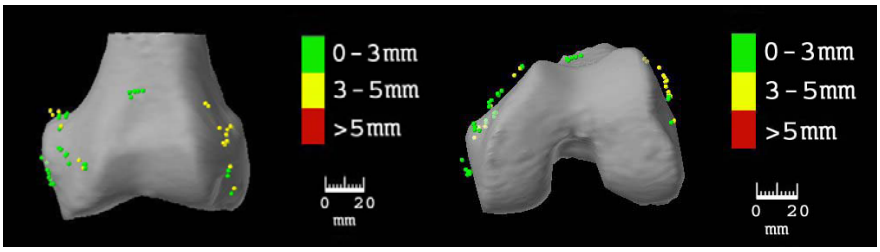


**Figure 5.8 Femur registrations for phantom #2. a) registration #1, b) registration #2, c) registration #3, d) registration #4, e) registration #5. The phantom femur segmented model is displayed with ultrasound data points from coronal and transverse perspectives. The ultrasound points were calculated using a speed of sound constant of 1540 m/s. The points are transformed using the ground truth registration from the standard registration approach. The distance of the point from the model shows the quality of the ultrasound capture approach. Data points less than 3 mm away are shown in green, points that are between 3 and 5 mm away are shown in yellow, and points that are greater than 5 mm away are shown in red.**

a)

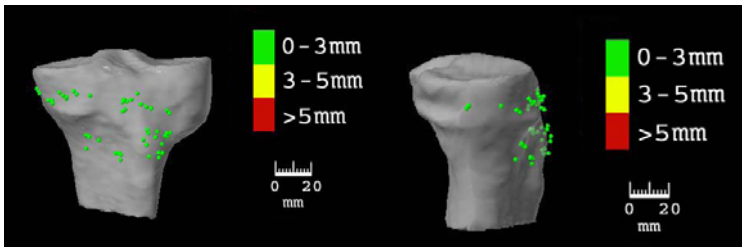


b)

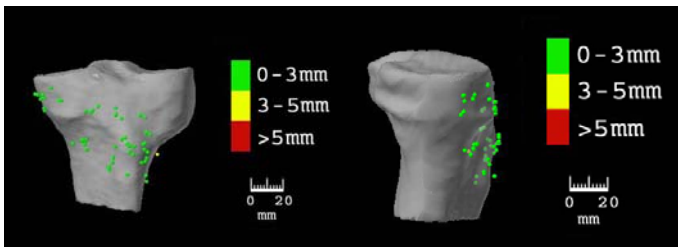


c)

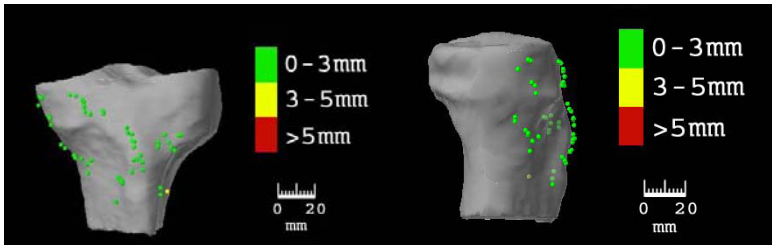


d)

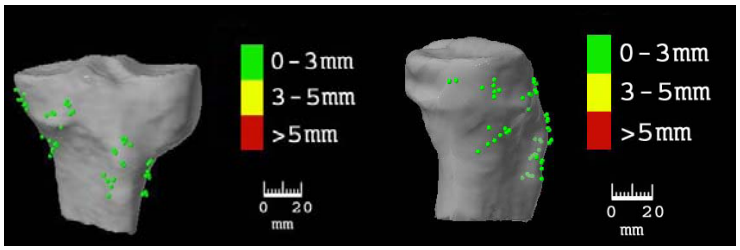


e)

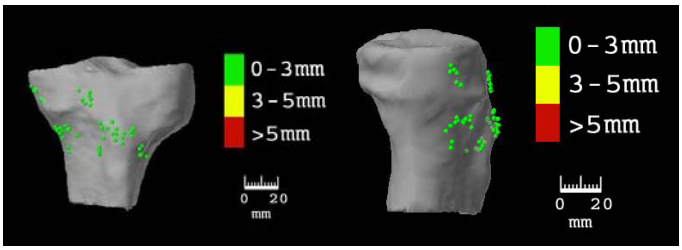


**Figure 5.9 Tibia registrations for phantom #2. a) registration #1, b) registration #2, c) registration #3, d) registration #4, e) registration #5. The phantom tibia segmented model is displayed with ultrasound data points from coronal and sagittal perspectives. The ultrasound points were calculated using a speed of sound constant of 1540 m/s. The points are transformed using the ground truth registration from the standard registration approach. The distance of the point from the model shows the quality of the ultrasound capture approach. Data points less than 3 mm away are shown in green, points that are between 3 and 5 mm away are shown in yellow, and points that are greater than 5 mm away are shown in red.**

### 5.3 Signal Processing Results

In the overall filtering scheme that was used to process an ultrasound signal, one key component was the low-pass filter. The low-pass filter served to envelope the raw ultrasound data and allow for a threshold filter to more easily be used. Several cutoff frequencies were tested on ultrasound data: 0.004, 0.01, and 0.03. Ten signals that ought to yield a positively detected bone and ten signals that should be rejected by the filter were used to test the filter. A signal that has a strong bone signal will have two characteristic peaks indicating the standoff/skin surface and the tissue/bone surface. These peaks should be separated from each other by a few millimeters and not be too close to the face of the transducer (the origin of the signal) nor too far since the bone is relatively shallow. These signals were categorized by inspection. For the threshold filter, a value of 1.5x the average signal value was consistently used for all of the processing. Figures 5.10-5.19 show the results of applying the filters with the three cut-off frequencies to the raw ultrasound data with valid bone signals and Figures 5.20-5.29 show the results of applying the filters to signals that should be rejected.

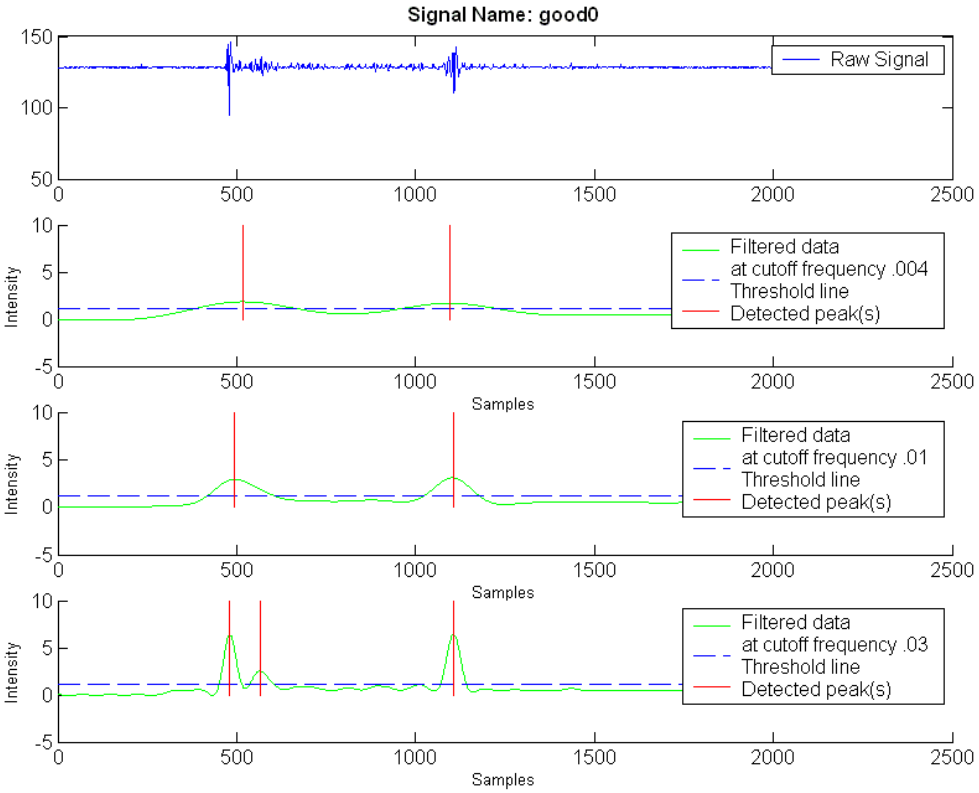


**Figure 5.10 Good bone signal #1 processed with different filters. The original ultrasound signal is displayed at the top in blue. The next three graphs show the results of applying the low-pass filter with cutoff frequencies of 0.004, 0.01, and 0.03 respectively. The filter with cutoff frequency of 0.004 successfully detected the double-peak. The filter with cutoff frequency of 0.01 successfully detected the double-peak. The filter with cutoff frequency 0.03 was too sensitive and detected an extra peak, thereby failing to find the bone surface.**

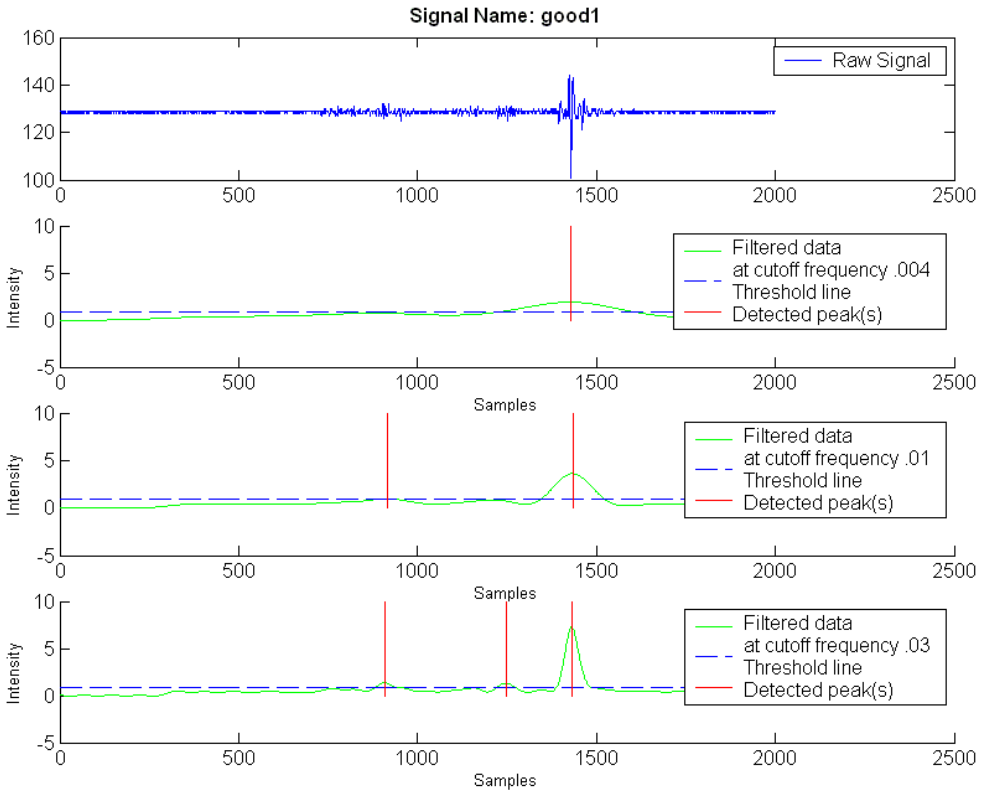


**Figure 5.11 Good bone signal #2 processed with different filters. The original ultrasound signal is displayed at the top in blue. The next three graphs show the results of applying the low-pass filter with cutoff frequencies of 0.004, 0.01, and 0.03 respectively. The filter with cutoff frequency of 0.004 failed to detect a double-peak. The filter with cutoff frequency of 0.01 successfully detected the double-peak. The filter with cutoff frequency 0.03 was too sensitive and detected an extra peak, thereby failing to find the bone surface.**

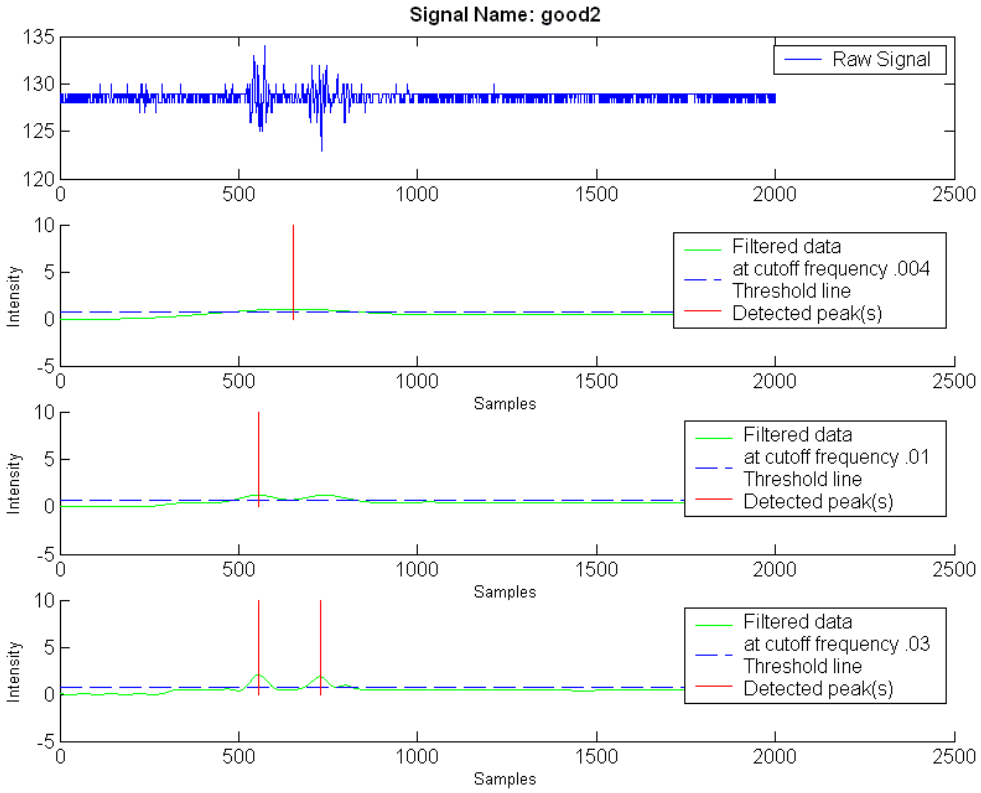


**Figure 5.12 Good bone signal #3 processed with different filters. The original ultrasound signal is displayed at the top in blue. The next three graphs show the results of applying the low-pass filter with cutoff frequencies of 0.004, 0.01, and 0.03 respectively. The filter with cutoff frequency of 0.004 failed to detect the double-peak. The filter with cutoff frequency of 0.01 failed to detect the double-peak. The filter with cutoff frequency 0.03 was too successfully detected the double-peak.**

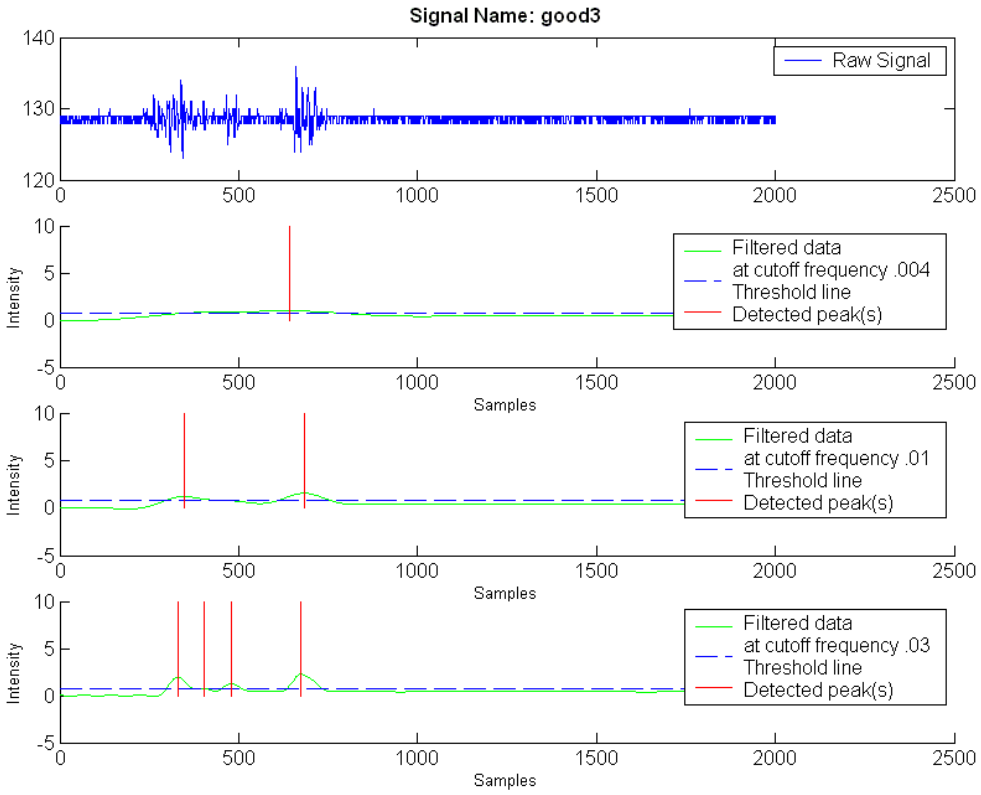


**Figure 5.13 Good bone signal #4 processed with different filters. The original ultrasound signal is displayed at the top in blue. The next three graphs show the results of applying the low-pass filter with cutoff frequencies of 0.004, 0.01, and 0.03 respectively. The filter with cutoff frequency of 0.004 was not sensitive enough and failed to detect the double-peak. The filter with cutoff frequency of 0.01 successfully detected the double-peak. The filter with cutoff frequency 0.03 was too sensitive and detected extra peaks, thereby failing to find the bone surface.**

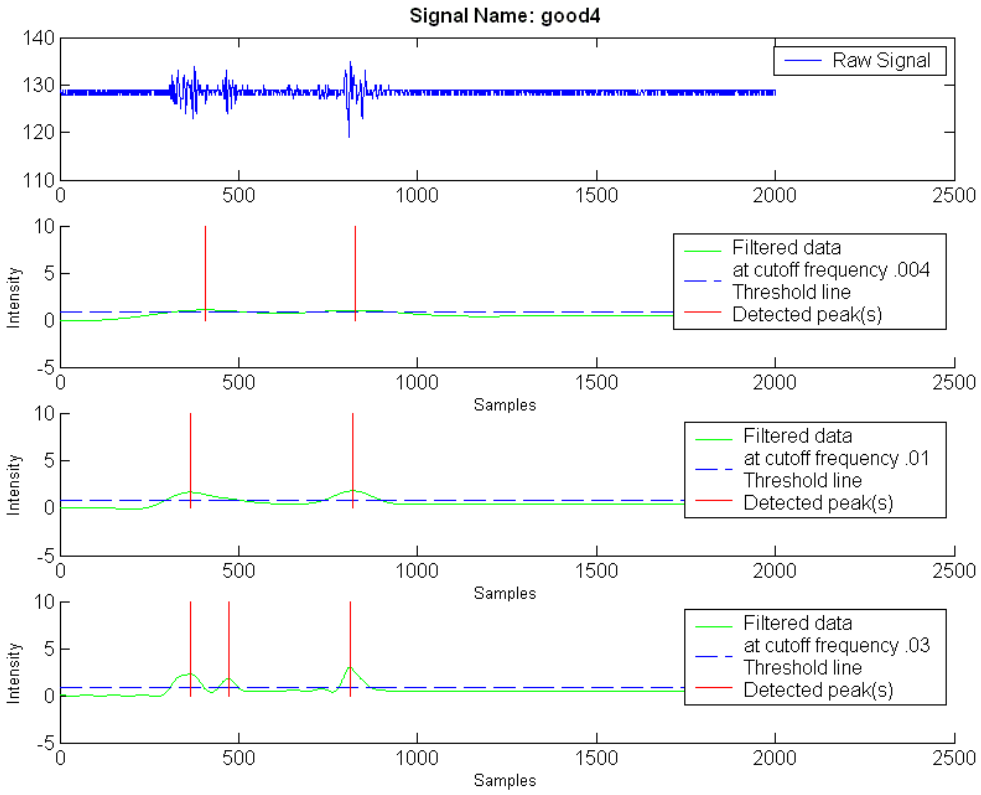


**Figure 5.14 Good bone signal #5 processed with different filters. The original ultrasound signal is displayed at the top in blue. The next three graphs show the results of applying the low-pass filter with cutoff frequencies of 0.004, 0.01, and 0.03 respectively. The filter with cutoff frequency of 0.004 successfully detected the double-peak. The filter with cutoff frequency of 0.01 successfully detected the double-peak. The filter with cutoff frequency 0.03 was too sensitive and detected an extra peak, thereby failing to find the bone surface.**

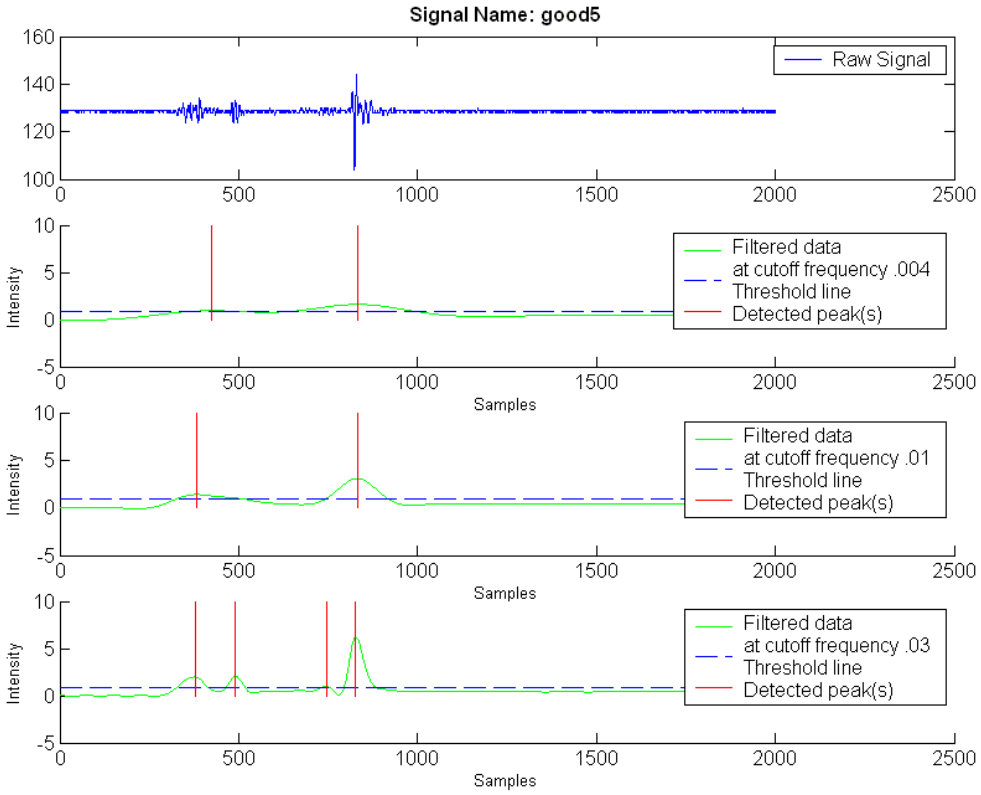


**Figure 5.15 Good bone signal #6 processed with different filters. The original ultrasound signal is displayed at the top in blue. The next three graphs show the results of applying the low-pass filter with cutoff frequencies of 0.004, 0.01, and 0.03 respectively. The filter with cutoff frequency of 0.004 successfully detected the double-peak. The filter with cutoff frequency of 0.01 successfully detected the double-peak. The filter with cutoff frequency 0.03 was too sensitive and detected extra peaks, thereby failing to find the bone surface.**

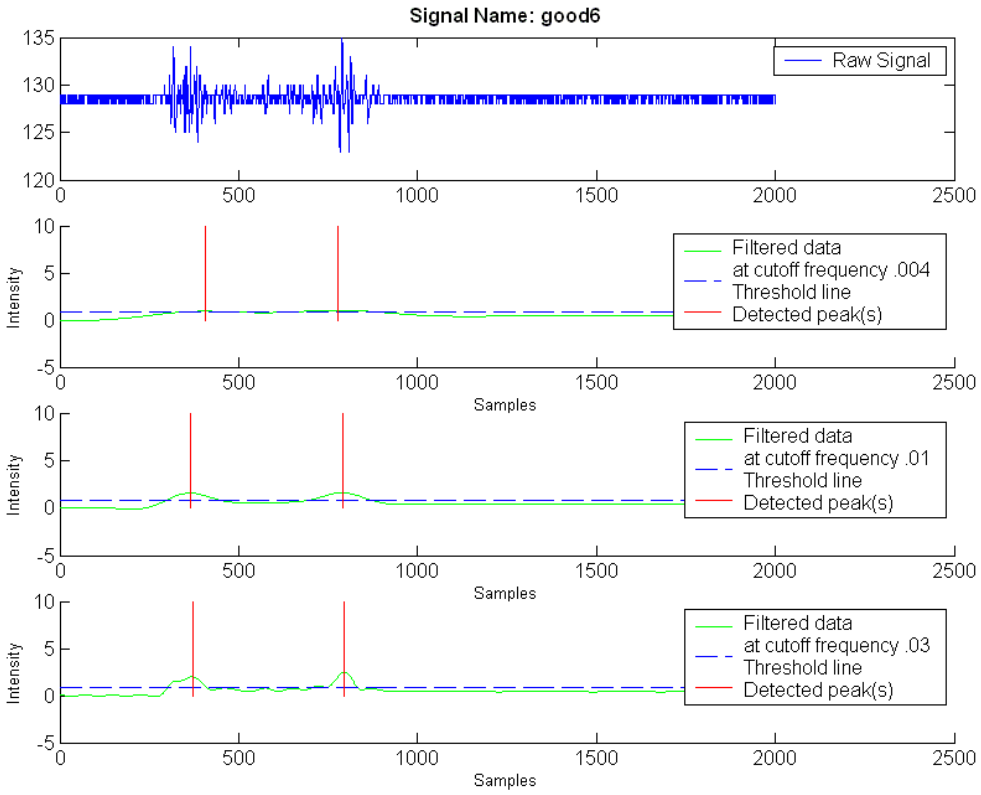


**Figure 5.16 Good bone signal #7 processed with different filters. The original ultrasound signal is displayed at the top in blue. The next three graphs show the results of applying the low-pass filter with cutoff frequencies of 0.004, 0.01, and 0.03 respectively. All three filters successfully find the bone surface.**

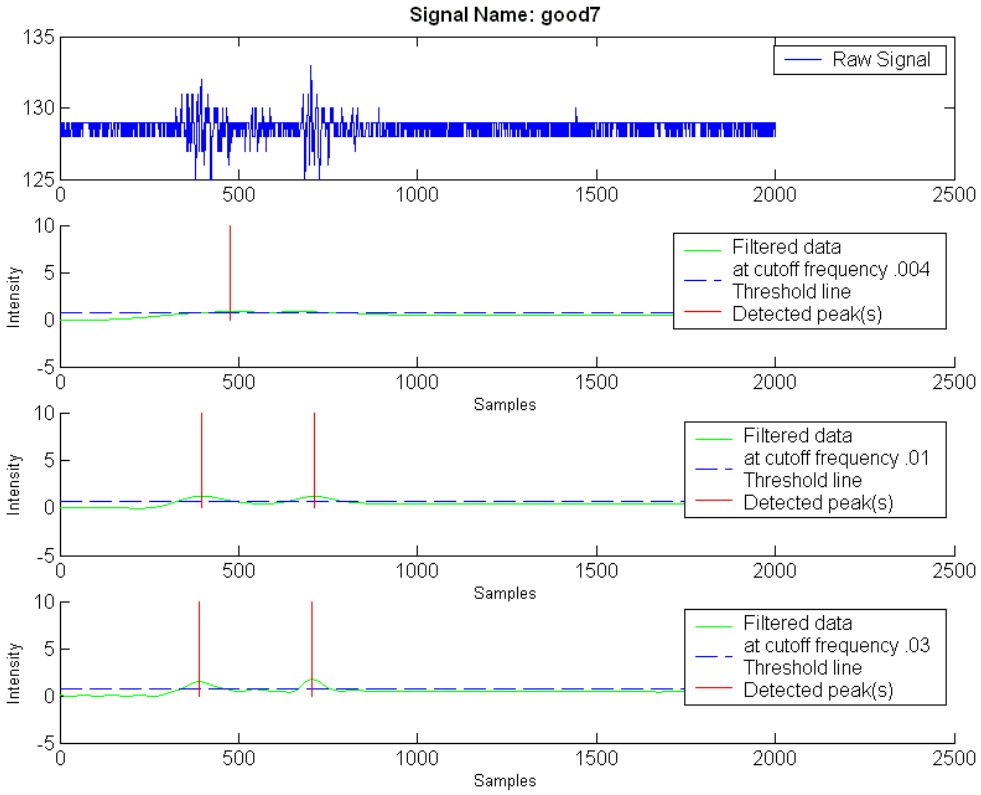


**Figure 5.17 Good bone signal #8 processed with different filters. The original ultrasound signal is displayed at the top in blue. The next three graphs show the results of applying the low-pass filter with cutoff frequencies of 0.004, 0.01, and 0.03 respectively. The filter with cutoff frequency of 0.004 failed due to being insensitive. The other two filters successfully find the bone surface.**

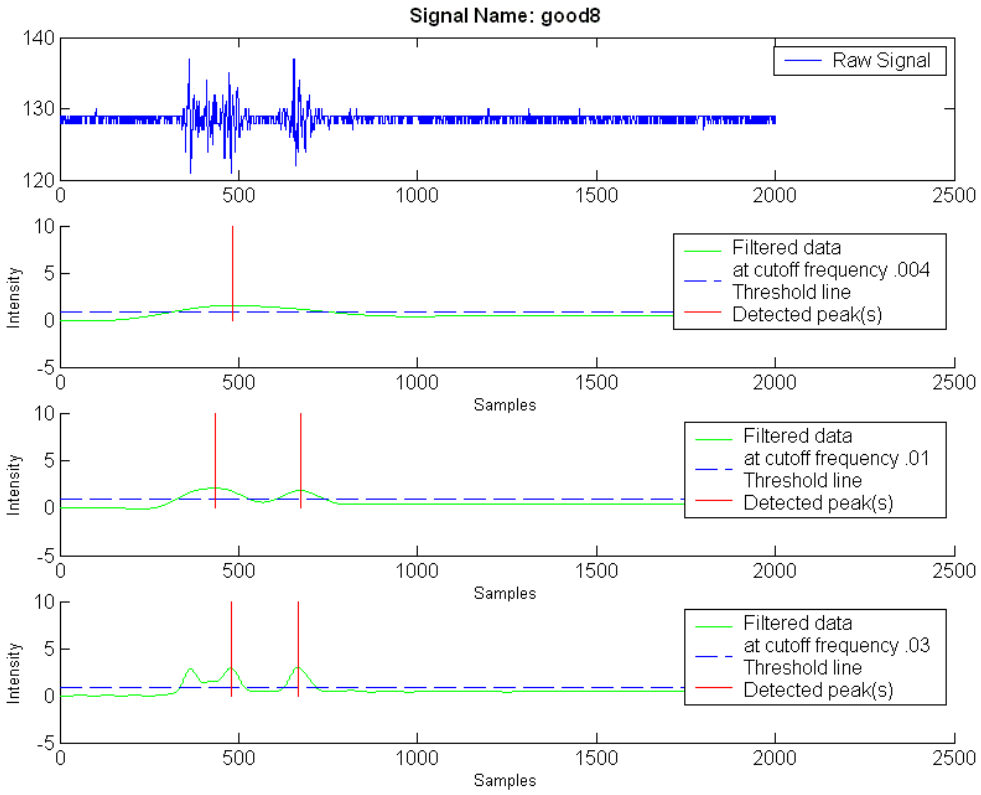


**Figure 5.18 Good bone signal #9 processed with different filters. The original ultrasound signal is displayed at the top in blue. The next three graphs show the results of applying the low-pass filter with cutoff frequencies of 0.004, 0.01, and 0.03 respectively. The filter with cutoff frequency of 0.004 failed due to being insensitive. The other two filters successfully find the bone surface.**

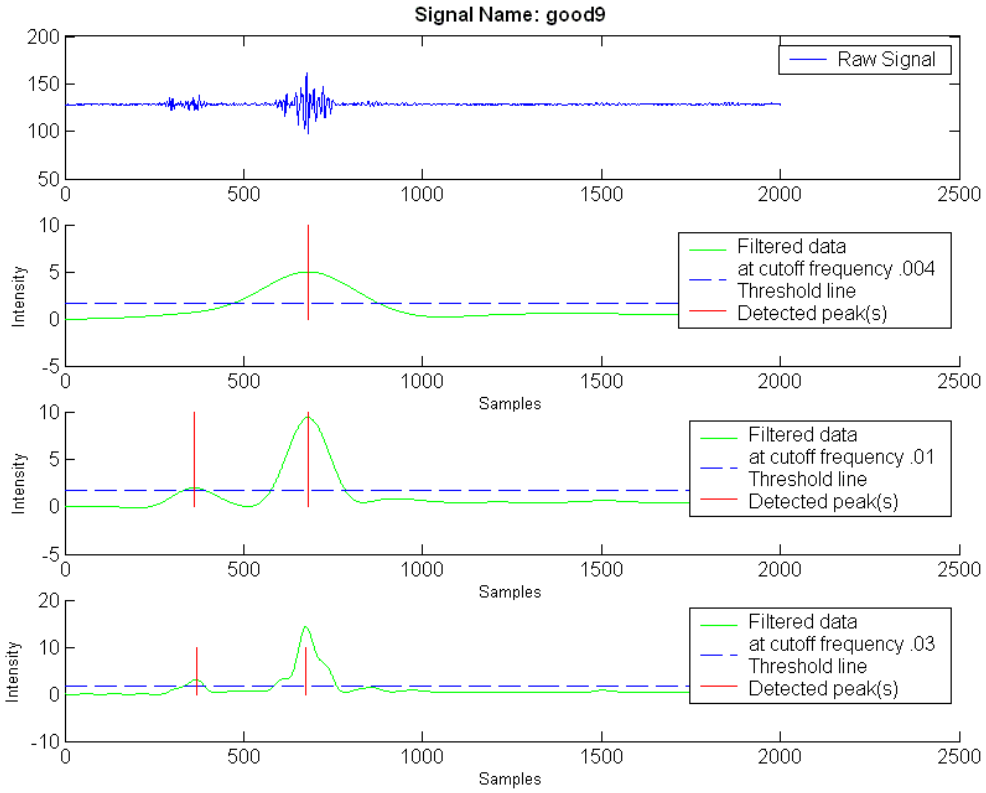


**Figure 5.19 Good bone signal #10 processed with different filters. The original ultrasound signal is displayed at the top in blue. The next three graphs show the results of applying the low-pass filter with cutoff frequencies of 0.004, 0.01, and 0.03 respectively. The filter with cutoff frequency of 0.004 failed due to being insensitive. The other two filters successfully find the bone surface.**

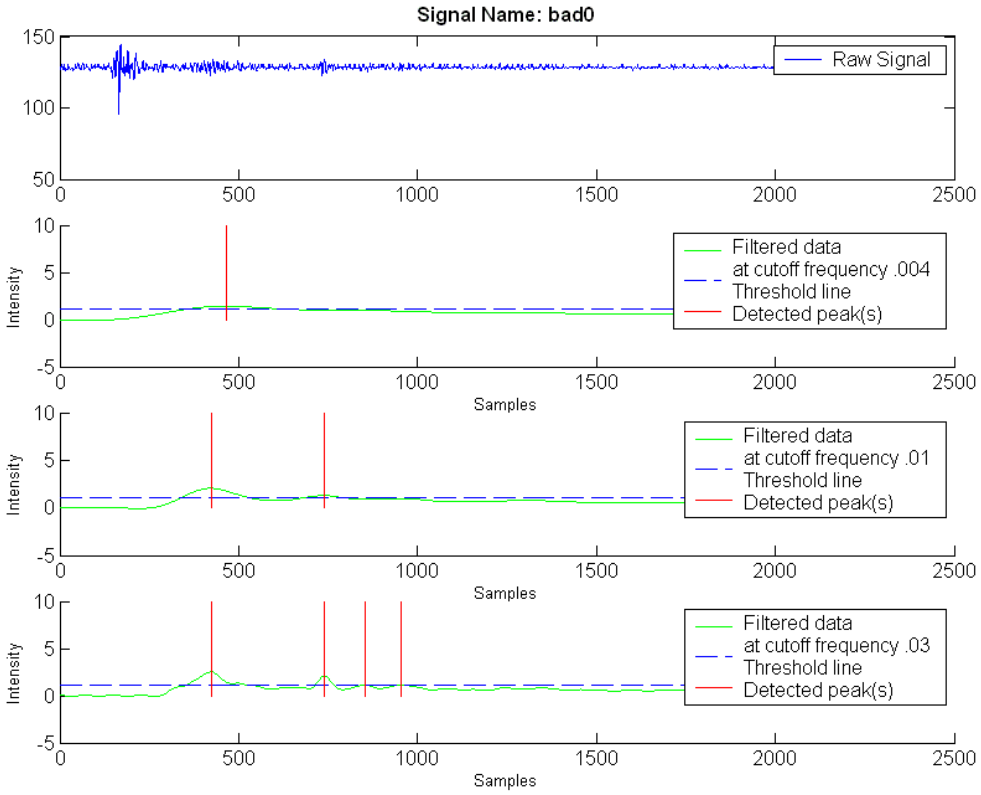


**Figure 5.20 Bad bone signal #1 processed with different filters. The original ultrasound signal is displayed at the top in blue. The next three graphs show the results of applying the low-pass filter with cutoff frequencies of 0.004, 0.01, and 0.03 respectively. The filter with cutoff frequency of 0.004 successfully rejects the signal. The filter with cutoff frequency of 0.01 incorrectly determines that a bone surface exists. The filter with cutoff frequency of 0.03 rejects the signal since it finds more than two unique peaks.**

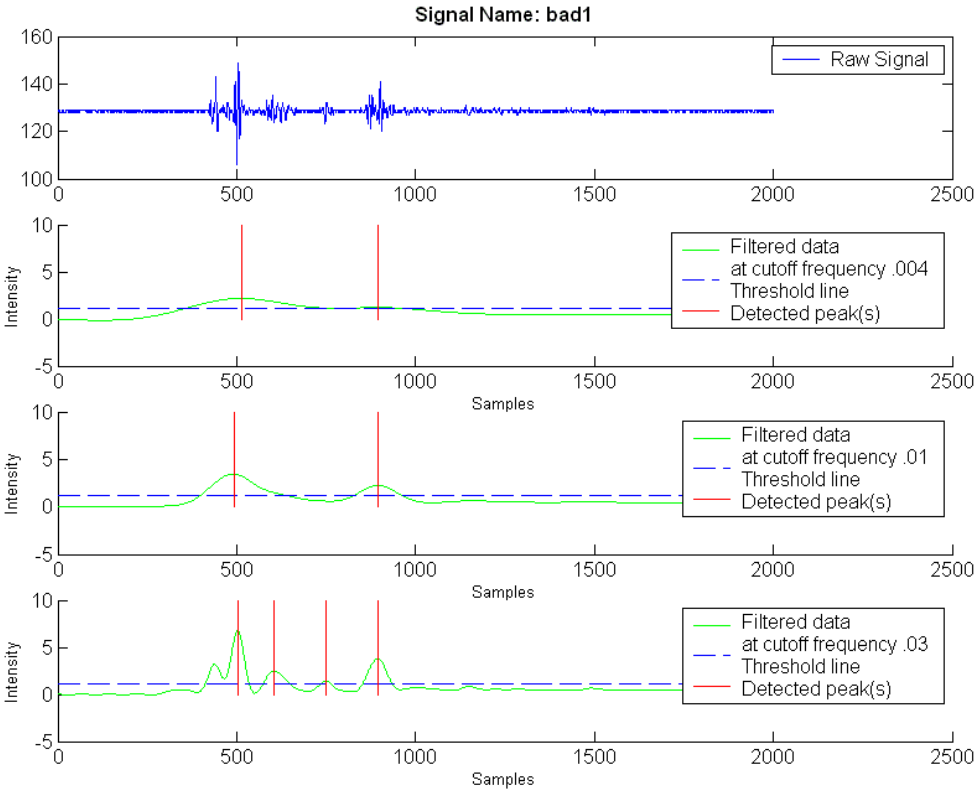


**Figure 5.21 Bad bone signal #2 processed with different filters. The original ultrasound signal is displayed at the top in blue. The next three graphs show the results of applying the low-pass filter with cutoff frequencies of 0.004, 0.01, and 0.03 respectively. The first two filters incorrectly determine that a bone surface exists. The filter with cutoff frequency of 0.03 rejects the signal since it finds more than two unique peaks.**

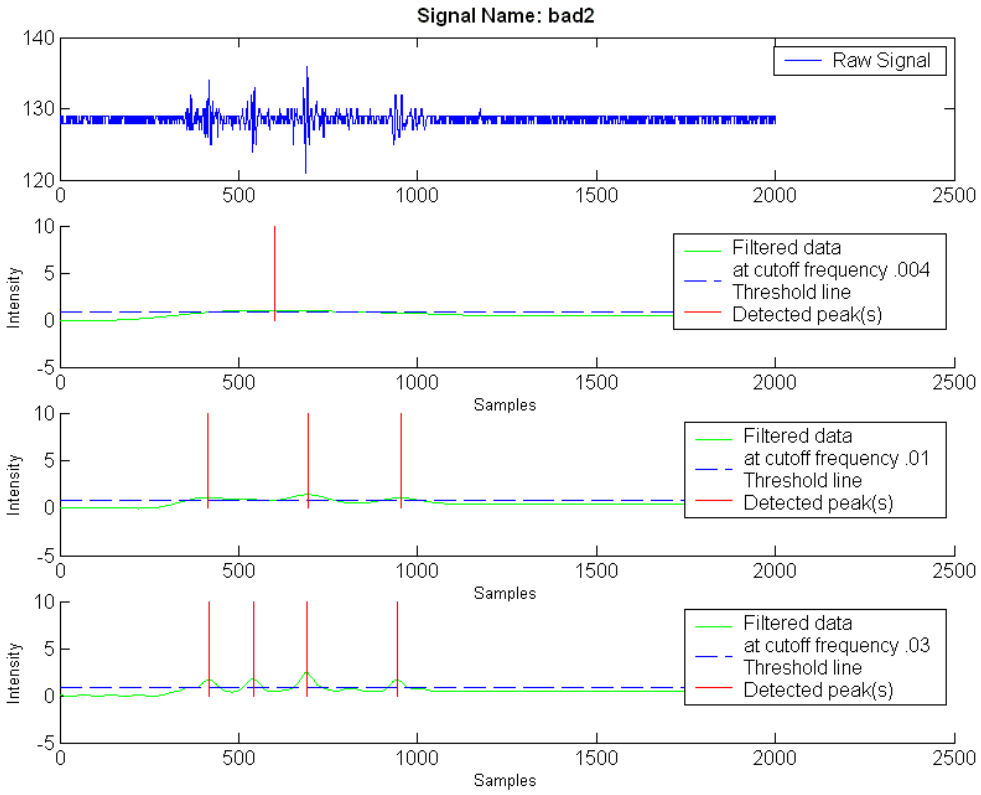


**Figure 5.22 Bad bone signal #3 processed with different filters. The original ultrasound signal is displayed at the top in blue. The next three graphs show the results of applying the low-pass filter with cutoff frequencies of 0.004, 0.01, and 0.03 respectively. All three filters successfully reject the signal as not having two unique peaks.**

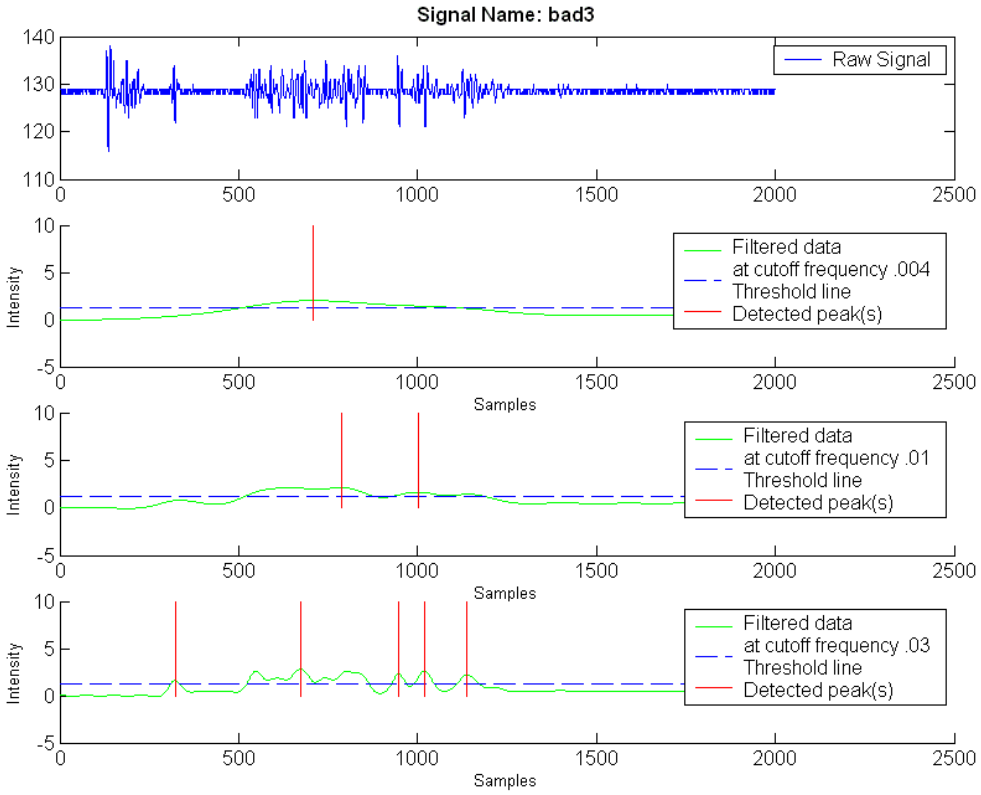


**Figure 5.23 Bad bone signal #4 processed with different filters. The original ultrasound signal is displayed at the top in blue. The next three graphs show the results of applying the low-pass filter with cutoff frequencies of 0.004, 0.01, and 0.03 respectively. The filters with cutoff frequencies of 0.004 and 0.03 successfully reject the signal. The filter with cutoff frequency of 0.01 incorrectly determines that a bone surface exists.**

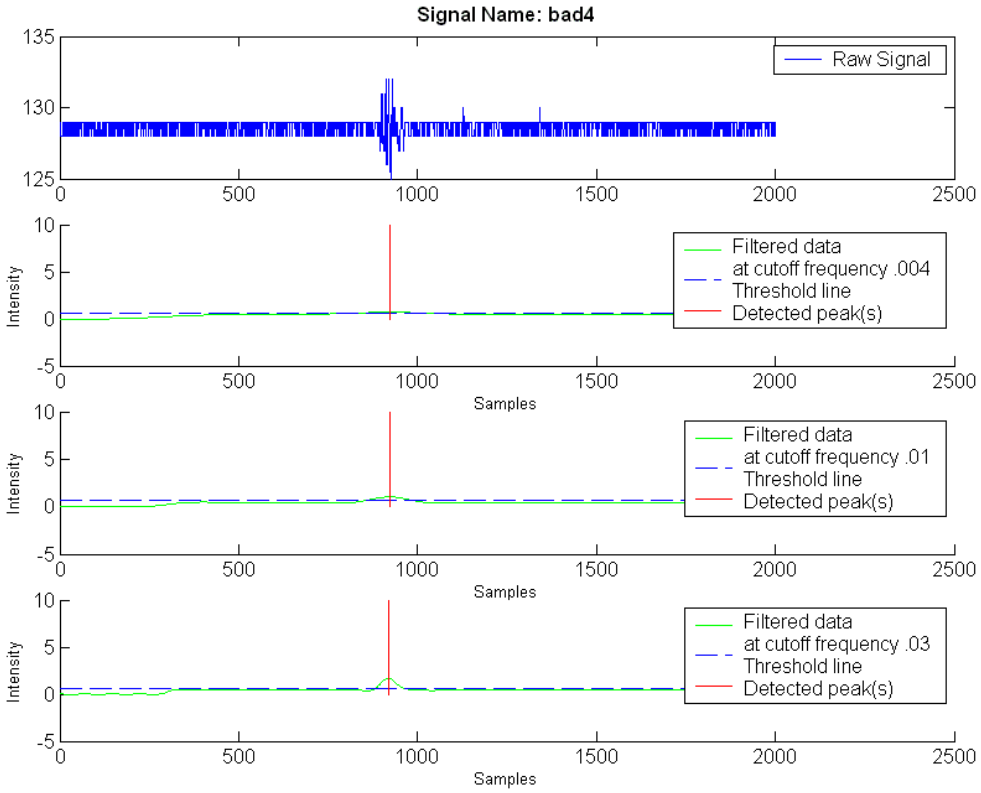


**Figure 5.24 Bad bone signal #5 processed with different filters. The original ultrasound signal is displayed at the top in blue. The next three graphs show the results of applying the low-pass filter with cutoff frequencies of 0.004, 0.01, and 0.03 respectively. All the filters successfully reject the signal since they only find a single peak.**

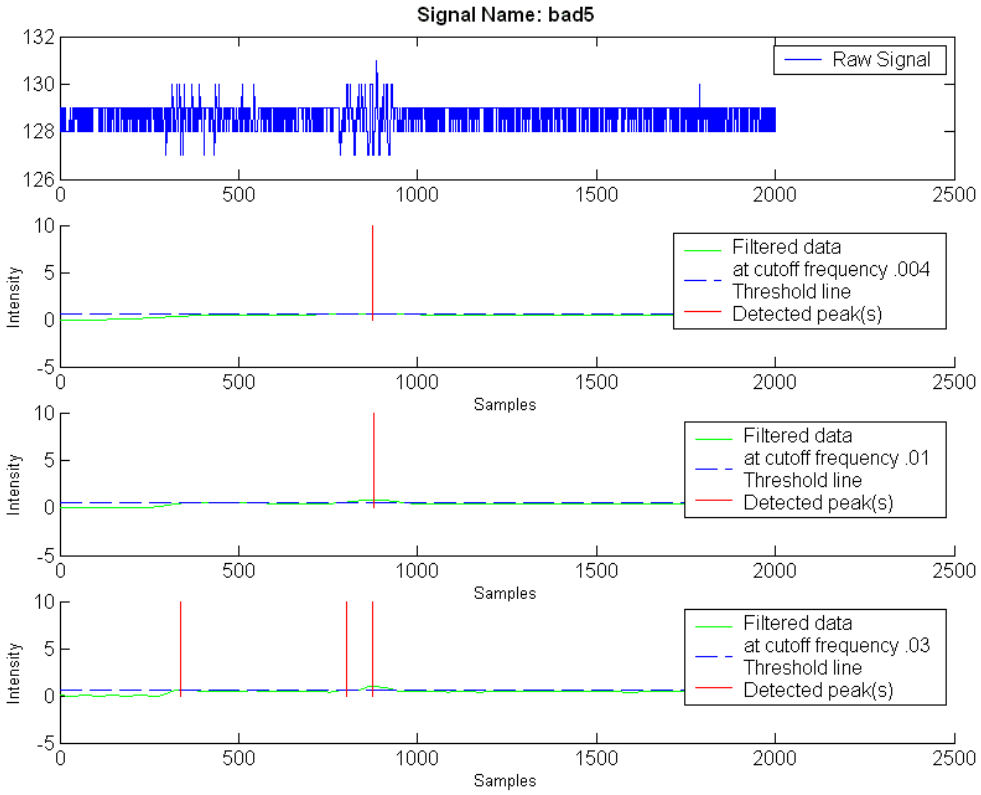


**Figure 5.25 Bad bone signal #6 processed with different filters. The original ultrasound signal is displayed at the top in blue. The next three graphs show the results of applying the low-pass filter with cutoff frequencies of 0.004, 0.01, and 0.03 respectively. All filters successfully reject the signal since none find a double peak.**

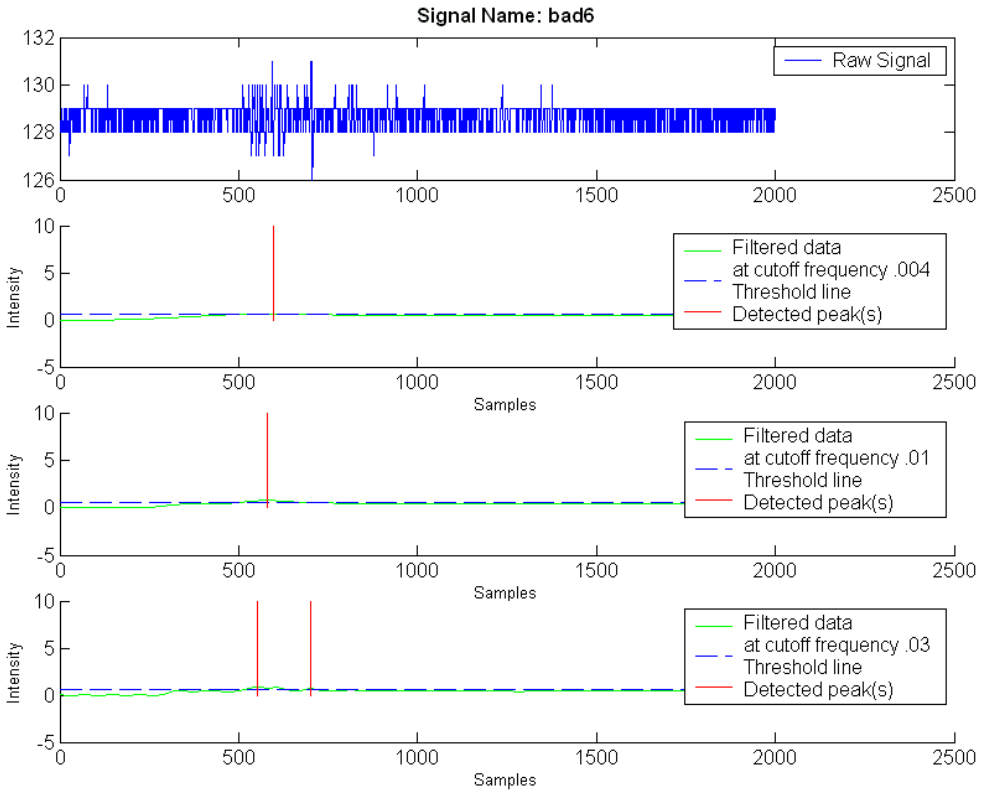


**Figure 5.26 Bad bone signal #7 processed with different filters. The original ultrasound signal is displayed at the top in blue. The next three graphs show the results of applying the low-pass filter with cutoff frequencies of 0.004, 0.01, and 0.03 respectively. The filters with cutoff frequencies of 0.004and 0.01 successfully reject the signal since they only find one unique peak. The filter with cutoff frequency of 0.03 incorrectly determines that a bone surface exists.**

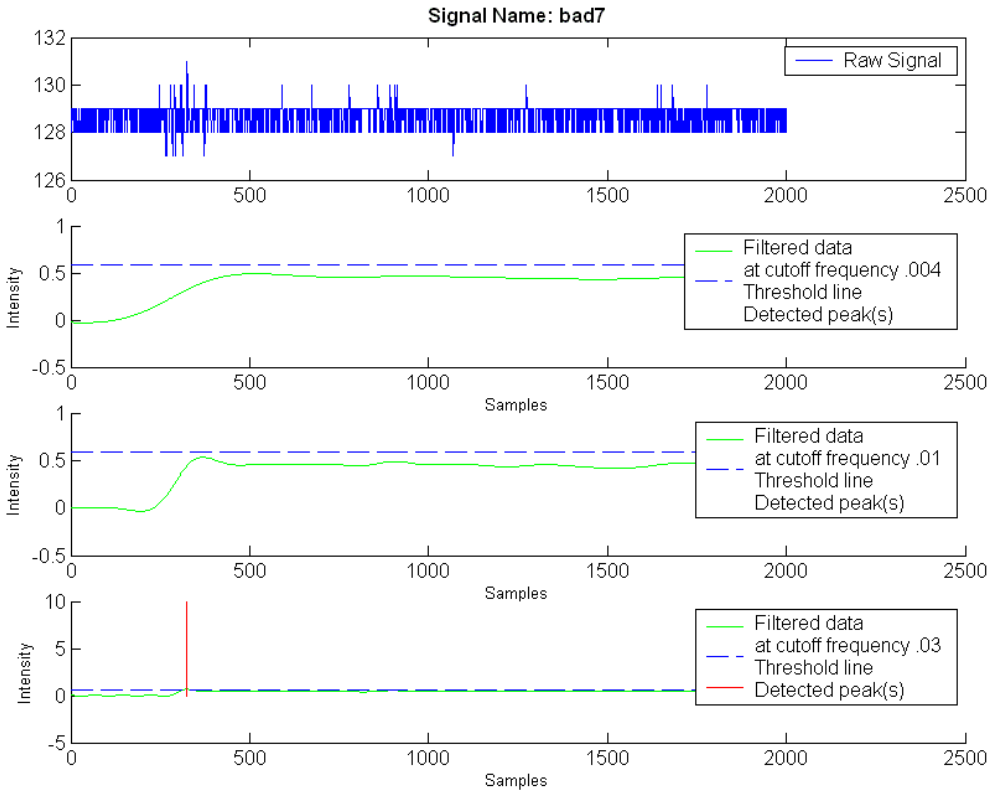


**Figure 5.27 Bad bone signal #8 processed with different filters. The original ultrasound signal is displayed at the top in blue. The next three graphs show the results of applying the low-pass filter with cutoff frequencies of 0.004, 0.01, and 0.03 respectively. All the filters successfully reject the signal.**

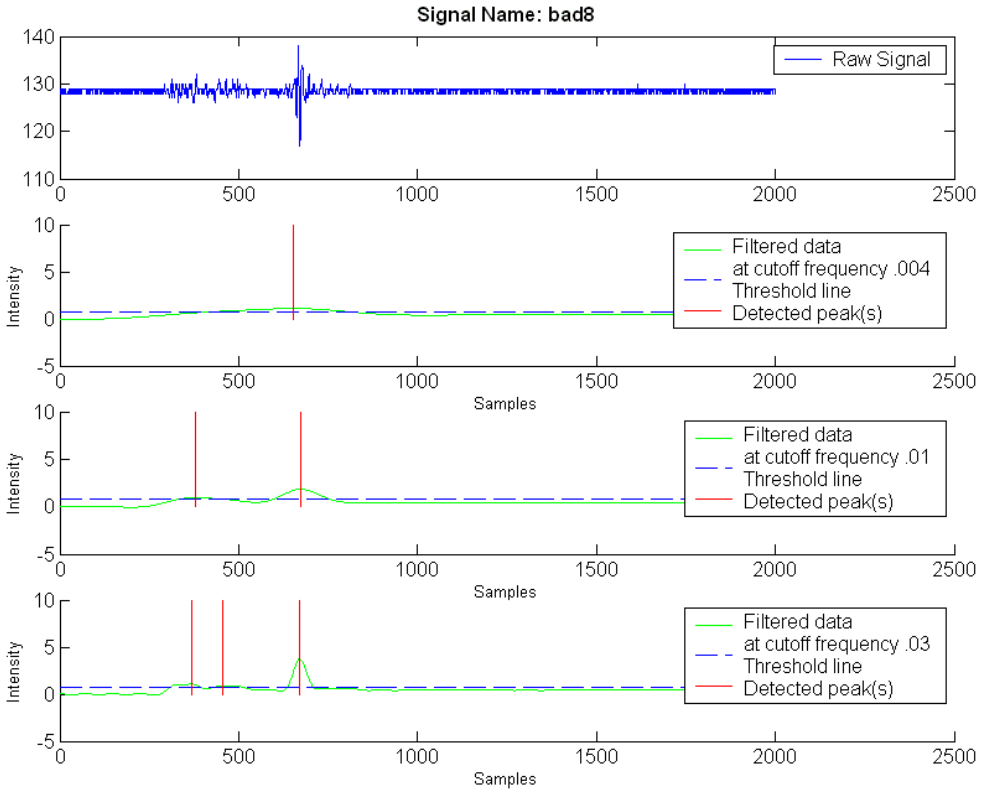


**Figure 5.28 Bad bone signal #9 processed with different filters. The original ultrasound signal is displayed at the top in blue. The next three graphs show the results of applying the low-pass filter with cutoff frequencies of 0.004, 0.01, and 0.03 respectively. The filter with cutoff frequency of 0.004 successfully rejects the signal. The filter with cutoff frequency of 0.01 incorrectly determines that a bone surface exists. The filter with cutoff frequency of 0.03 rejects the signal since it finds more than two unique peaks.**

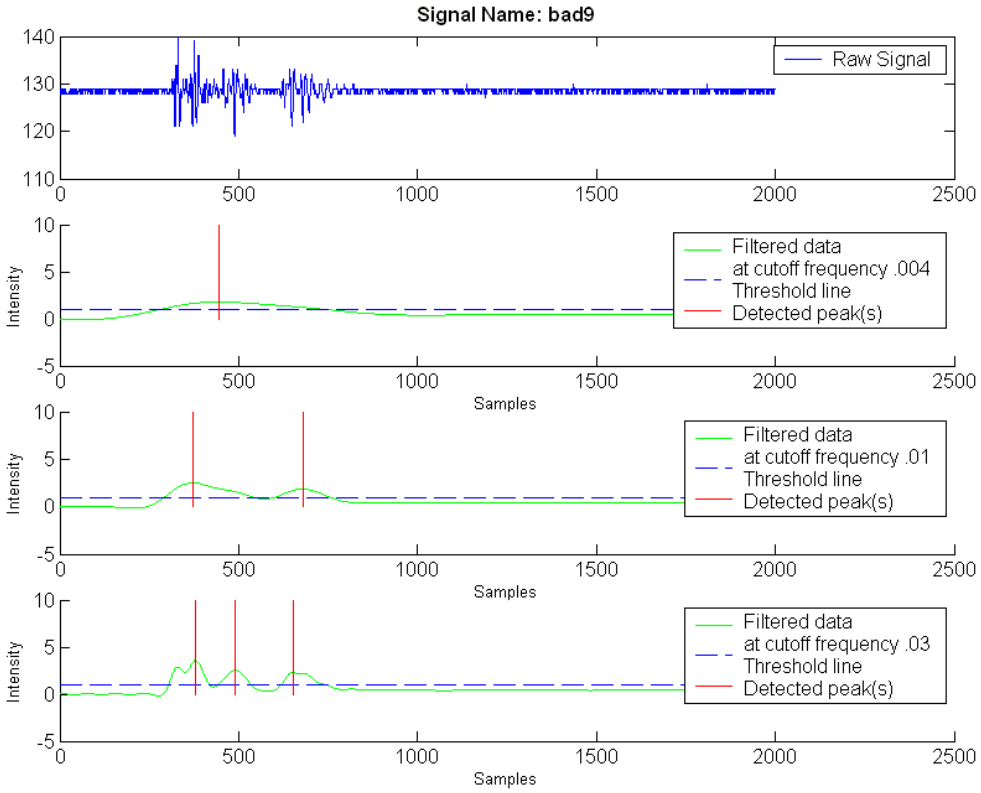


**Figure 5.29 Bad bone signal #10 processed with different filters. The original ultrasound signal is displayed at the top in blue. The next three graphs show the results of applying the low-pass filter with cutoff frequencies of 0.004, 0.01, and 0.03 respectively. The filter with cutoff frequency of 0.004 successfully rejects the signal. The filter with cutoff frequency of 0.01 incorrectly determines that a bone surface exists. The filter with cutoff frequency of 0.03 rejects the signal since it finds more than two unique peaks.**

## 5.4 Specimen Registration Results

Five registrations on each of three specimens were performed for each tibia and femur in the specimens. Various aspects of data collection improvement are tested including: standoff selection, length of scan, and anatomical patterns for collecting data. The results show comparisons to standard registration techniques using a mechanical probe. The quality of the ultrasound data is measured by transforming the collected ultrasound points using the standard registration. The visualization of this data

emphasizes the error of the ultrasound data collection by showing how far the points are from the surface of the image space bone model.

### 5.4.1 First Specimen Results

An RMS was calculated by determining the error at each sample point after the ultrasound registration is applied. The average RMS error for the tibia registrations was 1.51mm. The average RMS error for the femur registrations was 2.80mm. More importantly, a ground truth registration is compared to the ultrasound registrations. Results are also noted for CT scan length changes and standoff experiments.

#### 5.4.1.1 CT Scan Length Results

The first specimen was scanned using CT and a relatively long protocol. Normally, the scan covers 10 cm above and 10 cm below the knee joint. This usually yields about 400 image slices with 512 x 512 pixels. With the first specimen, the scan included approximately 20cm above and 20 cm below the joint. This resulted in nearly 1000 slices each with 512 x 512 pixels. The software ran exceptionally slowly due to the extra data from the scan. Occasionally, the software crashed as it was unable to load and display the larger image volumes. This caused the experiments to be prohibitively slow. Data was still collected on the distal tibia and proximal femur beyond what would normally be accessible, and the results are shown in Table 5.5 and Figures 5.30 and 5.31.

#### 5.4.1.2 Standoff Results from First Specimen Registrations

Various standoffs were employed for the first specimen. A simple water-filled glove finger was used for the first three tibia registrations. An Aquaflex pad was used for the final two tibia registrations. Aquaflex pads are gelatinous, lubricated pads that are intended to provide a buffer between a transducer and the skin surface. However, the pad did not stand up to extended use and could degrade if registration takes a long time. Also, it was more difficult to guarantee a good signal since the pad was more cumbersome to use. In contrast, the water-filled glove finger was robust and easier to manipulate. It was attempted to not use any standoff at all, but the signals were not usable if a standoff was not present. The first three tibia registrations used a glove-finger standoff while the last two were performed with an Aquaflex gel pad standoff. Those results are presented in the following section.

#### 5.4.1.3 First Specimen Results Compared to Standard Method

Results of the first five registrations of the tibia and femur specimens were compared to registrations captured with a mechanical probe. The results were decomposed into errors for translation and rotation for each axis. The mean translation and rotation errors for both bones are displayed in Table 5.5.

**Table 5.5: Registration results for specimen #1 compared to standard registration with mechanical probe. The error is derived from a decomposed matrix that applies the inverse of the standard registration result with the ultrasound registration results. Rows with an * denote registrations that were performed with an Aquaflex gel pad for a standoff. Otherwise, all registrations were performed with a glove finger standoff. The table is broken down into errors for a) translation for femur, b) rotation for femur, c) translation for tibia, and d) rotation for tibia for each axis.**

**a)**

| Femur Specimen #1 | X translation error (Medial-Lateral) (mm) | Y translation error (Anterior-Posterior) (mm) | Z translation error (Superior-Inferior) (mm) |
|---|---|---|---|
| Registration #1 | 4.75 | 6.36 | 3.35 |
| Registration #2 | 2.21 | 1.16 | 6.72 |
| Registration #3 | 0.74 | 0.21 | 0.88 |
| Registration #4 | 3.26 | 1.41 | 1.64 |
| Registration #5 | 2.36 | 1.19 | .031 |
| Mean | 2.66 | 2.07 | 2.58 |

**b)**

| Femur Specimen #1 | Rotation about X-axis (Medial-Lateral) (degrees) | Rotation about Y-axis (Anterior-Posterior) (degrees) | Rotation about Z-axis (Superior-Inferior) (degrees) |
|---|---|---|---|
| Registration #1 | 1.62 | 0.75 | 6.36 |
| Registration #2 | 1.02 | 2.00 | 5.09 |
| Registration #3 | 3.01 | 0.19 | 1.39 |
| Registration #4 | 3.10 | 1.27 | 6.81 |
| Registration #5 | 3.93 | 0.03 | 10.19 |
| Mean | 2.53 | 0.85 | 5.97 |

**c)**

| Tibia Specimen #1 | X translation error (Medial-Lateral) (mm) | Y translation error (Anterior-Posterior) (mm) | Z translation error (Superior-Inferior) (mm) |
|---|---|---|---|
| Registration #1 | 0.28 | 1.01 | 1.40 |
| Registration #2 | 1.71 | 0.48 | 1.04 |
| Registration #3 | 0.59 | 1.87 | 1.05 |
| Registration #4* | 0.17 | 3.94 | 1.68 |
| Registration #5* | 3.71 | 7.12 | 6.95 |
| Mean | 1.29 | 2.88 | 2.43 |

**d)**

| Tibia Specimen #1 | Rotation about X-axis (Medial-Lateral) (degrees) | Rotation about Y-axis (Anterior-Posterior) (degrees) | Rotation about Z-axis (Superior-Inferior) (degrees) |
|---|---|---|---|
| Registration #1 | 0.08 | 0.58 | 1.07 |
| Registration #2 | 2.03 | 0.90 | 5.22 |
| Registration #3 | 0.17 | 0.44 | 2.94 |
| Registration #4* | 1.39 | 0.88 | 9.76 |
| Registration #5* | 1.77 | 2.38 | 48.79 |
| Mean | 1.09 | 1.04 | 13.55 |

a)

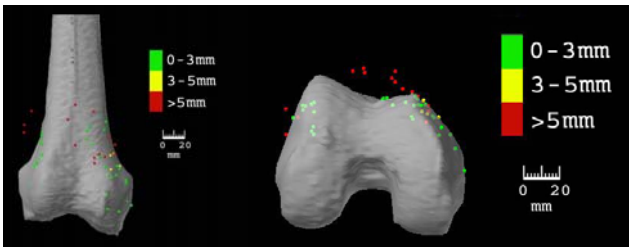


b)

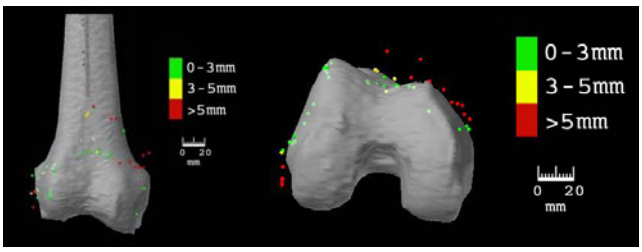


c)

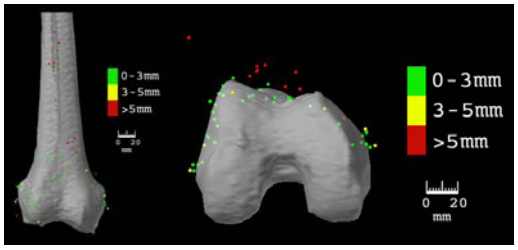


d)

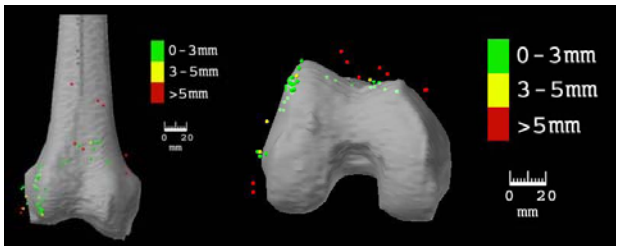


e)

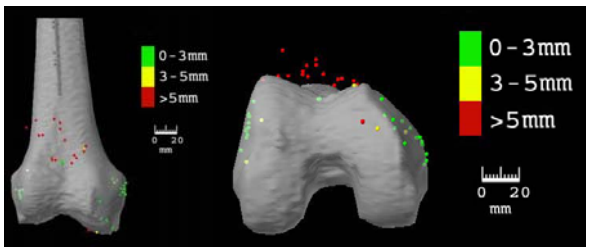


**Figure 5.30 Femur registrations for specimen #1. a) registration #1, b) registration #2, c) registration #3, d) registration #4, e) registration #5. The femur specimen segmented model is displayed with ultrasound data points from coronal and transverse perspectives. The points are transformed using the ground truth registration from the standard registration approach. The distance of the point from the model shows the quality of the ultrasound capture approach. Data points less than 3 mm away are shown in green, points that are between 3 and 5 mm away are shown in yellow, and points that are greater than 5 mm away are shown in red.**

a)

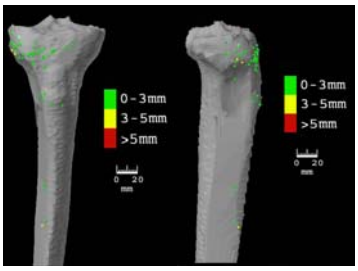


b)

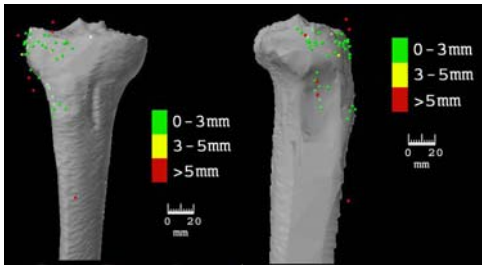


c)

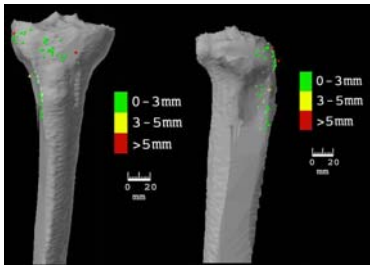


d)

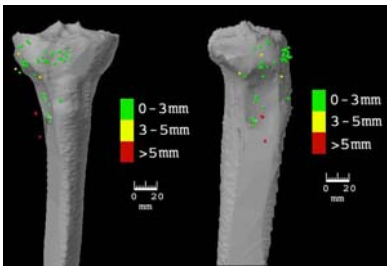


e)

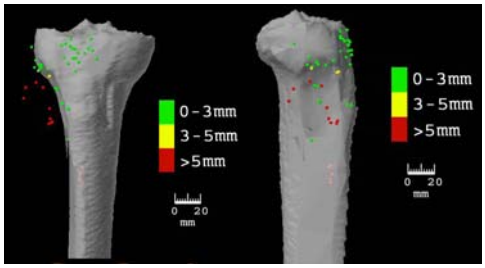


**Figure 5.31 Tibia registrations for specimen #1. a) registration #1, b) registration #2, c) registration #3, d) registration #4, e) registration #5. The registration results shown in a), b), and c) were captured with a water-filled glove finger as a standoff, whereas registrations shown in d) end e) were captured using an Aquaflex gel pad. The tibia specimen segmented model is displayed with ultrasound data points from coronal and sagittal perspectives. The points are transformed using the ground truth registration from the standard registration approach. The distance of the point from the model shows the quality of the ultrasound capture approach. Data points less than 3 mm away are shown in green, points that are between 3 and 5 mm away are shown in yellow, and points that are greater than 5 mm away are shown in red.**

5.4.1.4 Second Specimen Results Compared to Standard Method

The results from the second specimen are displayed in Table 5.6. The tibia results are similar to those of the first specimen's registrations and highlight the need to constrain the rotation about the z-axis. The femur results are drastically worse with the second specimen. Some causes for this can be seen in the images that display the ultrasound data points properly transformed onto the bone specimen using the standard mechanical probe registration (Figs. 5.32 and 5.33).

**Table 5.6: Registration results for specimen #2 compared to standard registration with mechanical probe. The error is derived from a decomposed matrix that applies the inverse of the standard registration result with the ultrasound registration results. The table is broken down into errors for a) translation for femur, b) rotation for femur, c) translation for tibia, and d) rotation for tibia for each axis.**

**a)**

| Femur Specimen #2 | X translation error (Medial-Lateral) (mm) | Y translation error (Anterior-Posterior) (mm) | Z translation error (Superior-Inferior) (mm) |
|---|---|---|---|
| Registration #1 | 13.85 | 11.65 | 4.42 |
| Registration #2 | 13.22 | 17.27 | 2.63 |
| Registration #3 | 7.19 | 12.02 | 2.41 |
| Registration #4 | 11.96 | 9.82 | 0.93 |
| Registration #5 | 8.82 | 15.13 | 0.27 |
| Mean | 11.00 | 13.18 | 2.13 |

**b)**

| Femur Specimen #2 | Rotation about X-axis (Medial-Lateral) (degrees) | Rotation about Y-axis (Anterior-Posterior) (degrees) | Rotation about Z-axis (Superior-Inferior) (degrees) |
|---|---|---|---|
| Registration #1 | 2.50 | 0.14 | 21.90 |
| Registration #2 | 1.46 | 1.36 | 18.74 |
| Registration #3 | 2.04 | 0.06 | 16.72 |
| Registration #4 | 0.83 | 2.96 | 13.37 |
| Registration #5 | 1.23 | 1.68 | 6.94 |
| Mean | 1.61 | 1.24 | 15.53 |

**c)**

| Tibia Specimen #2 | X translation error (Medial-Lateral) (mm) | Y translation error (Anterior-Posterior) (mm) | Z translation error (Superior-Inferior) (mm) |
|---|---|---|---|
| Registration #1 | 0.32 | 1.65 | 6.44 |
| Registration #2 | 2.50 | 0.81 | 2.23 |
| Registration #3 | 5.56 | 0.50 | 5.20 |
| Registration #4 | 1.59 | 1.61 | 1.52 |
| Registration #5 | 3.72 | 2.23 | 2.69 |
| Mean | 2.74 | 1.36 | 3.61 |

**d)**

| Tibia Specimen #2 | Rotation about X-axis (Medial-Lateral) (degrees) | Rotation about Y-axis (Anterior-Posterior) (degrees) | Rotation about Z-axis (Superior-Inferior) (degrees) |
|---|---|---|---|
| Registration #1 | 0.57 | 1.37 | 6.39 |
| Registration #2 | 0.24 | 0.51 | 0.72 |
| Registration #3 | 0.56 | 1.73 | 3.42 |
| Registration #4 | 0.93 | 0.61 | 7.90 |
| Registration #5 | 0.86 | 0.76 | 7.77 |
| Mean | 0.63 | 1.00 | 5.24 |

a)

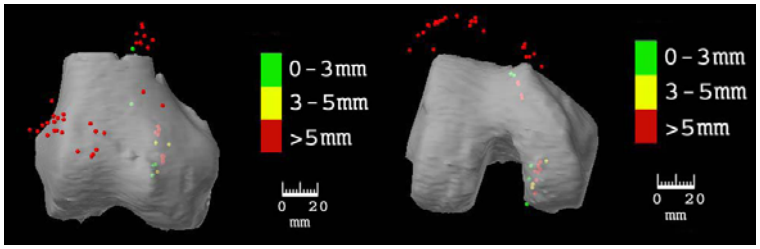


b)

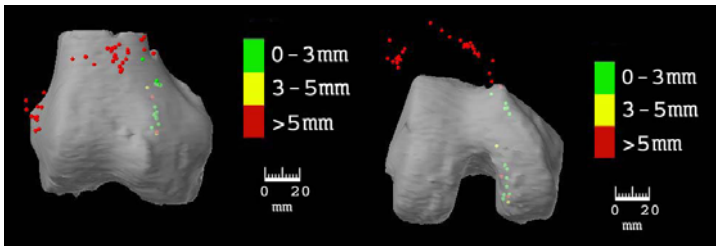


c)

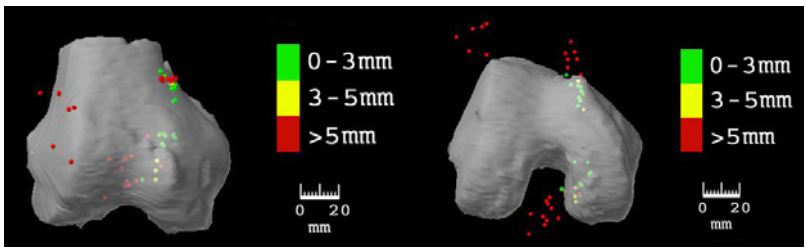


d)

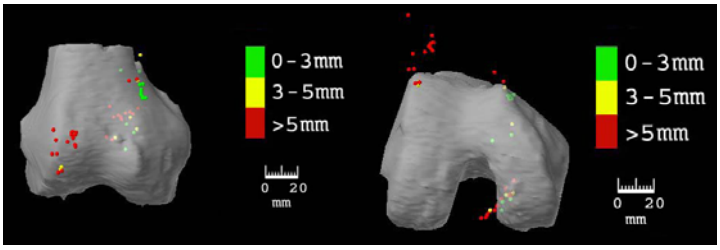


e)

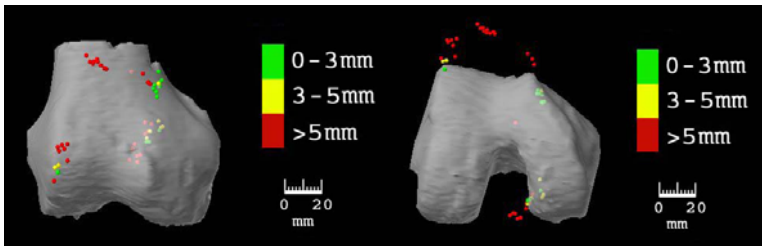


**Figure 5.32: Femur registrations for specimen #2. a) registration #1, b) registration #2, c) registration #3, d) registration #4, e) registration #5. The femur specimen segmented model is displayed with ultrasound data points from coronal and transverse perspectives. The points are transformed using the ground truth registration from the standard registration approach. The distance of the point from the model shows the quality of the ultrasound capture approach. Data points less than 3 mm away are shown in green, points that are between 3 and 5 mm away are shown in yellow, and points that are greater than 5 mm away are shown in red.**

a)

b)

c)

d)

e)

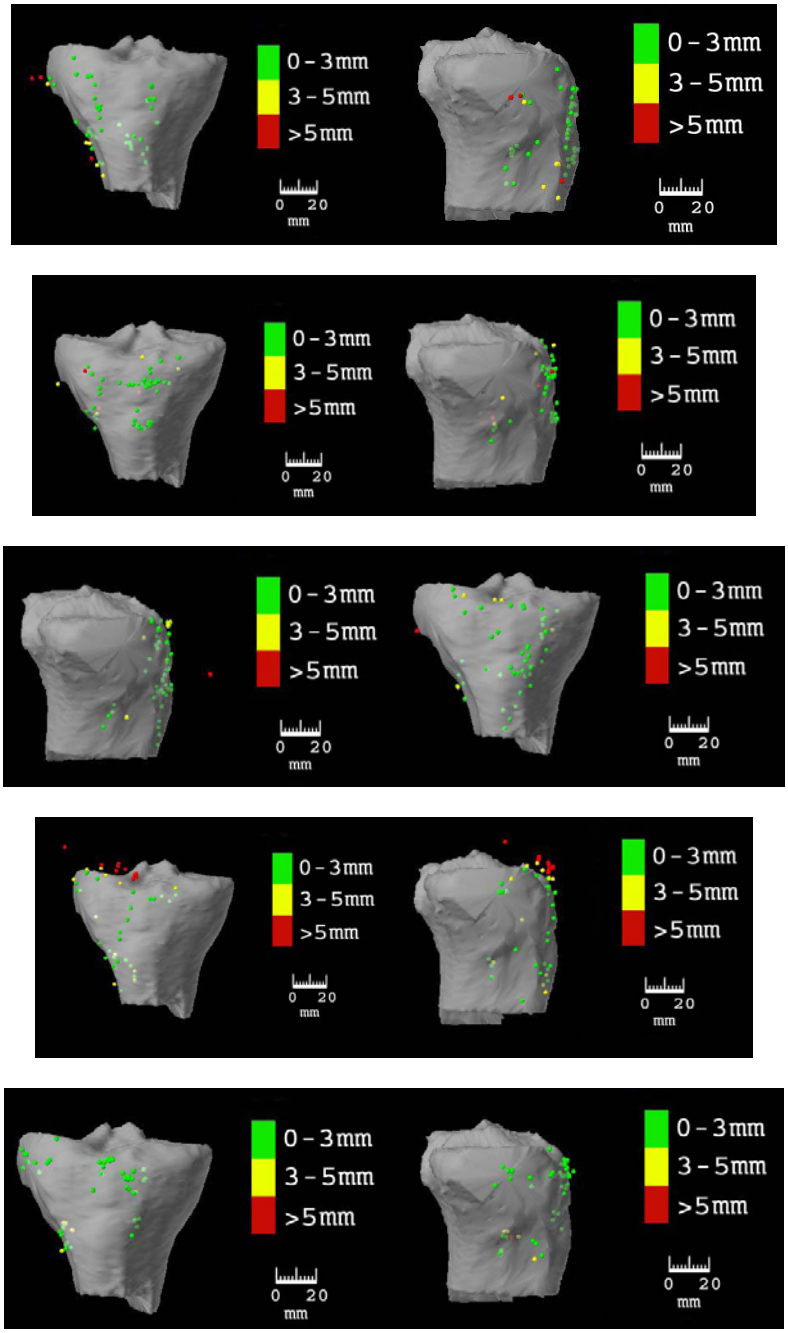


**Figure 5.33: Tibia registrations for specimen #2. a) registration #1, b) registration #2, c) registration #3, d) registration #4, e) registration #5. The tibia specimen segmented model is displayed with ultrasound data points from coronal and sagittal perspectives. The points are transformed using the ground truth registration from the standard registration approach. The distance of the point from the model shows the quality of the ultrasound capture approach. Data points less than 3 mm away are shown in green, points that are between 3 and 5 mm away are shown in yellow, and points that are greater than 5 mm away are shown in red.**

5.4.1.5 Third Specimen Results Compared to Standard Method

The results for the third specimen improve upon the first two specimens (Table 5.7). The RMS error values are 0.76 mm for the tibia and 0.93 mm for the femur. The femur registrations for the third specimen restricted data collection to the epicondyles where there is minimal tissue. The tibia model differed from previous specimens in that the fibula was included in the segmentation. Any points collected on the fibula were mapped to the model instead of generating noisy points for the registration algorithm. The data in Table 5.7 and Figures 5.34 and 5.35 show the results of the new methods.

**Table 5.7: Registration results for specimen #3 compared to standard registration with mechanical probe. The error is derived from a decomposed matrix that applies the inverse of the standard registration result with the ultrasound registration results. The table is broken down into errors for a) translation for femur, b) rotation for femur, c) translation for tibia, and d) rotation for tibia for each axis.**

**a)**

| Femur Specimen #3 | X translation error (Medial-Lateral) (mm) | Y translation error (Anterior-Posterior) (mm) | Z translation error (Superior-Inferior) (mm) |
|---|---|---|---|
| Registration #1 | 5.74 | 2.17 | 6.38 |
| Registration #2 | 0.03 | 0.99 | 5.50 |
| Registration #3 | 2.33 | 0.31 | 0.50 |
| Registration #4 | 4.16 | 0.12 | 7.15 |
| Registration #5 | 3.55 | 4.45 | 3.51 |
| Mean | 3.16 | 1.59 | 4.61 |

**b)**

| Femur Specimen #3 | Rotation about X-axis (Medial-Lateral) (degrees) | Rotation about Y-axis (Anterior-Posterior) (degrees) | Rotation about Z-axis (Superior-Inferior) (degrees) |
|---|---|---|---|
| Registration #1 | 0.09 | 2.46 | 6.45 |
| Registration #2 | 0.44 | 0.12 | 0.58 |
| Registration #3 | 0.20 | 0.46 | 1.48 |
| Registration #4 | 1.00 | 1.25 | 4.70 |
| Registration #5 | 0.55 | 1.10 | 3.86 |
| Mean | 0.46 | 1.07 | 3.41 |

**c)**

| Tibia Specimen #3 | X translation error (Medial-Lateral) (mm) | Y translation error (Anterior-Posterior) (mm) | Z translation error (Superior-Inferior) (mm) |
|---|---|---|---|
| Registration #1 | 2.41 | 1.76 | 1.84 |
| Registration #2 | 2.78 | 1.31 | 2.11 |
| Registration #3 | 0.31 | 0.43 | 3.53 |
| Registration #4 | 0.73 | 1.96 | 1.25 |
| Registration #5 | 0.65 | 1.26 | 1.98 |
| Mean | 1.38 | 1.34 | 2.14 |

**d)**

| Tibia Specimen #3 | Rotation about X-axis (Medial-Lateral) (degrees) | Rotation about Y-axis (Anterior-Posterior) (degrees) | Rotation about Z-axis (Superior-Inferior) (degrees) |
|---|---|---|---|
| Registration #1 | 1.28 | 0.25 | 2.56 |
| Registration #2 | 0.56 | 0.39 | 1.08 |
| Registration #3 | 0.03 | 0.05 | 3.42 |
| Registration #4 | 0.29 | 0.12 | 3.82 |
| Registration #5 | 0.55 | 0.20 | 2.82 |
| Mean | 0.54 | 0.20 | 2.74 |

a)

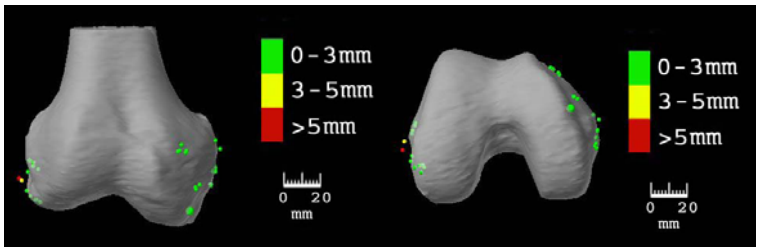


b)

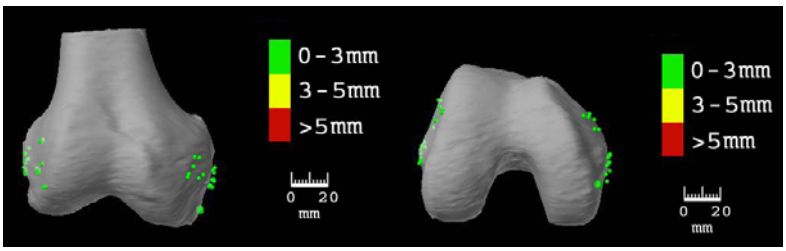


c)

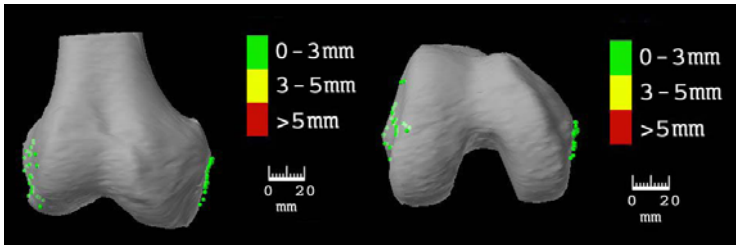


d)

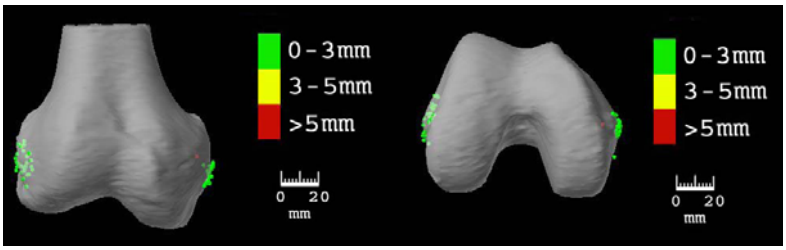


e)

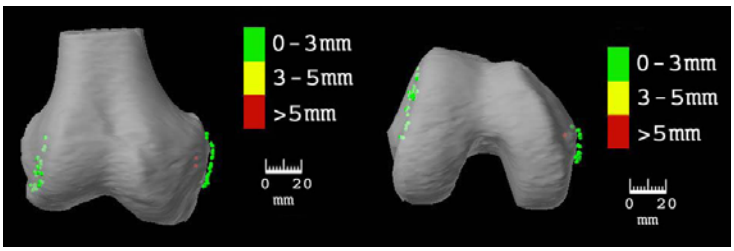


**Figure 5.34 Femur registrations for specimen #3. a) registration #1, b) registration #2, c) registration #3, d) registration #4, e) registration #5. The femur specimen segmented model is displayed with ultrasound data points from coronal and transverse perspectives. The points are transformed using the ground truth registration from the standard registration approach. The distance of the point from the model shows the quality of the ultrasound capture approach. Data points less than 3 mm away are shown in green, points that are between 3 and 5 mm away are shown in yellow, and points that are greater than 5 mm away are shown in red.**

a)

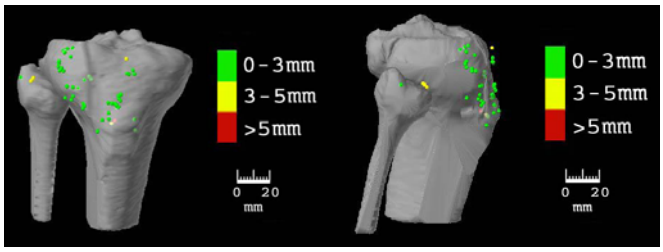


b)

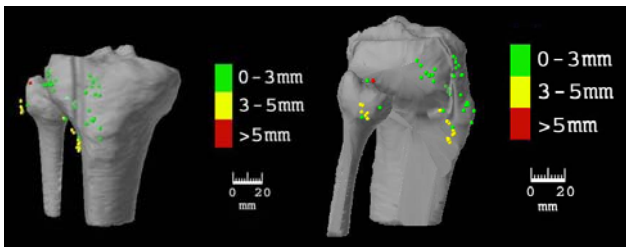


c)

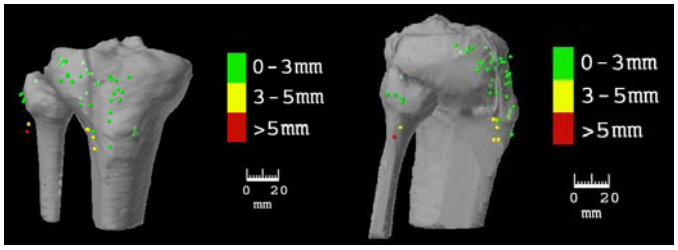


d)

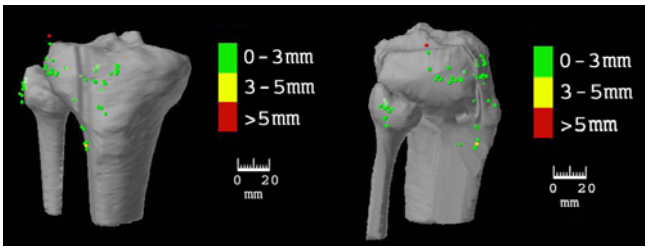


e)

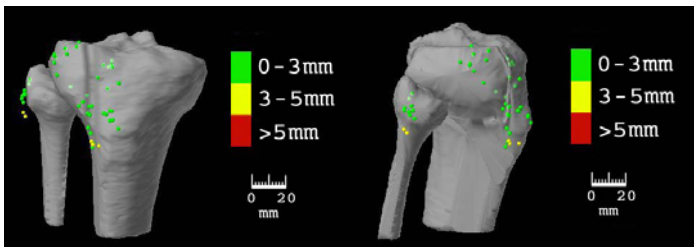


**Figure 5.35 Tibia registrations for specimen #3. a) registration #1, b) registration #2, c) registration #3, d) registration #4, e) registration #5. The tibia specimen segmented model is displayed with ultrasound data points from coronal and sagittal perspectives. It also includes a segmented fibula. The points are transformed using the ground truth registration from the standard registration approach. The distance of the point from the model shows the quality of the ultrasound capture approach. Data points less than 3 mm away are shown in green, points that are between 3 and 5 mm away are shown in yellow, and points that are greater than 5 mm away are shown in red.**

# Chapter 6: Discussion

## 6.1 Calibration

The calibration with the best RMS error and condition number was chosen for use in the experiments. Tables 5.1 and 5.2 show results for the five calibrations. The RMS is based on an error determined by finding the distance from the sample points to the surface after the points are transformed using the resulting calibration. The condition number is a measure of the spread of the data. Both values are critical in choosing the best calibration. It would be possible to have a very low RMS value if many of the points were captured in one spot, yet the resulting calibration could be quite poor. The condition number exposes whether the quality of the data set is sufficient. Calibration #1 had the best combination of RMS and condition number. The resulting offset for calibration #1 was (-28.10 1.72 -201.47) and so that was used for the remainder of the experiments.

## 6.2 Phantom Registration

The results displayed in figures 5.6 and 5.7 indicate that the data points for the first phantom registration seem to be floating off of the surface of the image model. The error sources could be a faulty calibration or an imprecise speed-of-sound constant. Since the calibration results from section 5.1 indicate that the chosen calibration is accurate, the most likely error is the speed-of-sound constant. Normally, a speed-of-sound of 1450 m/s is assumed in distilled water. However, the environment for the

experiment is not precisely matched to the conditions under which the theoretical constant was determined.

With the points floating off the surface of the model, the implication is that the speed-of-sound constant is too low and that the ultrasound beam is actually travelling faster than expected. For the second phantom registration, a speed-of-sound constant of 1540 m/s was used to more closely match the warmer non-distilled water in the water bath. The results show an improvement in the quality of the ultrasound data (Figs. 5.6-5.9). The significance of the difference is highlighted by the ANOVA graphs in Figure 6.1.

**Figure 6.1: The difference between the first phantom registration and second phantom registration were significant for both a) femur ($p<0.001$) and b) tibia ($p<0.001$). The first phantom results are displayed in column 1 and the second in column 2. The most significant variable between the first and second registrations was the speed-of-sound constant. For the first registration, the constant was set to 1450 m/s, for the second it was set to 1540 m/s. The ANOVA graphs show the mean of the each data set as the red line in the center of the box, the first and third quartiles are the upper and lower extent of the box, and the red crosses are outliers.**

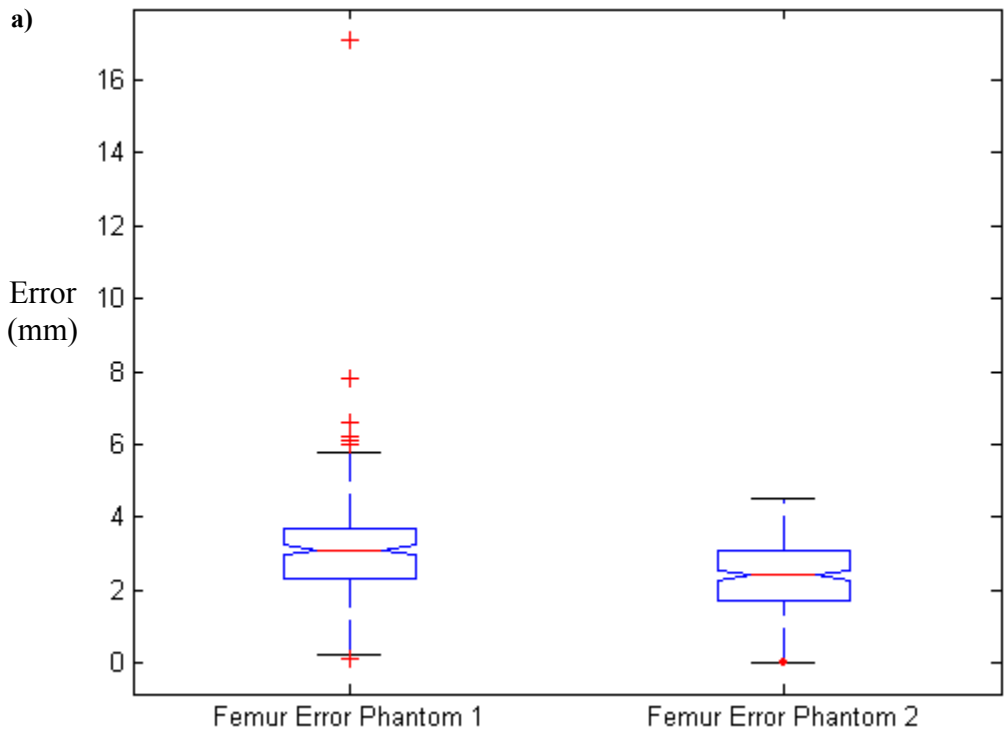

**b)**

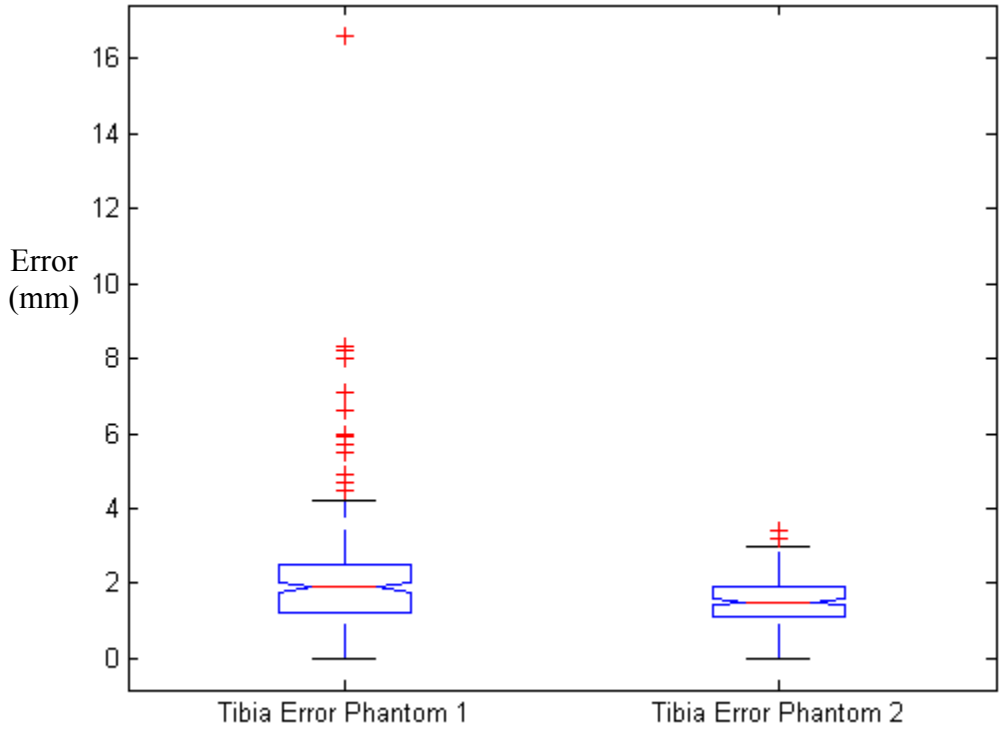


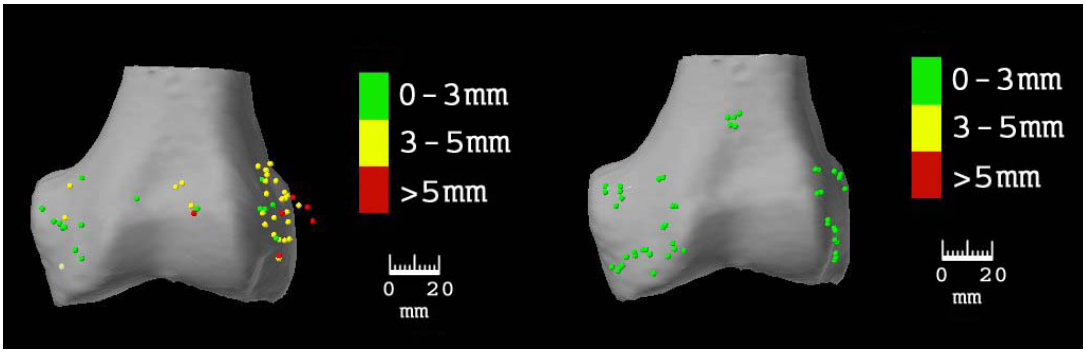


**Figure 6.2: A side-by-side comparison of samples from the first phantom registration (left) and the second phantom registration (right). The points are clearly closer to the surface on the second registration. The change in speed-of-sound constant had a positive effect. Unfortunately, the speed-of-sound constant for water does not affect the specimen registrations, which are based on a speed-of-sound constant that averages the speeds-of-sound through various tissue types.**

## 6.3 Specimen Registration

. Various aspects of data collection improvement were tested including: standoff selection, signal processing details, length of scan, and anatomical patterns for collecting data. The standoff options were between a water-filled glove finger, an Aquaflex gel pad, and scanning with no standoff. The signal processing filters incorporated different cutoff frequencies, including 0.004, 0.01, and 0.03. Variations in the length of the CT scan also affected the specimen registrations and analysis shows that the effects were significant. The patterns for both bones were altered over the course of the experiments. The femur data collection was limited to the epicondyles on the third specimen, whereas the first two specimens did not have any restriction. The tibia model for the third specimen included the fibula, which aided in constraining the rotation as explained in later sections.

### 6.3.1 Standoff Results

An attempt was made to directly measure the bone without any standoff, but the position of the target bone in the near-field of the transducer made it impossible to accurately determine the distance of the bone. An AquaFlex pad was used since it could be commonly found in ultrasound practices. However, the pad did not stand up to extended use and could degrade if registration takes a long time. Also, it was more difficult to guarantee a good signal since the pad was more cumbersome to use. The most effective standoff was a simple glove finger that was cut away from the glove and filled with water. This was an easy-to-use approach that resulted in consistently clean signals. While it provides a cheap disposable option, this could raise sterility issues in a

clinical setting. The errors that resulted from the use of the Aquaflex pad are significant (Fig. 6.3).

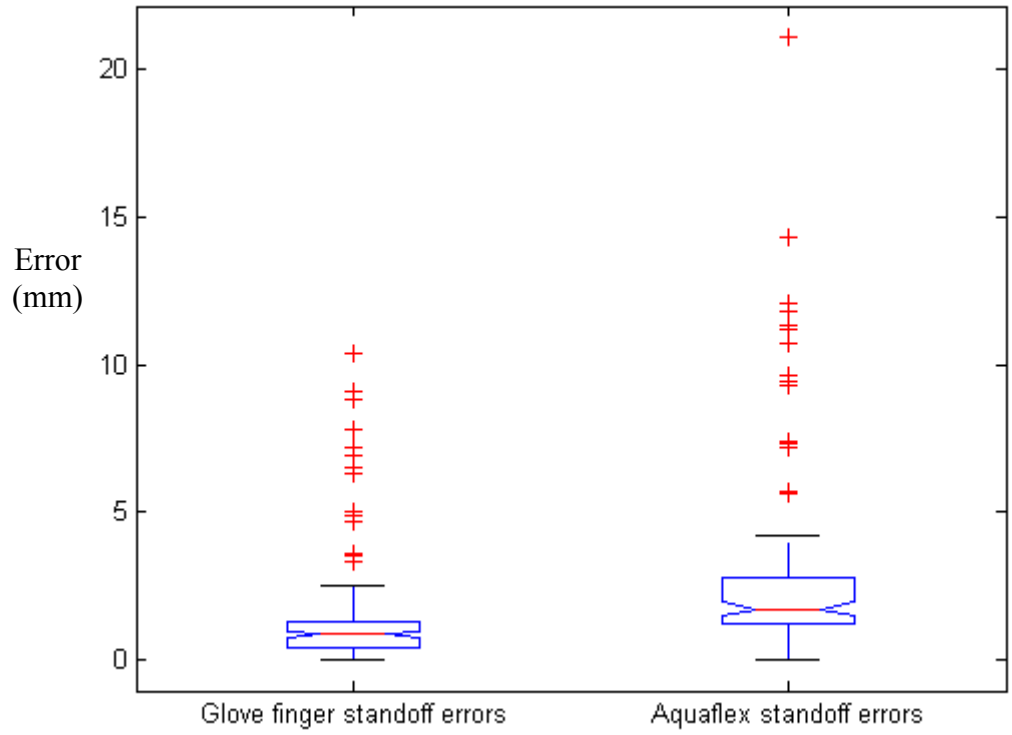


**Figure 6.3: The registration errors using the glove finger standoff were significantly better than the errors from the registrations using an Aquaflex gel pad for a standoff ($p<0.001$).**

### 6.3.2 Processing Filter Results

Of the various filters that were applied for smoothing, a low-pass Butterworth filter of order two and cutoff frequency of 0.01 yielded the most consistently clean signal. The constants for the filter were calculated in Matlab and hard-coded into the software. For the threshold filter, a value of 1.5x the average signal value resulted in the fewest false positives and false negatives. The filters were tested on a data set of ten signals that have a detectable bone signal and ten signals that should be rejected as lacking a

significant bone signal. The results from the test are displayed in Table 6.1. The cutoff frequency of 0.01 allowed for the best detection of a bone signal if one was present. Its low false-negative rate implies that it will yield a faster registration if a proper technique for collecting data is used. It also had the highest false-positive rate, and this implies that the results may be noisier since it is incorrectly categorizing signals. Since speed of registration is a critical component for any method, and since the false-positive rate was still within reason given the signal data set, the cutoff frequency of 0.01 was chosen for the low-pass filter.

**Table 6.1 A comparison of the detection rates of the three low-pass filters that varied by cutoff frequency. A high false-negative rate means that many signals were unnecessarily rejected. A high false-positive rate means that many signals were improperly categorized as bone signals though they should have been rejected. There are trade-offs associated with the errors of false-positive and false-negative signal analysis. Accepting a filter scheme that leans towards more false positives may lead to a faster registration, and a scheme that has a higher false-negative rate may be more robust.**

| Low-Pass Filters | False-Negative Rate | False-Positive Rate |
|---|---|---|
| Cutoff Frequency = 0.004 | 60% | 10% |
| Cutoff Frequency = 0.01 | 10% | 50% |
| Cutoff Frequency = 0.03 | 50% | 10% |

### 6.3.3 CT Scan length

The CT scan length changed for each of the three specimens (Fig. 6.4). The first specimen was scanned with a significantly longer setting so data could be captured further proximal on the femur and more distal on the tibia. The result was that the software application was prohibitively slow. The benefit of having more area on the

physical bone that can be accessed for data to match to the image space model is not worth the downside of slowing down the procedure. The scan for the second specimen was significantly shorter than the first, and data points can be seen captured close to the edge of the model. If data points captured on the physical bone do not correspond to the image space model, they will contribute error to the registration routine. Some of the registrations for the second specimen suffered from this problem as data points can be seen floating proximal of the femur model (Fig. 5.23a). The scan for the third specimen provided a reasonable image model without slowing down the software application significantly.

**a)**

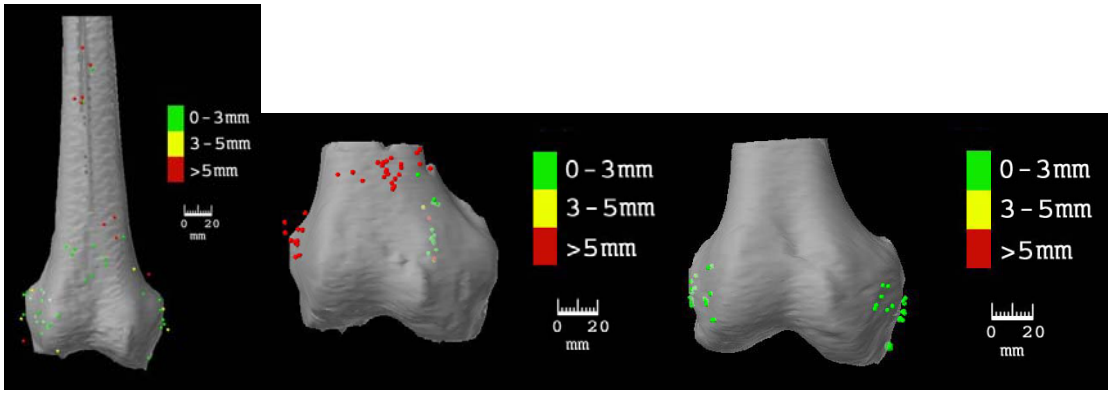


**b)**

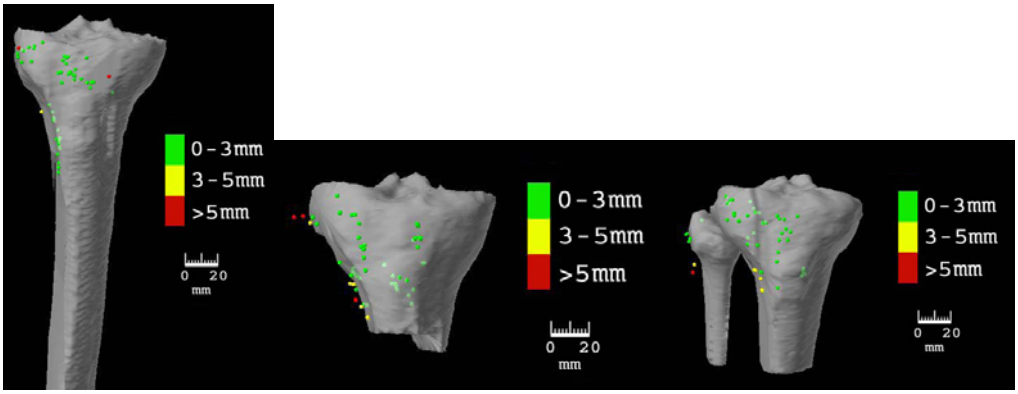


**Figure 6.4 The CT scan length varied for each of the three specimens. a) Femur models for the first specimen (left), second specimen (middle), and third specimen (right). b) Tibia models for the first specimen (left), second specimen (middle), and third specimen (right). Data points on the first specimen can be seen father along the scan (proximal for the femur, distal for the tibia) than in the other specimens. On the second specimen, data points can be seen dangerously close to the edge of the bone model. Points that are captured on the physical bone that are not on the image space bone model will add error to the registration. The third specimen scan is not as long as the first, but none of the data points are too close to the edge of the model.**

### 6.3.4 Accessibility Results

An interpretation of the registration results can highlight which data points are accurate and which are poorly captured (Figs. 5.21, 5.22, 5.23, 5.24, 5.25, 5.26). This view is created by applying the standard registration transform, as determined by the mechanical probe registration, to the ultrasound data points and displaying them on the

bone model. The femur and tibia have unique anatomical features and so have different accessibility restrictions.

The images for the tibias show that the tibia points are mostly embedded on the image space bone. This indicates that the points are accurately collected and only the pattern needs to be improved to better register the tibia. One exception to this was detected on the second specimen results. One resulting image of the tibia from the second specimen showed that points captured on the lateral side of the tibia were floating off of the bone model (Fig. 6.5).

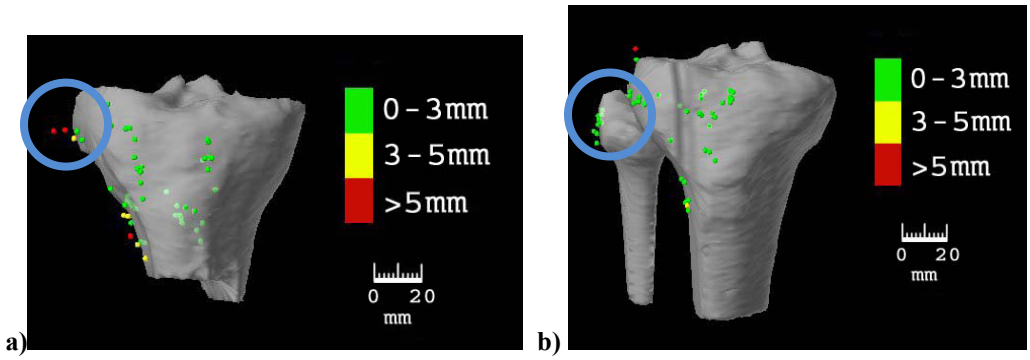


**Figure 6.5: Difference between models with and without fibula. a) A tibia registration from the second specimen shows red points on the superior lateral side shown in the blue circle. These points were likely captured on the fibula. The fibula is accessible to ultrasound and not to a standard approach. b) Including the fibula in the third specimen segmentation leverages this advantage.**

In contrast with the tibia registrations, the femur images show that many points are not accurately captured. The reason could be due to excessive noise. Noise can be generated by inhomogeneous tissue. Noise can also result if the ultrasound transducer is not perpendicular to the face of the bone. Theoretically, while the patella obscures the patellar groove on the femur, the tissue superior of the patella should not obscure the underlying bone from ultrasound. The resulting images (Figs. 5.21, 5.23, 6.6, 6.7) underscore that, in practice, the data points on the anterior of the femur are not easily captured. This disproved the hypothetical description of which areas were accessible on

the femur (Fig 4.7). By restricting data capture to the epicondyles of the femur, the ultrasound capture error was significantly reduced (Fig. 6.7).

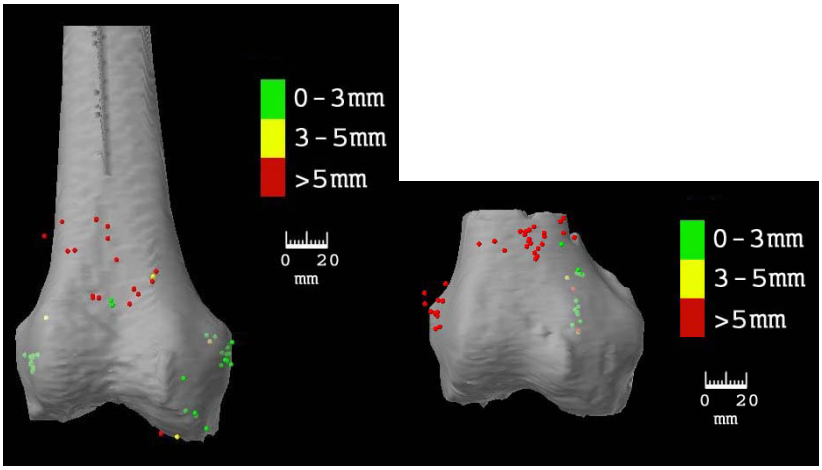


**Figure 6.6 Results from first two femur registrations show errors . Results from femur registrations from the first specimen (left) and second specimen (right) show data points with significant error displayed in red on the anterior of the femur. These imply that significant noise from thicker tissue on the anterior may interfere with accurate ultrasound data collection.**

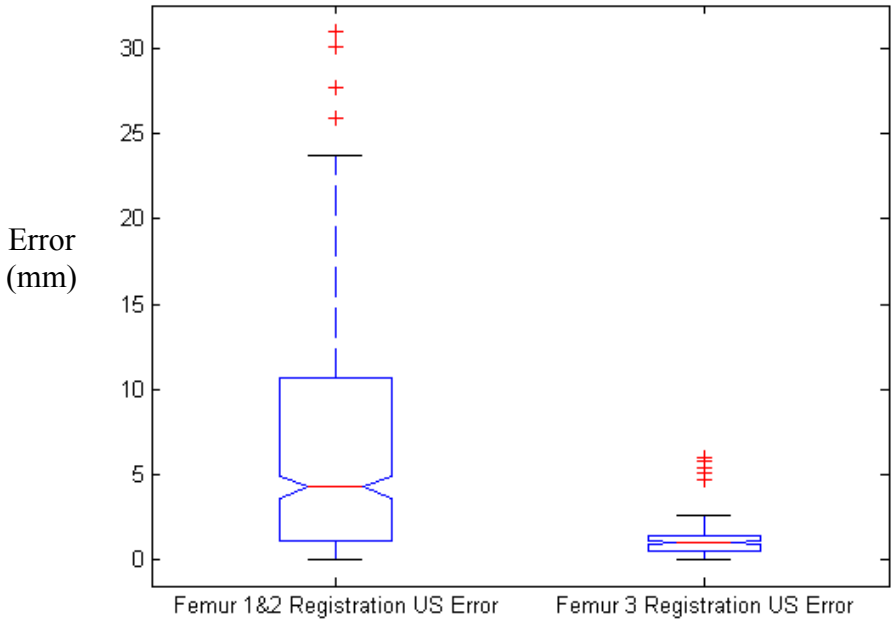


**Figure 6.7 The ANOVA graph compares the errors of the ultrasound data points from the femur registrations from the first two specimens with the ultrasound data from the registrations of the third femur specimen. Registrations from the femurs of the first two specimens had no restrictions for which areas could be used for data capture. The data capture from the third specimen was limited to the epicondyles of the femur. It demonstrates that restricting the ultrasound data capture to the epicondyles of the femur greatly reduced the error ($p<0.001$).**

### 6.3.5 Specimen Results Compared to Standard Method

The ultrasound registrations were compared to a standard registration technique that involves capturing data directly on the bone with a mechanical probe. The transform that is determined by the standard registration is inversed and applied to the ultrasound registration transform. This calculation yields a transform that can be decomposed into translation and rotation errors.

#### 6.3.5.1 Femur Registration Results Compared to Standard Method

Results from the femur registrations showed that the first two femur specimens could not be registered with enough accuracy to be clinically relevant. After analyzing the captured ultrasound data, the images indicated that noisy points were preventing a successful registration. For the third specimen, restricting ultrasound capture to the epicondyles resulted in more accurate data samples (Fig. 6.7). The resulting registrations of the third specimen compared more favorably to the standard registration results (Fig. 6.8). While the results of the third specimen do not guarantee a robust registration, some of the registrations show that accurate ultrasound registration of the femur is at least possible (Table 6.2).

**a)**

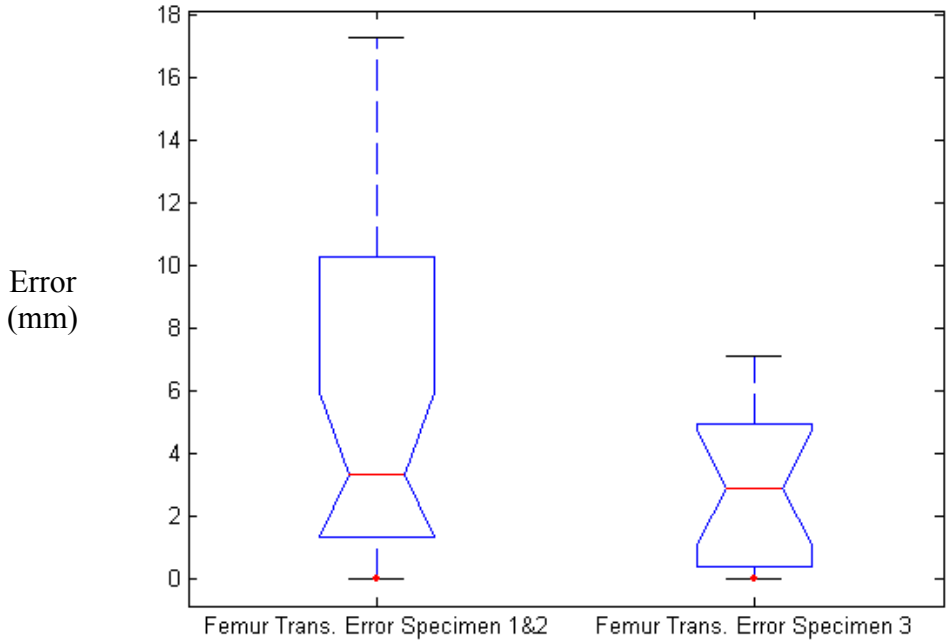


**b)**

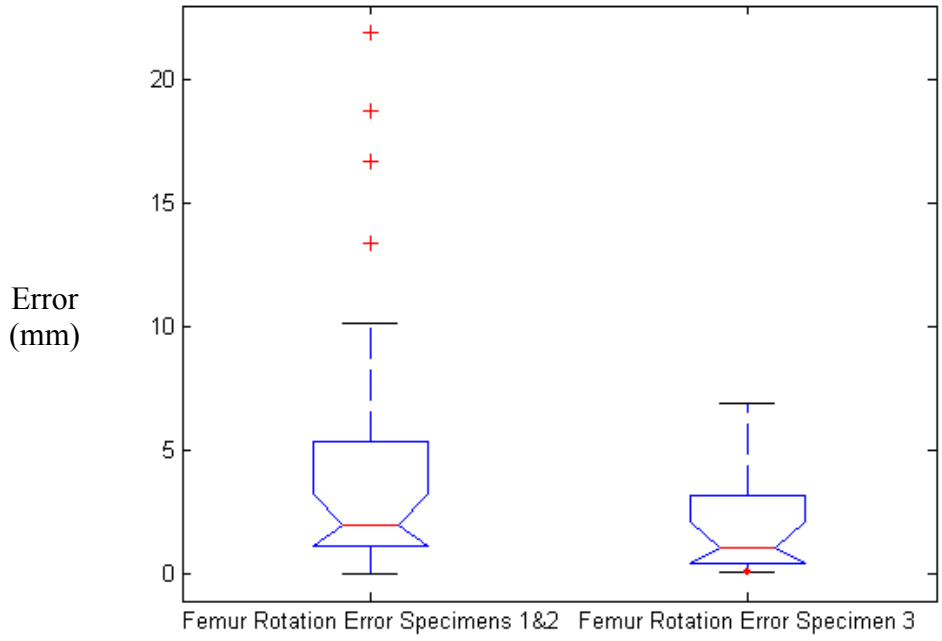


**Figure 6.8: Comparison of the decomposed a) translation ($p<0.05$) and b) rotation ($p<0.10$) registration results of the first two specimens with the decomposed results of the third specimen. The results show that the femur registrations improved with the technique for the third specimen. However, the error values are still slightly higher than what would be clinically acceptable.**

**Table 6.2 The second registration from the third femur specimen proved that a clinically accurate registration is achievable. The results show that the decomposed error relative to the standard registration method can be within the clinically acceptable error range of 3mm of translation and 3 degrees of rotation.**

| Registration #2 Femur Specimen #3 | X-axis | Y-axis | Z-axis |
|---|---|---|---|
| Translation Error | 2.33 | 0.31 | 0.50 |
| Rotation Error | 0.20 | 0.46 | 1.48 |

6.3.5.2 Tibia Registration Results Compared to Standard Method

Results from ultrasound tibia registrations indicate that an ultrasound approach may be accurate and robust (Tables 5.5, 5.6, 5.7). The mean of the decomposed errors for translation and rotation from the third specimen are within a 3mm translation and 3 degree rotation threshold. The errors for the Z-axis rotation is the most significant component of the decomposed error transform. The registration from the third specimen improved on the Z-axis rotation error (Table 5.7). The addition of the fibula to the segmentation of the third specimen's tibia aided in constraining the Z-axis rotation error (Figure 6.9).

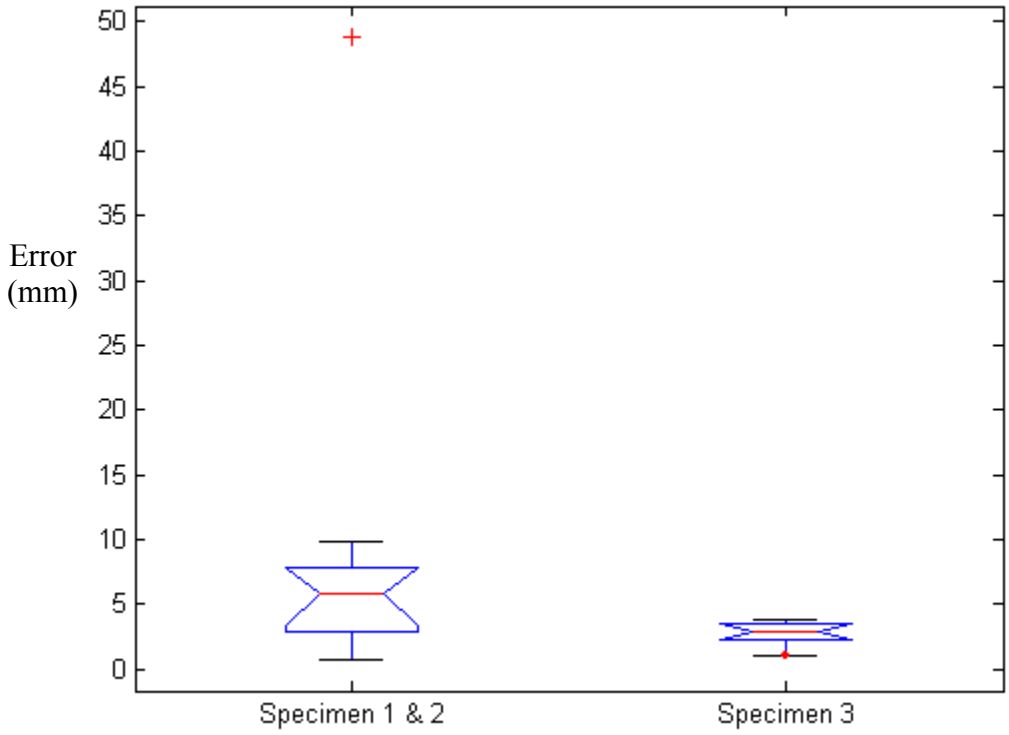


**Figure 6.9: The Z-axis rotation error from the tibia ultrasound registrations as compared to the standard method. The error from the third specimen has an improved mean and variance. The lower significance (p>0.3) could be due to a small sample set of 5 registrations for the third specimen.**

While the registration error is approximately 3mm worse than the standard method, the technique shows considerable improvement over the mechanical probe registration of the tibia due to advantages unrelated to accuracy. One key feature on the tibia is the tubercle. Since extra incisions are required to access the tibia tubercle for the mechanical probe approach, it is especially invasive. Ultrasound, on the other hand, can access the tubercle without any incision. Speed is also improved since a physician's assistant can perform much of the work in this registration approach, whereas a surgeon is required to perform the standard approach since an incision is made.

## 6.4 Future Work

### 6.4.1 Hybrid Approach

Preliminary results indicate that the ultrasound femur approach may not be robuts enough to be clinically acceptable. If the ultrasound data capture is limited to the epicondyles, the registration may need additional constraining features to guarantee an accurate registration. A hybrid approach that combines a few carefully selected points by the mechanical probe with the ultrasound point collection could yield a more accurate registration than ultrasound alone. This hybrid approach could be accomplished with a smaller incision than is normally required for one that uses the mechanical probe exclusively. This is similar to the approach that has been used for total hip arthroplasty (THA) [36]. Since an incision is still necessary for the procedure, this approach would not compromise the benefits of the A-mode approach. Preliminary tests were performed with a hybrid approach. The hybrid points did not seem to improve the registration, but it was determined that poor ultrasound data quality was the primary source of the error. With accurate ultrasound data, gathering data from obscured areas using a mechanical probe may improve the registration.

### 6.4.2 Optimizing on the Speed-of-Sound Constant

The phantom registrations demonstrated that a change in the speed-of-sound properties can greatly affect the quality of the ultrasound data capture. Speed-of-sound properties in human specimens have high variability depending on the quantity of skin, fat and muscle between the surface and the bone. It is possible to include the speed-of-sound constant as a parameter into the ICP-based registration routine. By incorporating

the speed-of-sound constant, each registration can account for data that is captured on a patient with thicker or thinner tissue. The current speed-of-sound constant of 1540 m/s assumes a consistent distribution of human tissue that matches the conditions under which the constant was determined. Since tissue can vary greatly between patients, accounting for it in the optimization routine may improve the robustness of the ultrasound approach.

### 6.4.3 Comparison to Acustar gold standard

In addtion to comparing the ultrasound approach to the standard mechanical probe approach, the evaluation would be improved by also comparing to a gold standard fiducial-based registration using Acustar fiducials. The fiducials are radiopaque markers placed in the bone before the CT scan is taken. The markers are selected in image space and determine a set of points. Then the radiopaque caps are replaced with caps that can be mated with an acustar probe to a high degree of accuracy (Fig. 6.10) [5, 13]. The tracked Acustar probe can select points in physical space and an accurate point-pair matching can be established. This matching has even greater accuracy than the surface match using the mechanical probes. Since the surface match approach has an error in the 1-2mm range, the results of an A-mode ultrasound approach may actually be better than what has been experimentally determined. An Acustar fiducial registration may help to accurately determine the error.

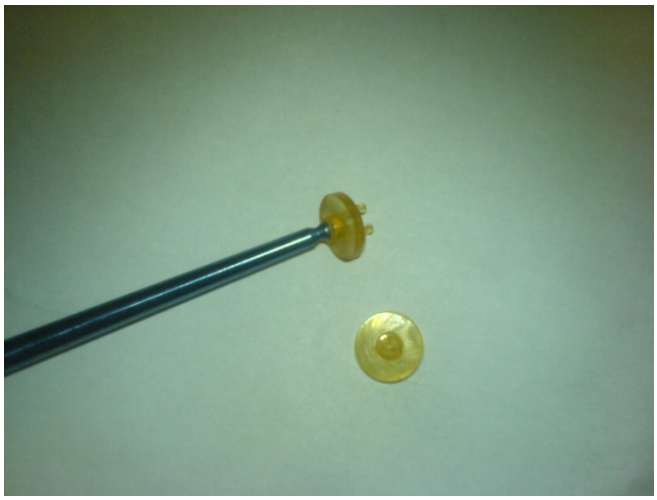

**Figure 6.10: Acustar probe sitting in the acustar fiducial cap. This provides a fiducial-based approach to registration that can improve the results of the gold standard reference that is used in these experiments. A better reference will result in a more accurate evaluation of the ultrasound approach.**

### 6.4.4 Optical Flow

The signal processing is a key part of the A-mode ultrasound registration approach. The filtering is predominantly spatial based filtering, meaning it searches through a single signal for the position of the bone surface. The only temporal filtering in the current scheme is a consistency filter that ensures the points are not taken in error. However, temporal filtering may also be used to predict where the bone is in successive signals.

Optical flow is an image processing analysis scheme that uses temporal filtering to predict motion. If only spatial filtering is used, each signal must contain a significant peak to confidently declare the bone surface position. With optical flow, it may be possible to use a successfully filtered signal as a key frame for future signals. Future signals may be processed with a more lenient threshold for the spatial filter if it is combined with a prediction for the location of the bone surface based on a previous key frame.

The disadvantage to optical flow is that it assumes a consistency from one signal to the next. Unfortunately, noisy ultrasound signals are typical due to the inhomogeneity of human tissue. This may invalidate the assumption on which optical flow is based. It may be the case, however, that the ultrasound signals, while not perfectly consistent, are still close enough for a modified optical flow routine to work.

## Chapter 7: Conclusions

A-mode ultrasound registration provides clinically useful accuracy for surgical navigation in robot-assisted knee replacement. A calibration procedure was developed that can be used to easily determine the offset of the ultrasound beam to the affixed tracker. The tibia and femur are easily and quickly registered using an A-mode approach that takes advantage of automated signal processing. This approach eliminates the need for a larger incision for access for registration. Once clinical accuracy is achieved, the only limiting factor remaining for computer-assisted robot-assisted knee replacement is the size of the implants.

The high variability and relatively low sample size made some of the analysis less conclusive although trends are clear. One unquantifiable difference between the specimens is the quality of the cadaver tissue. Some specimens had very little tissue or more degraded tissue than others. This affects the quality of the ultrasound data that is captured as well as the final resulting registrations. With continued testing, a greater sample size could prove that the ultrasound approach for the tibia including the fibula is robust. It could also prove that an ultrasound approach for the femur that is restricted to the epicondyles is robust and accurate.

Overall, these registration results were in line with other researchers' results in cranial applications of A-mode ultrasound registration [50, 58]. Maurer et al indicated that their ex vivo results would imply that an upper limit of 3mm for a TRE could be expected in vivo [50] and that would be clinically acceptable. The tibia results were in a clinically acceptable range and the femur results were close. Slight improvements may reduce the error so a robust and accurate A-mode registration method can be used

clinically. As Popovic et al concluded, robustness is key to bridging the method from occasional research successes to clinical practice, and some areas for improvement include signal processing and help with transducer alignment [58]. There are a few schemes that might improve the results.

**REFERENCES**:

[1] Akiyama, H., Kawanabe, K., Goto, K., Ohnishi, E., Nakamura, T. "Computer-Assisted Fluoroscopic Navigation System for Removal of Distal Femoral Bone Cement in Revision Total Hip Arthroplasty." The Journal of Arthroplasty, Vol. 22, No. 3, pp. 445-448, 2007.

[2] Amin, D., Kanade, T., DiGioia, A., Jaramaz, B. "Ultrasound Registration of the Bone Surface for Surgical Navigation." Computer Aided Surgery Vol. 8, pp. 1-16, 2003.

[3] Amstutz, C., Caversaccio, M., Kowal, J., Bachler, R., Nolte, L.P., Hausler, R., Styner, M. "A-Mode Ultrasound-Based Registration in Computer-Aided Surgery of the Skull." Otolaryngology Head & Neck Surgery, Vol. 129, No. 12, pp. 1310-1316, Dec 2003.

[4] Barratt, D.C., Penney, G., Chan, C.S.K., Slomczykowski, M., Carter, T.J., Edwards, P.J., Hawkes, D.J. "Self-Calibrating Ultrasound-to-CT Bone Registration." MICCAI 2005, LNCS 3749, Springer Publishing, pp. 605 – 612, 2005.

[5] Barratt, D.C., Penney, G.P., Chan, C.S.K., Slomczykowski, M., Carter, T.J., Edwards, P.J., Hawkes, D.J. "Self-Calibrating 3D-Ultrasound-Based Bone Registration for Minimally Invasive Orthopedic Surgery." IEEE Transactions on Medical Imaging, Vol. 25, No. 3, pp. 312-323, March 2006.

[6] Barrett, A.R.W., Cobb, J.P., Rodriguez y Baena, F.M., Jakopec, M., Gomes, P., Harris, S.J., Davies, B.L. "Minimally-Invasive Computer-Assisted Hip Resurfacing Surgery Using The Acrobot Navigation System." Journal of Bone and Joint Surgery British Volume, Vol. 88-B, No. 3, p. 441, 2006.

[7] Barrett, A.R.W., Davies, B.L., Gomes, M.P.S.F., Harris, S.J., Henckel, J., Jakopec, M., Rodriguez y Baena, F.M., Cobb, J.P. "Preoperative Planning and Intraoperative Guidance for Accurate Computer-Assisted Minimally Invasive Hip Resurfacing Surgery." Proceedings of the Institution of Mechanical Engineers, Part H: Journal of Engineering in Medicine, Vol. 220, No. 7, pp. 759-773, 2006.

[8] Bass, W.A. "Patient-Image Registration Using A-Mode Ultrasound Localization of Features." Ph.D. Dissertation, Vanderbilt University, Nashville Tennessee, May 2003.

[9] Besl P., McKay N.D., "A Method for Registration of 3D Shapes." IEEE Transactions on Pattern Analysis and Machine Intelligence, Vol. 14, pp. 239 – 256, 1992.

[10] Blanchet, E., Lucchini, J.P., Jenny, R., Fortin, T. "An Image-Guided System Based on Custom Templates: Case Reports." Clinical Implant Dental Related Research, Vol. 6, pp. 40-47, 2004 .

[11] Borner, M., Bauer, A., Lahmer, A. "Computer-Guided Robot-Assisted Hip Endoprosthesis." Orthopade, Vol. 26, pp. 251-257, 1997.

[12] Brendel, B., Winter, S., Rick, A., Stockheim, M., Ermert, H. "Registration of 3D CT and Ultrasound Datasets of the Spine using Bone Structures." Computer Aided Surgery Vol. 7, pp. 146-155, 2002.

[13] Brendel, B., Winter, S., Rick, A., Stockheim, M., Ermert, H. "Bone Registration with 3D CT and Ultrasound Data Sets." International Congress Series 1256, pp. 426–432, 2003.

[14] Burkey, B., Speyer, M., Maciunas, R., Fitzpatrick, J.M., Galloway, R., Allen, G. "Sublabial, Transseptal, Transsphenoidal Approach to the Pituitary Region Guided by the ACUSTAR I System." Otolaryngology Head & Neck Surgery, Vol. 118, No. 2, pp. 191-194, 1998.

[15] Chauhan, S., Mishra, R., Kumar, S., Teo, M.Y. "A Robot for Non-invasive Breast Cancer Surgery." Seventh International Conference on Control, Automation, Robotics, and Vision, pp. 425-428, December 2002.

[16] Davies, B., Starkie, S., Harris, S.J., Agterhuis, E., Paul, V., Auer, L.M. "Neurobot: A Special-Purpose Robot for Neurosurgery." Proceedings of the 2000 IEEE International Conference on Robotics & Automation, pp.4103-4108. San Francisco, CA April 2000.

[17] Decking, J., Theis, C., Achenbach, T., Roth, E., Nafe, B., Eckardt, A. "Robotic Total Knee Arthroplasty: The Accuracy of CT-Based Component Placement." Acta Orthop Scand. Vol. 75, pp. 573-579, 2004.

[18] Deokmien, C., Mildenstein, M., Hensel, K., Hold, S., Winter, S. "Registration of Intraoperative 3D Ultrasound with MR Data for the Navigated Computer Based Surgery." Advances in Medical Engineering, Vol. 114, pp. 252-257, 2007.

[19] Department of Orthopedics, University of Iowa. "Total Knee Replacement: A Patient Guide." Orthopedic Nursing Division, Department of Nursing, University of Iowa Hospitals and Clinics. December 1999.

[20] DiGioia, A., Jaramaz, B., Picard, F., Nolte, L.P. Computer and Robotic Assisted Knee and Hip Surgery. Oxford University Press. NY, NY. 2004.

[21] Dorr, L.D., Hishiki, Y., Wan, Z., Newton, D., Yun, A. "Development of Imageless Computer Navigation for Acetabular Component Position in Total Hip Replacement." The Iowa Orthopedic Journal, Vol. 25, pp. 1-9, 2005.

[22] Dumond, S. "UltrasoundTechnology for Small Animal Imaging." http://www.animallab.com/articles.asp?pid=209. ALN Magazine, November, 2006.

[23] Ewers R, Schicho K, Undt G, Wanschitz F, Truppe M, Seemann R, Wagner A. "Basic Research and 12 Years of Clinical Experience in Computer-Assisted Navigation

Technology: A Review." International Journal of Oral Maxillofacial Surgery, Vol. 34, pp. 1-8, 2005.

[24] Fitzpatrick, J.M., West, J.B., Maurer Jr., C.R. "Predicting Error in Rigid-body, Point-Based Registration." IEEE Transactions on Medical Imaging, Vol. 17, No. 5, pp. 694-702, 1998.

[25] Foley, K.T., Smith, M.M. "Image-Guided Spine Surgery." Neurosurg Clin N Am, Vol. 7, pp. 171-186, 1996.

[26] Freedman, K. B. **"**Partial Knee Replacement - Series: Procedure**."** http://www.nlm.nih.gov/medlineplus/ency/presentations/100225_1.htm, National Institute of Health, 2006.

[27] Frost and Sullivan. "Strategic Analysis Orthopedic Implant Markets." World Orthopedic, August 2003.

[28] Gauldie, D.R. "Calibration and Registration With 3D A-Mode Ultrasound." Master's Thesis, Queen's University, Kingston, Ontario, Canada, December 2002.

[29] Gong, J., Bachler, B., Sati, M., Nolte, L.P. "Restricted Surface Matching: A New Approach to Registration in Computer Assisted Surgery". LNCS, MRCAS 1997, pp. 597-605, 1997.

[30] Goss, S.A., Johnston, R.L., Dunn, F. "Compilation of Empirical Ultrasonic Properties of Mammalian Tissues." The Journal of the Acoustical Society of America, Vol. 68, No.1, pp. 93-108, 1980.

[31] Greenspan, M., Godin, G. "A Nearest Neighbor Method for Efficient ICP." Proceedings of the 3rd International Conference on 3-D Digital Imaging and Modeling, pp. 161-170, 2001.

[32] Guthrie, B.L., Adler Jr., J.R. "Computer-Assisted Preoperative Planning, Interactive Surgery, and Frameless Stereotaxy." Clinical Neurosurgery, Vol. 38, pp. 112-131, 1992.

[33] Hassfeld, S., Muhling, J. "Comparative Examination of the Accuracy of a Mechanical and an Optical System in CT and MRT Based Instrument Navigation." International Journal of Oral Maxillofacial Surgery, Vol. 29, pp. 400–407, 2000.

[34] Hearn, D., Baker, M., P. Computer Graphics. Chapter 3: 3D Transformations, Prentice Hall, Inc. Upper Saddle River, NJ. 1986.

[35] He, P., Zheng, J. "Segmentation of Tibia Bone in Ultrasound Images Using Active Shape Models." Proceedings of the 23rd Annual EMBS International Conference, pp. 2712-2715, Istanbul, Turkey, October 2001.

[36] Heger, S., Portheine, F., Ohnsorge, J.A.K., Schkommodau, E., Radermacher, K. "User-Interactive Registration of Bone with A-Mode Ultrasound." IEEE Engineering in Medicine and Biology Magazine, Vol. 24, No. 2, pp. 85-95, March 2005.

[37] Ionescu, G., Lavallee, S., Demongeot, J. "Automated Registration of Ultrasound with CT Images: Application to Computer Assisted Prostate Radiotherapy and Orthopedics." MICCAI 1999, LNCS 1679, pp. 768-778, 1999.

[38] Jaynes, C. "Two Camera Geometry: Stereo Vision Images." http://www.metaverselab.org/classes/635/lectures/published/004-StereoGeometry.pdf, University of Kentucky, 2002.

[39] Kendoff, D., Bogojevic, A., Citak, M., Maier, C., Maier, G., Krettek, C., Hufner, T. "Experimental Validation of Noninvasive Referencing in Navigated Procedures on Long Bones." Journal of Orthopaedic Research, Vol. 25, pp. 201-207, 2007.

[40] La Palombara, P.F., Fadda, M., Martelli, S., Marcacci, M. "Minimally Invasive 3D Data Registration in Computer and Robot Assisted Total Knee Arthroplasty." Medical and Biological Engineering and Computing, Vol. 35, pp. 600-610, 1997.

[41] Langlotz, F., Nolte, L.P. "Technical Approaches to Computer-Assisted Orthopedic Surgery." European Journal of Trauma, Vol. 30, No. 1, pp.1-11, 2004.

[42] Lee, T.C., Yang, L.C., Liliang, P.C., Su, T.M. "Single Versus Separate Registration for Computer-Assisted Lumbar Pedicle Screw Placement." Spine, Vol. 29, No. 14, pp. 1585-1589, 2004.

[43] Lourakis, M. "A Brief Description of the Levenberg-Marquardt Algorithm Implemented by levmar." Institute for Computer Science, Foundation for Research and Technology, Heraklion, Crete, Greece, February 2005.

[44] Luwig, G. "The Velocity of Sound through Tissues and the Acoustic Impedance of Tissues." The Journal of the Acoustical Society of America, Vol. 22, No. 6, pp. 862-866, 1950.

[45] Lyman, S., Sherman, S., Dunn, W.R., Marx, R.G. "Advancements in the Surgical and Alternative Treatment of Arthritis." Current Opinion on Rheumatology. Vol. 17, pp. 129-33, 2005.

[46] Ma, B., Ellis, R.E. "Robust Registration for Computer-Integrated Orthopedic Surgery: Laboratory Validation and Clinical Experience." Medical Image Analysis, Vol. 7, No. 3, pp. 237-250, 2003.

[47] Manninen, P., Riihimaki, H., Heliovaara, M., Suomalainen, O. "Physical Exercise and Risk of Severe Knee Osteoarthritis Requiring Arthroplasty." Rheumatology, Vol. 40, pp. 432-437, 2001.

[48] Maurer Jr., C.R., Aboutanos, G.B., Dawant, B.M., Maciunas, R.J., Fitzpatrick, J.M. "Registration of 3-D Images Using Weighted Geometrical Features." IEEE Transactions On Medical Imaging, Vol. 15, No. 6, pp. 836-849, 1996.

[49] Maurer Jr, C.R., Fitzpatrick, J.M., Wang, M.Y., Galloway, Jr R.L., Maciunas, R.J., Allen, G. "Registration of Head Volume Images Using Implantable Fiducial Markers." IEEE Transactions on Medical Imaging, Vol. 16, No. 4, pp. 447-462, August 1997.

[50] Maurer Jr, C.R., Gaston, R.P., Hill, D.L., Gleeson, M.J., Taylor, M.G., Fenlon, M.R., Edwards, P.J., Hawkes, D.J. "AcouStick: A Tracked A-Mode Ultrasonography System for Registration in Image-Guided Surgery." MICCAI 1999, LNCS 1679, pp. 953-963, 1999.

[51] Mercier, L., Lango, T., Lindseth, F., Collins, D.L. "A Review of Calibration Techniques for Freehand 3-D Ultrasound Systems." Ultrasound Medicine and Biology, Vol. 31, No. 4, pp. 449-471, 2005.

[52] Miga, M.I., Sinha, T.K., Cash, D.M., Galloway, R.L., Weil, R.J. "Cortical Surface Registration for Image-Guided Neurosurgery Using Laser-Range Scanning." IEEE Transactions on Medical Imaging, Vol. 22, No. 8, 2003.

[53] Nolte, L.P., Zamorano, L.J., Jiang, Z., Wang, Q., Langlotz, F., Berlemann, U. "Image-Guided Insertion of Transpedicular Screws: A Laboratory Set-Up." Spine Vol. 20, pp. 497-500, 1995.

[54] Novotny, P., Kettler, D.T., Jordan, P., Dupont, P.E., del Nido, P.J., Howe, R.D. "Stereo Display of 3D Ultrasound Images for Surgical Robot Guidance." Proceedings of the 28th IEEE EMBS Annual International Conference, NYC, USA, pp. 1509-1512, August 2006.

[55] Parmet, S., Lynm, C., Glass, R. "Osteoarthritis of the Knee." Journal of American Medical Association, Vol. 289, No. 8, p. 1068, 2003.

[56] Phee, L., Xiao, D., Yuen, J., Chan, C.F., Ho, H., Thng, C.H., Cheng, C., Ng, W.S. "Ultrasound Guided Robotic System for Transperineal Biopsy of the Prostate." Proceedings of the 2005 IEEE International Conference on Robotics and Automation, Barcelona, Spain, pp.1315-1320, April 2005.

[57] Poonguzhali, S., Ravindran, G. "A Complete Automatic Region Growing Method for Segmentation of Masses on Ultrasound Images." International Conference on Biomedical and Pharmaceutical Engineering, pp. 88-92, 2006.

[58] Popovic, A., Heger, S., Follmann, A., Wu, T., Engelhardt, M., Schmieder, K., Radermacher, K. "Efficient Non-Invasive Registration with A-mode Ultrasound in Skull Surgery." Proceedings of the 18th Conference on Computer Assisted Radiology and Surgery, International Congress Series, pp. 821-826, 2005.

[59] Prymka, M., Hassenpflug, J. "Dislocated Fracture of the Lesser Trochanter with Malrotation of the Stem After Robot Assisted Implantation of a Cementless Hip Prosthesis: A Casuistic Report." Unfallchirurg, Vol. 106, pp. 671-675, 2003.

[60] Rousseau, F., Hellier, P., Barillot, C. "A Fully Automatic Calibration Procedure For Freehand 3D Ultrasound." *IEEE International Symposium on Biomedical Imaging,* Washington, USA, pp. 985-988, July 2002.

[61] Rusinkiewicz, R., Levoy, M. "Efficient Variants of the ICP Algorithm." Third International Conference on 3D Digital Imaging and Modeling, Quebec City, Canada, 2001.

[62] Russakoff, D., Rohlfing, T., Adler, J., Maurer Jr., C.R. "Intensity-Based 2D-3D Spine Image Registration Incorporating a Single Fiducial Marker." Academic Radiology Vol. 12, No.1, pp. 37-50, Jan. 2005.

[63] Shoham, M., Lieberman, I.H., Benzel, E.C., Togawa, D., Zehavi, E., Zilberstein, B., Roffman, M., Bruskin, A., Fridlander, A., Joskowicz, L., Brink-Danan, S., Knoller, N. "Robotic Assisted Spinal Surgery – from Concept to Clinical Practice." Computer Aided Surgery, Vol. 12, No. 2, pp. 105-115, 2007.

[64] Sikorski, J.M., Chauhan, S. "Computer-Assisted Orthopaedic Surgery: Do We Need CAOS?" Journal of Bone and Joint Surgery, Vol. 85-B, No. 3, pp. 319-323, April 2003.

[65] Spencer, J.M.F. "Computer Navigation of the Acetabular Component: A Cadaver Reliability Study." Journal of Bone and Joint Surgery, Vol. 88-B, pp. 972-975, 2006.

[66] Stulberg, S.D., Loan, P., Sarin, V. "Computer-Assisted Navigation in Total Knee Replacement: Reults of an Initial Experience in Thirty-five Patients." The Journal of Bone and Joint Surgery, Vol. 84-A, No. 2, pp. 90-98, 2002.

[67] Suetens, P. Fundamentals of Medical Imaging. New York, NY: Cambridge University Press, 2002.

[68] Sugita, N., Matsuda, N., Warisawa, S., Mitsuishi, M., Fujiwara, K., Abe, N., Hashizume, H. "Development of a Computer-Integrated Minimally Invasive Surgical System for Knee Arthroplasty." IEEE International Conference on Biomedical Robotics and Biomechatronics, pp. 323-328, 2006.

[69] Topchyan, A., Tatarinov, A., Sarvazyan, N., Sarvazyan, A. "Ultrasound Velocity in Human Muscle In Vivo: Perspective for edema studies." Ultrasonics, Vol. 44, pp. 259-264, 2006.

[70] Tucker, J.M., "Optimized Registration for Computer Assisted Total Knee Arthroplasty." Penn State McNair Journal, Vol. 10, pp. 260-274, 2003.

[71] U.S. Department of Health and Human Services, Centers for Disease Control and Prevention. "Targeting Arthritis: Public Health Takes Action," 2002.

[72] U.S. Department of Health and Human Services, Centers for Disease Control and Prevention. "Targeting Arthritis: The Nation's Leading Cause of Disability," 2004.

[73] Wang, L.I., Greenspan, M., Ellis, R. "Validation of Bone Segmentation and Improved 3-D Registration Using Contour Coherency in CT Data." IEEE Transactions on Medical Imaging, Vol 25, No. 3, pp. 324-334, March 2006.

[74] Weber, P., Schlegel, J.C., Meiche, J., Peter, L., Harland, U. "A System for Ultrasound Based Intraoperative Navigation in Spine Surgery." IEEE Ultrasonics Symposium, pp. 1361-1364, 2001.

[75] Widmann, G. "Image-Guided Surgery and Medical Robotics in the Cranial Area." Biomedical Imaging and Intervention Journal, Vol. 3, No. 1, p. e11, 2007.

[76] Wieclwek, W., Pietka, E. "Live-Wire-Based 3D Segmentation Method." Proceedings of the 29th Annual International Conference of the IEEE EMBS, pp. 5645-5648, Lyon, France, Aug 2007.

[77] Wiles, A., Thompson, D., Frantz, D. "Accuracy Assessment and Interpretation for Optical Tracking Systems." Medical Imaging Proceedings 5367, Visualization, Image-Guided Procedures, 2004.

[78] Wilson, E. "Accuracy Analysis of Electromagnetic Tracking Within Medical Environments." Catholic University of America, Master's Thesis, Washington D.C., 2006.

[79] Wong, K.C., Kumta, S.M., Chiu, K.H., Antonio, G.E., Unwin, P., Leung, K.S. "Precision Tumor Resection and Reconstruction using Image-Guided Computer Navigation." The Journal of Bone and Joint Surgery, Vol. 89-B, pp. 943-947, 2007.

[80] Wu, X., Taylor, R. "A Framework for Calibration of Electromagnetic Surgical Navigation Systems." Proceedings of the 2003 IEEE/RSJ International Conference on Intelligent Robots and Systems, Las Vegas, Nevada, October 2003.

[81] Xiaojun, C., Chengtao, W., Yanping, L. "A Computer-Aided Oral Implantology System." Proceedings of the 2005 IEEE Engineering in Medicine and Biology 27th Annual Conference Shanghai, China, September 1-4, 2005.

[82] Yau, W.P., Leung, A., Liu, K.G., Yan, C.H., Wong, L.L.S., Chiu, K.Y. "Interobserver and Intra-observer Errors in Obtaining Visually Selected Anatomical Landmarks During Registration Process in Non-Image-Based Navigation-Assisted Total Knee Arthroplasty." The Journal of Arthroplasty, Vol. 22, No. 8, pp. 1150-1161, 2007.